Spectro-polarimetry of the solar chromosphere in the He I 10830 Å lines

Dissertation
zur Erlangung des Doktorgrades
der Mathematisch-Naturwissenschaftlichen Fakultäten
der Georg-August-Universität zu Göttingen

vorgelegt von
Clementina Sasso
aus Torre del Greco / Napoli / Italia

Göttingen 2008

Bibliografische Information Der Deutschen Bibliothek

Die Deutsche Bibliothek verzeichnet diese Publikation in der Deutschen Nationalbibliografie; detaillierte bibliografische Daten sind im Internet über `http://dnb.ddb.de` abrufbar.

D7
Referent: Prof. Dr. Franz Kneer
Korreferent: Prof. Dr. Sami K. Solanki
Tag der mündlichen Prüfung: 18 März 2008

ISBN 978-3-936586-85-5

Copernicus Publications 2008
http://publications.copernicus.org
© Clementina Sasso

Printed in Germany

Contents

Summary **5**

1 Introduction **7**

2 Prominences and Filaments **9**
- 2.1 General properties 9
- 2.2 Motions and velocities in prominences 10
  - 2.2.1 Activity and eruption 12
- 2.3 Magnetic field in prominences 12
  - 2.3.1 Models of prominence support 13
- 2.4 Recent results and outlook 16

3 Spectropolarimetry **19**
- 3.1 Stokes parameters 19
- 3.2 Zeeman effect 20
- 3.3 Paschen-Back effect 22
- 3.4 The He ɪ 10830 Å lines 23
- 3.5 Radiative transfer equation 25
- 3.6 Solution of the RTE 27
  - 3.6.1 Milne-Eddington approximation 28
- 3.7 Inversion of Stokes profiles 28
  - 3.7.1 HeLIx 29
  - 3.7.2 Multi-component inversion 30

4 Inversions of the He ɪ 10830 Å: The influence of the Paschen-Back effect **31**
- 4.1 Introduction 31
- 4.2 Methods and results 32
  - 4.2.1 Inversion of synthetic profiles 32
  - 4.2.2 Inversion of observational data 32
  - 4.2.3 Stokes *V* asymmetry 36
- 4.3 Conclusions 38

5 Observations **41**
- 5.1 Instruments 41
- 5.2 Observations 41
- 5.3 Analysis of the Stokes profiles 48
- 5.4 Supersonic flows 50

5.5 Conclusions 50

6 Analysis and Results **53**
6.1 Fit to the observations 64
6.2 Maps of retrieved parameters 75
6.3 Discussion 80

7 Conclusions & Outlook **85**

Bibliography **89**

Publications **95**

Acknowledgements **97**

Lebenslauf **99**

Summary

This thesis is based on the analysis and interpretation of spectropolarimetric observations obtained in the He ɪ lines at 10830 Å. In particular, we refer to observations of an active region filament located close to the solar disc center, during its phase of activity. The aim of this study is to provide novel observational results on the magnetic field measurements in solar prominences and filaments to give constraints to the theoretical models of their support in the solar corona. The main goal is to interpret the behavior of the atmospheric parameters retrieved from the spectropolarimetric data to give a picture of the magnetic structure of the observed filament. It is the first time that the magnetic structure of a flaring filament has been determined.

The correct inversion of the He Stokes profiles requires their formation in the incomplete Paschen-Back effect regime to be studied. In order to take this effect into account, we have improved the numerical code for the synthesis and inversion of Stokes profiles and investigate the influence of this effect on the inversion of polarimetric data. A comparison between the results of inversions based on synthetic profiles calculated with and without the inclusion of the Paschen-Back shows that when taking into account the incomplete Paschen-Back effect, on average 16% higher field strength values are obtained. We also find that this effect is not the main cause for the area asymmetry exhibited by many He ɪ 10830 Stokes *V*-profiles. This points to the importance of velocity and magnetic field gradients over the formation height range of these lines.

The analysis of the observed polarization of the He ɪ 10830 Å multiplet in the filament, carried out by inverting the Stokes profiles, reveals the presence of different unresolved atmospheric components of the He lines, coexisting within the resolution element (~ 1.2 arcsec). The different components, belonging to different magnetic field lines, show supersonic up- and downflows, sometimes within the same resolution element. The He blueshifted components belong to mostly transversal field lines in the body of the filament. These field lines are found to be curving upwards on both sides. This picture suggests the presence of dipped field lines that are moving upward, carrying with them the filament material. During this movement, we also observe filament material flowing down along field lines having the same polarity as the photospheric field (i.e. they have the opposite inclination with respect to the dipped field lines). These downflows are faster at the filament end points and can reach values close to 10 times the speed of sound. The field lines are found to be almost parallel to the filament axis in the plane perpendicular to the line of sight. This is in agreement with previous measurements. The two main theoretical models of prominence support (dip or flux rope models) have been used to interpret the results obtained. Even if the observed dipped field lines are predicted by both models, globally our observations can be explained better in terms of the flux rope model than the dip model.

1 Introduction

Solar prominences (or filaments when they are observed on the solar disc) are relatively dense and cold objects, located in the surrounding much hotter and less dense corona. Although prominences have been observed and studied for decades, there are still many open questions about their formation, structure and stability. Magnetic fields are known to play a key role in supporting the prominence material against gravity and acting as a thermal shield for the cool plasma against the million-degree coronal environment. Theoretical models have been proposed to explain how the cold prominence plasma can be supported by a magnetic field. These models are based on only few measurements of the magnetic field vector obtained mainly through spectropolarimetric observations in the He I D_3 line seen in emission in prominences at the limb and in the Hα line. In order to provide more statistics needed in order to set constraints on the theoretical models of prominence support and to discern between them, new observational results are required. Recently, the He I 10830 Å lines were indicated as diagnostics of magnetic field in prominences observed at the limb but also in filaments on the disc (Lin et al. 1998, Trujillo Bueno et al. 2002, Merenda 2006). Similar to the Hα line, in fact, filaments appear as dark absorption features also in the He I 10830 Å line. Measurements in these lines could help to obtain information on the magnetic field, particularly in the case of the low-lying active region filaments, difficult to be observed at the limb since hidden by chromospheric spicules.

The He I 10830 Å triplet is formed in the upper solar chromosphere. Its components are sensitive to the magnetic field via the Zeeman effect and therefore are suitable for spectropolarimetric measurements. In the last years, spectropolarimetry in these lines has become one of the key tools to determine the magnetic field vector in the upper chromosphere (Trujillo Bueno et al. 2002, Solanki et al. 2003).

In this context, we present this thesis work with the main aim of analyzing spectropolarimetric data (the full Stokes vector) obtained in the He I triplet at 10830 Å of an active region filament observed close to disc center, during its phase of activity. The data were recorded with the second generation Tenerife Infrared Polarimeter (TIP-II) at the German Vacuum Tower Telescope (VTT) on 2005 May 18. The activation of the filament (increased internal turbulent motions accompanied by a rising motion of the whole prominence), followed a nearby flare eruption that most probably destabilized the magnetic configuration of the filament supporting field lines, causing its activation. The observations follow the change of the magnetic structure of the filament resulting in a row of interesting features visible in the He I 10830 Å Stokes profiles. We retrieve the values of the atmospheric parameters like the magnetic field vector and the line-of-sight velocity for the profiles we have observed, by means of an inversion procedure. This is done by applying to the observed Stokes profiles a numerical code for the synthesis and inversion of Stokes profiles in a Milne-Eddington atmosphere (Lagg et al. 2004). In previous papers (Solanki et al. 2003, Lagg et al. 2004), the analysis of the observed polarization in the He ɪ 10830 Å multiplet was carried out considering the linear Zeeman splitting approximation. Socas-Navarro et al. (2004) pointed out the importance of treating the formation of the He ɪ 10830 lines by considering the wavelength positions and the strengths of the Zeeman components in the incomplete Paschen-Back effect regime. The Paschen-Back effect influences the Zeeman sublevels, leading to changes in strength and in position of the Zeeman components of these lines. The code for the inversions of the Stokes profiles has been improved to take into account the Paschen-Back effect and its influence on the inversion of polarimetric data has been investigated.

The overall behavior of the retrieved atmospheric parameters in the observed filament is interpreted to give a picture of its magnetic structure during the activity phase.

The thesis is organized as follows. In the first chapter, the basic properties of solar prominences and the physical processes that govern their structure and dynamics are described, together with the proposed models of their magnetic support. In the second chapter, the theory of polarized radiation is introduced. At the end of the chapter, the concept of the inversion technique, the mathematical formulation and the description of the code we used to invert the Stokes profiles are also presented. In the third chapter, we illustrate the relevance of the Paschen-Back effect in the formation of the He ɪ 10830 Å multiplet lines using synthetic Stokes profiles. We also investigate the influence of the Paschen-Back effect on the retrieved value of the atmospheric parameters. The results of inversions based on synthetic profiles calculated with and without including the Paschen-Back effect are compared. The observations of the full Stokes vector in the filament are presented in the fourth chapter. In the fifth chapter we discuss the results of the inversions of the observed Stokes profiles to find an overall description of the magnetic field supporting the filament. A comparison is then made with the theoretical models of prominence support. Finally, in the last chapter, we summarize the results presented in the previous chapters and identify future steps that need to be taken to improve on the results of the present study.

2 Prominences and Filaments

In this introductory chapter we will describe the basic properties of solar prominences and filaments and the physical processes that govern their structure and dynamics. In the last 20 years, different theoretical models have been developed to explain how the cold prominence plasma can be supported by magnetic field in the solar corona. This brief review will introduce the main characteristics of these models and also the measurements of prominence magnetic fields obtained mainly through spectropolarimetric observations.

2.1 General properties

Solar prominences are relatively dense and cold objects, embedded in the surrounding much hotter corona (Tandberg-Hanssen 1974, 1995), the outer layer of the solar atmosphere. Prominences are located at heights of $\sim 10^5$ km above the photosphere of the Sun and their temperature is $\sim 10^4$ K, a hundred times lower then the temperature of the surrounding corona. The particle densities range from 10^{16} to 10^{17} m^{-3}, a hundred times greater than coronal values. While the corona consists of extremely hot fully-ionized gas (plasma), prominences contain much cooler and denser ionized gas, similar in composition to that of the chromosphere.

Prominences are usually observed above the solar limb in emission in the Hα line (the first spectral line of the Balmer series of neutral hydrogen) at a wavelength of 6563 Å, appearing as bright features against the dark background (see Fig.2.1). When seen projected against the solar disc, prominences show up in absorption in Hα, looking as dark, elongated features against the bright disc, referred to as filaments (see Fig.2.2). Nowadays, we know that the two terms, prominence and filament, refer to the same structure but historically they were used to identify what were thought to be different objects. In this work we will use the general term prominence when dealing with common properties of both objects and we will use the term filament only referring to prominences seen against the solar disc.

A prominence forms over timescales of about a day and can be stable with lifetimes ranging from several days to months or can be a transient phenomenon that lasts hours or less. Prominences differ also in morphology and typical size. A variety of classifications has been proposed over the years regarding prominences, based on their morphology and activity. Commonly, they have been placed in two basic categories (Tang 1987, Zirin 1988, Martin 1990, Tandberg-Hanssen 1974, 1995): quiescent and active region prominence. The former are generally associated with the decaying phase of an active region, forming from its remnants (Gaizauskas et al. 2001). They are long, thin sheet-like structures, nearly vertical to the solar surface, with typical length of 10^5 km, height of 10^4 km and

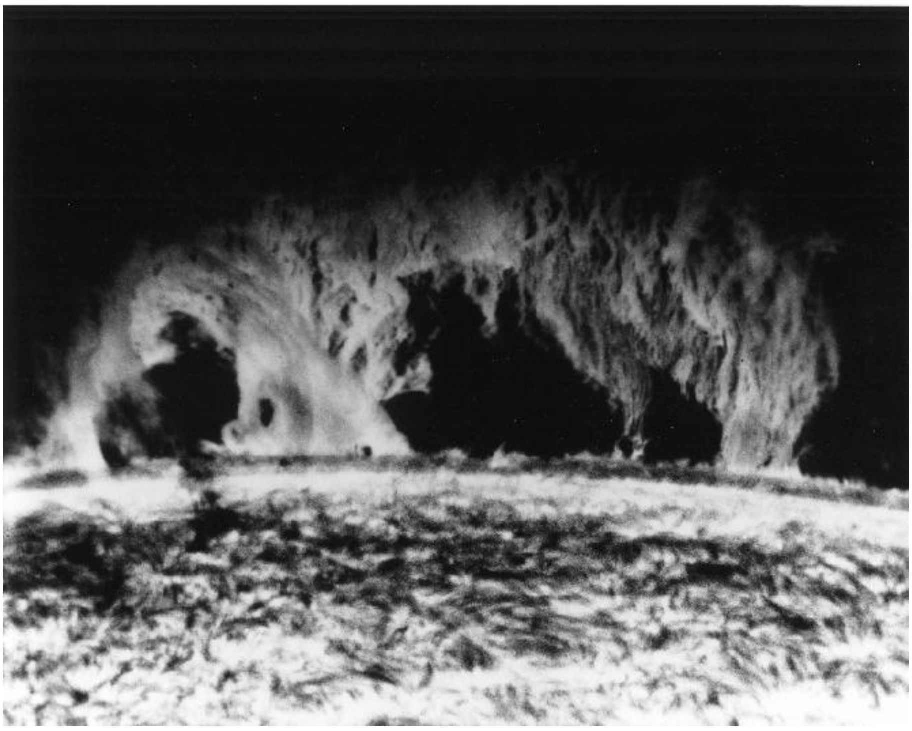

Figure 2.1: A typical quiescent prominence observed at the edge of the Sun in 1970. Quasi-vertical plasma threads are well visible. Source: BBSO/NJIT.

thickness of 10^4 km. They are suspended high in the corona and are stable objects, living for a long time (days to months). Active region prominences form in and around active regions in correspondence with newly emerged magnetic fields. They are shorter in length, low lying and evolve very fast compared to the evolution of the associated active region. Their density is rather large (10^{17} m^{-3}). A quiescent prominence may begin life as a relatively small active region prominence and as the active region disperses, it grows thicker and longer to become a quiescent prominence. It may continue growing for many months up to 10^6 km in length, and during the process it migrates slowly towards the nearest solar pole.

Prominences are always located above the neutral lines that separate regions of opposite magnetic polarity in the photospheric field (Babcock & Babcock 1955) and beneath the coronal arcades connecting these opposite polarity regions. In the case of active regions prominences, their shape follows the complicated magnetic field structure of the active region and they have the curved shape of their associated polarity inversion lines.

2.2 Motions and velocities in prominences

The speed of the prominence material determines whether a prominence can be defined an active or a quiescent object. A prominence can be subject to two different kind of motions: an overall motion, e.g., an oscillation or an eruption of the whole structure, or internal motions that do not alter its shape. Prominences exhibit a large variety of fine structures and information about their morphology and dynamics comes above all from

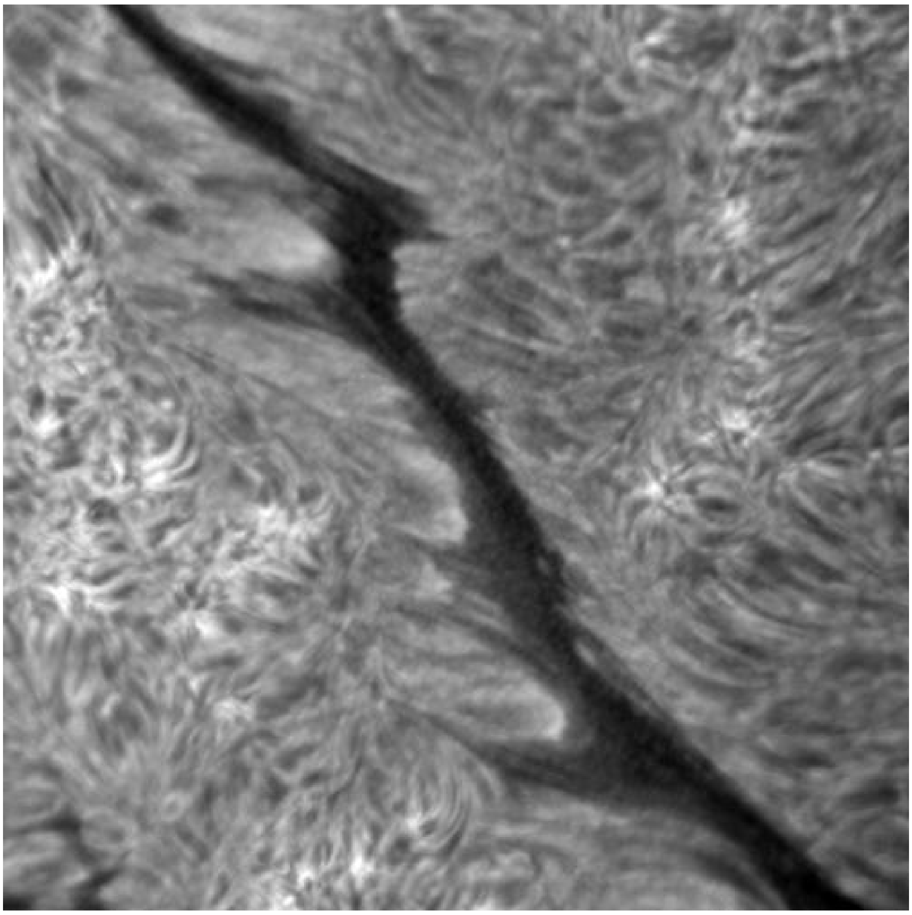

Figure 2.2: Filament observed in the Hα line on 2000 May 6, at the NSO, Sacramento Peak. Source: National Solar Observatory/AURA/NSF.

high resolution ($\sim$ 100 km) ground based observations obtained mostly in the Hα line.
Quiescent prominences show both internal and global motions. Images and movies show that the material is concentrated in thin vertically oriented threads of diameter of few hundreds km with the material slowly either streaming down or rising up the threads. Superimposed on this vertical velocity, different threads of plasma exhibit a random motion with velocities of 5–10 km/s. On the disc, the high resolution Hα images and movies show fine structure fibrils of different lengths. They move sideways with velocities up to 3 km/s. Stronger horizontal motions of $\sim$ 15 km/s are also recorded. For quiescent prominences with one end interacting with a sunspot, it has been observed that the material is streaming out of the prominence, going down into the sunspot. In this case, the vertical velocity is much higher than 5 km/s.
Active region prominences show considerable internal motion. They are characterized by a continuous flow of material along the body axis. This is one of the strongest descriptive differences between active and quiescent filaments.

2.2.1 Activity and eruption

Active region and quiescent prominences can become ‘activated’ and exhibit several types of large-scale motions. For example, a prominence can show its activity by becoming larger and darker (when viewed on the disc as a filament) or brighter (at the limb). This activity can correspond to an increase in turbulent motion or to flows along the prominences. This type of activation sometimes fades away after a short period or it can happen that the prominence becomes completely unstable and erupts, eventually followed by ejection of coronal material escaping from the Sun, while some material descends to the chromosphere along helical arches. In this case the prominence can eventually disappear. In two-third of eruptions, the prominence reforms in the same place and with minor changes of the shape.

In case of ‘activated’ quiescent prominences, velocities of 30–50 km/s are observed. The increased internal turbulent motions are characterized by a chaotic behavior of the fine structure details of the prominence plasma and are often accompanied by a slow rising motion of the whole prominence (few km/s). Depending on the case, the prominence can return to its original quiescent state or be subject to very strong internal motions of the plasma, up to 300 km/s, and then come at rest again.

The eruption of an old quiescent prominence starts with a slow rise at a few km/s and may take several hours. It is accompanied by an X-ray brightening and occasionally by the appearance of Hα flare ribbons. One interesting case of eruption, in which high velocities are measured happens when a quiescent prominence undergoes a sudden disappearance due to an ascending motion. The phenomenon is referred to as ‘disparition brusque’. The prominence material starts to exhibit increased random internal motions (velocities of 30–50 km/s) and then the whole prominence starts to rise with increasing velocities of several hundred km/s and the prominence is ejected into the corona. The cause is generally not a flare-induced activation.

As in the case of quiescent prominences, the activation of an active region filament can happen with increased internal motions that can lead or not to an eruption or a disparition brusque. The eruption of an active region prominence is much more rapid and takes about half an hour or less; while the prominence is still ascending at high speed, a two ribbon Hα flare begins and, in this case, the prominence generally reforms after only a few hours. Motions and velocities in active region filaments were observed also in the He I lines at 10830 Å. Observations of an erupting active region filament presented by Penn (2000), saw the He I absorption line blue-shifted to velocities between 200 and 300 km/s. In the same observation, the filament showed also internal motions with multiple Doppler components shifted by ±25 km/s. Very high velocity redshifts (30-60 km/s) were instead reported by Penn & Kuhn (1995) in an active filament during the decay phase of a flare always in the He I 10830 absorption lines.

2.3 Magnetic field in prominences

Although prominences have been studied for decades, there are still many open questions about their formation, structure and stability. Magnetic fields are known to play a key role in supporting the prominence material against gravity and also acting as a thermal shield for the cool plasma against the million-degree coronal environment (Kippenhahn

& Schlüter 1957, Tandberg-Hanssen 1974, 1995). Quiescent and active prominences are thought to share the same basic magnetic structure and mechanisms, although they differ in magnetic intensity, structural complexity, structural length scale and evolutionary timescale (Low & Hundhausen 1995).

The magnetic field in solar prominences has been measured since several decades. Most of our knowledge is derived from direct prominence polarization observations using first the Zeeman effect and later on the Hanle effect (see Chap. 3). First measurements, obtained in the 80's and still valid today, found on average a measured magnetic field strength typically of 10-20 G and with the magnetic field vector almost parallel to the body axis of the prominence, forming with it an angle of $\sim 20^\circ$ in the horizontal plane (Leroy 1989, for a review). The observations analyzed were obtained in the He I D_3 line at 5878 Å seen in emission in a quiescent prominence observed at the limb. Practically, the measurements have indicated the predominance of horizontal field lines threading the prominence whose principal component is directed along the long axis of the prominence. Much of the theoretical work in modeling the magnetic field in prominences, that followed in the 90's, was based on these measurements. It is based on the idea that a prominence is composed by cool plasma which has come to rest at the lowest points of upward-concave (dipped) or nearly horizontal field lines. The presence of a magnetic force in the prominences (and the surrounding corona) is made possible by the fact that both consist of ionized gas, in which there is a high concentration of free electrons. The high electrical conductivity of the plasma allows electric currents to easily flow through it, forcing the material to move along the magnetic field lines. Therefore the cool prominence plasma will stay on the field line on which it was originally located, being not allowed to easily cross from one field line to another. Under the influence of gravity it will slide down along the field line until it reaches the chromosphere or encounters a 'dip' in the field line where the field is locally horizontal and curved upward.

Models of prominence magnetic structures have been discussed by a number of authors and among these models of magnetic configurations many propose the existence of these dipped field lines (Kippenhahn & Schlüter 1957, Wu et al. 1990, Antiochos et al. 1994, Choe & Lee 1992, Van Hoven et al. 1992). Some of the models describe also the mechanisms of prominence formation. Actually, the way in which a prominence is formed can determine the mechanisms of its support. For the purpose of this thesis, we will give an overview of these models only from the point of view of the support of the prominence material, without going into the details of prominence formation.

2.3.1 Models of prominence support

The first authors to propose and develop a model for the equilibrium and stability of prominence plasma in a magnetic configuration with dipped field lines were Kippenhahn & Schlüter (1957). They assumed a main field configuration in which the polarity of the magnetic field lines threading the prominence material is the same as the polarity of the underlying photospheric field (see Fig. 2.3a). In this case the prominence has a *normal polarity field*. In their paper the authors suggested that the prominence can be stably supported only at places where the field lines are locally horizontal and curved upward. So, the prominence material sits in the dip at the top of the magnetic field lines connecting the two opposite polarity photospheric regions. More recently, the model has been referred

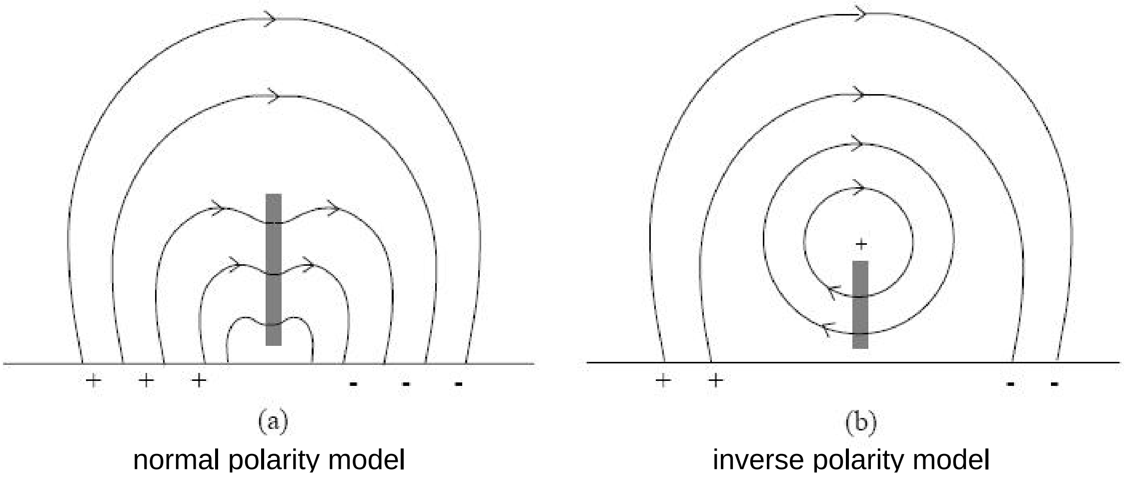

Figure 2.3: Two models of the magnetic field supporting a solar prominence: (a) Kippenhahn-Schlüter model (normal polarity model). (b) Kuperus-Raadu model (inverse polarity model). These figures show the projection of the field lines into the plane perpendicular to the long axis of the prominence (shaded region). The horizontal line at the base indicates the solar photosphere. The picture has been adapted from van Ballegooijen (2000).

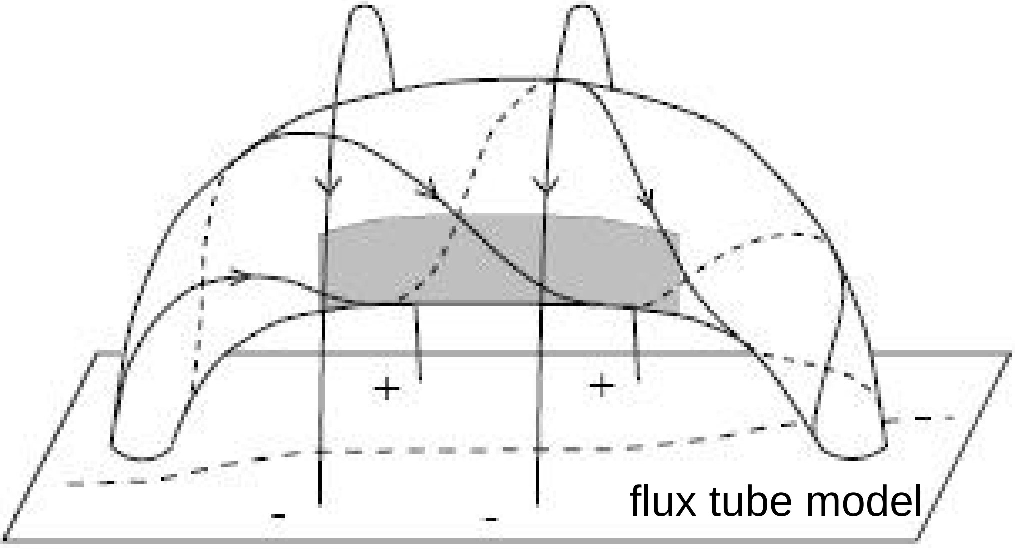

Figure 2.4: Twisted flux tube model for solar prominences. The prominence sheet is indicated by the shaded region. The picture has been adapted from van Ballegooijen (2000).

to as the *normal polarity dip model*.

Later, Kuperus & Tandberg-Hanssen (1974) proposed a different field configuration developed by Kuperus & Raadu (1974). A closed-loop magnetic field supports the filament material and shields it from the hot coronal plasma (see Fig. 2.3b). In this model the magnetic field lines threading the prominence material are in the opposite direction than the photospheric magnetic field. In this case the prominence has an *inverse polarity field*.

Both models are two–dimensional with the magnetic field confined in a vertical plane with respect to the solar surface. The work of Leroy (1989) showed that prominences possess a strong magnetic field along the axial direction. These led to the development of three–dimensional models: a magnetic field component normal to the plane of the Fig. 2.3 is assumed to exist, and this field component transforms the closed field lines in the inverse configuration model (b) into helical fields in three-dimensional space forming flux ropes. The flux rope naturally presents dips (troughs of the helical windings) where plasma can accumulate in a stable manner. The prominence material sits in the lower part of the flux rope.

The idea of quiescent prominences supported by helical flux ropes that lie horizontally above the polarity inversion line on the photosphere, with the main axis roughly parallel to it (see Fig.2.4) has been discussed and developed later by many authors. Research has also moved into the detailed description of the magnetic topology of the flux rope. A large twisted magnetic flux rope is indeed an appealing prominence model because its helical field lines provide support for the mass of the prominence and isolate the cold prominence plasma from the hot corona. A coronal flux rope can be defined as a magnetic structure that contains field lines that twist about each other by more than one winding between the two ends anchored to the photosphere (Priest et al. 1989, Low 2001). Most of the present models are based on flux tubes that possess some degree of twist (van Ballegooijen & Martens 1989, Antiochos et al. 1994, Priest et al. 1989, Priest 1990, Amari et al. 1999). Such models comprise also a coronal arcade that is overlying the helical field. Depending on the class of models (normal or inverse polarity, see Fig. 2.3) the coronal magnetic field around prominences will have different characteristics and likely, it plays an important role in the equilibrium and stability of the field. In order to have an idea on how such a flux rope model appears in a realistic situation, we show in Fig. 2.5 an example of modeling of a filament magnetic topology as it was obtained by Aulanier & Schmieder (2002). The lower twisted lines represent the magnetic field lines passing through the filament body while the upper loop-like lines are the coronal magnetic lines.

Interpretation of polarimetric data have suggested that most quiescent prominences have inverse polarity. The normal configuration happens only for a small minority of prominences, generally low-lying (Bommier et al. 1994). The measurements also show a tendency for the field strength and the alignment of the magnetic vector with the prominence axis to increase with height inside the prominences observed at the limb. These two properties have been explained in terms of the magnetic field of a prominence embedded in a flux rope in the inverse configuration. These models have been successful also in explaining other observational constraints on prominences, including the fact that when a prominence erupts it sometimes looks like a twisted tube.

In this section about prominence models we have also to mention that even if most of the present models are based on flux tubes, there are still some models that claim for vertical fields constrained in current sheets (curtain models, Osherovich 1989, Jensen 1990, Péc-

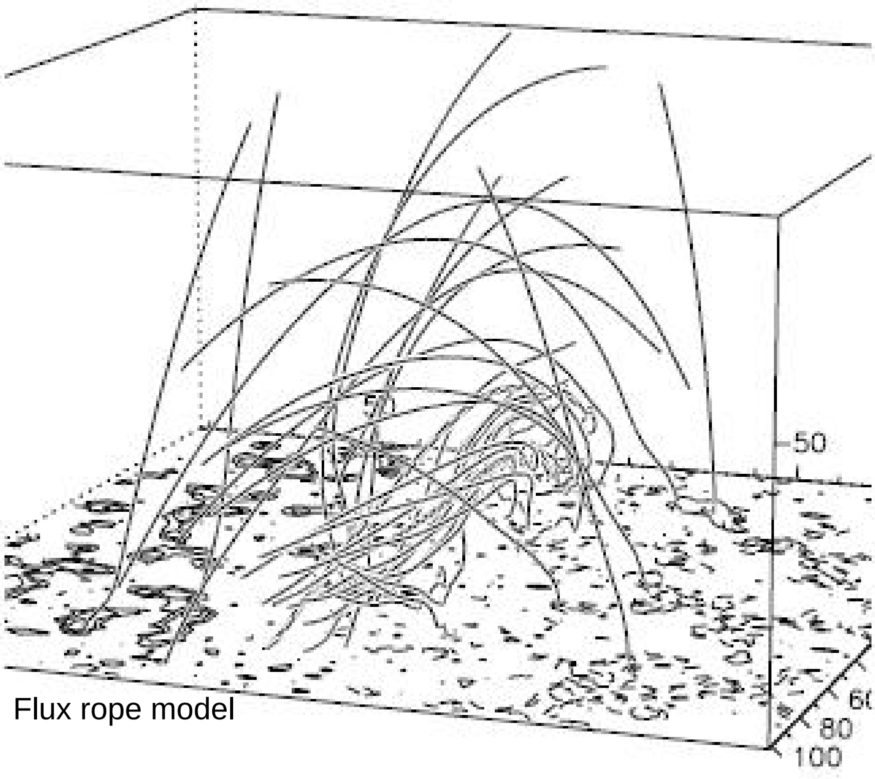

Figure 2.5: Example of modeling of a filament magnetic topology. The picture has been adapted from Aulanier & Schmieder (2002).

seli & Engvold 2000) based on the observation at certain wavelength of vertical structures.

2.4 Recent results and outlook

After the first results obtained in the 80's, on the determination of magnetic field in prominences, not many measurements were performed for about 10 years. Only recently, with the advent of a new generation of spectropolarimeters and the development of new techniques for analyzing and interpreting the data and a better understanding of the physics of the formation of spectral lines, there was a renewed interest in the diagnostics of the magnetic field in prominences.

In recent years, Casini et al. (2003) presented the first map of the magnetic field in a prominence observed at the limb. They retrieved the magnetic field vector values by inverting spectropolarimetric data obtained in the He I D_3 line seen in emission. The average magnetic field is mostly horizontal and varies between 10 and 20 G. These results confirm previously measured values. However, the maps also show that the field can be significantly stronger than average, up to 80 G, in clearly organized plasma structures of the prominence. They also found a slow turn of the field vector away from the prominence axis as the edge of the prominence is approached.

Recently, some authors pointed out the diagnostic potential of another He I line, the triplet at 10830 Å, seen in emission in prominences (Trujillo Bueno et al. 2002, Merenda 2006). Measurements of the polarization of the He ɪ 10830 Å radiation are also indicated as a useful new tool for the diagnostics of magnetic field in filaments (Lin et al. 1998, Trujillo Bueno et al. 2002). Similar to the Hα line, in fact, filaments also appear as dark absorption features in the He ɪ 10830 Å line. This is not the case for the He ɪ D_3 line, in which filaments do not show strong absorption on the solar disc. There are strong motivations to extending the magnetic field diagnostics to filaments observed on the solar disc, particularly in order to better study also the low-lying active region filaments, difficult to be observed at the limb since hidden by chromospheric spicules. Trujillo Bueno et al. (2002) found practically horizontal fields in a filament located at the very center of the solar disc, with a strength of 20 G.

While the magnetic field in quiescent prominences has been widely investigated, less is known about the field in active prominences. Some recent measurements of magnetic field in an active region filament obtained in the He ɪ 10830 line by Martínez Pillet appeared in a recent review of López Ariste & Aulanier (2007). The magnetic field strengths retrieved by fitting the spectropolarimetric observations with a Milne-Eddington model (see Chap. 3) are of the order of hundreds of G. These values are much higher than previous measurements which found a field ranging from 20 to 70 G (Tandberg-Hanssen 1974).

New observational results are required to provide more statistics in order to give constraints to the theoretical models of prominence support.

3 Spectropolarimetry

In this chapter the theory of polarized radiation will be described starting from the definition of the Stokes vector and the introduction of the Zeeman and the Paschen-Back effect. Then the Radiative Transfer Equation (RTE) in the presence of a magnetic field will be presented. We will mainly follow the approach and the notation of Landi Degl'Innocenti & Landolfi (2004) and del Toro Iniesta (2003). At the end, a description of the inversion technique we applied to the spectropolarimetric data in order to retrieve information on the magnetic field vector will be given.

3.1 Stokes parameters

Let us consider the electric field vector **E** of a quasi-monochromatic electromagnetic plane wave propagating along the *z*-axis, with mean frequency ν (mean wavelength λ) and spectral width $\Delta\nu \ll \nu$. The components of **E** in the plane perpendicular to the direction of propagation are

$$E_{\rm x}(t) = a_{\rm x}(t)\exp[i(\phi_{\rm x}(t) - 2\pi\nu t + 2\pi z/\lambda)], \tag{3.1}$$
$$E_{\rm y}(t) = a_{\rm y}(t)\exp[i(\phi_{\rm y}(t) - 2\pi\nu t + 2\pi z/\lambda)]. \tag{3.2}$$

The Stokes parameters are defined in terms of the amplitudes, $a_{\rm x}$ and $a_{\rm y}$, and the phases, $\phi_{\rm x}$ and $\phi_{\rm y}$ of $E_{\rm x}$ and $E_{\rm y}$, as follows:

$$I = < a_{\rm x}^2 > + < a_{\rm y}^2 >, \tag{3.3}$$
$$Q = < a_{\rm x}^2 > - < a_{\rm y}^2 >, \tag{3.4}$$
$$U = 2 < a_{\rm x}a_{\rm y}\cos\delta >, \tag{3.5}$$
$$V = 2 < a_{\rm x}a_{\rm y}\sin\delta >, \tag{3.6}$$

where $\delta = \phi_{\rm x} - \phi_{\rm y}$ and $<>$ stands for the time average. The rotation of the electric field in the plane *xy* is counterclockwise if $\sin\delta < 0$ and clockwise if $\sin\delta > 0$.
A condition for I is that the intensity of polarized light cannot be larger than the total intensity of light:

$$I^2 \geq Q^2 + U^2 + V^2. \tag{3.7}$$

The equality holds when the radiation beam is completely polarized.
All four Stokes parameters are real and have dimensions of intensity. They are thus measurable and they can also be defined operationally. If we consider two perfect linear polarizers whose transmission axes are oriented at an angle θ measured counterclockwise to the *x*-axis as viewed by the observer receiving the light, then:

- I represents the sum of the measured intensities transmitted through the perfect linear polarizers whose transmission axes are mutually orthogonal, i.e. the linear polarizers are oriented at angles 0° and 90°, respectively.
- Q is the difference between the measured intensities transmitted through the linear polarizers oriented at angles $\theta = 0°$ and $\theta = 90°$.
- U represents the difference between the measured intensities transmitted through the linear polarizers at angles $\theta = 45°$ and $\theta = 135°$.
- V is the difference between the measured intensities transmitted through a quarter-wave linear retarder, followed by the two linear polarizers at $\theta = 45°$ and $\theta = 135°$. By this definition, V measures the difference between right (clockwise) and left (counterclockwise) circularly polarized light.

The polarimeters we used to record the observations analyzed in this work (Tenerife Infrared Polarimeter, TIP-I and II) are based on this principle. A description will be given in Chapter 5.

3.2 Zeeman effect

The Hamiltonian H of an electron in an atom in an external, uniform magnetic field can be written as the unperturbed Hamiltonian H_0 of the electron plus an additional term H_B, called the *magnetic Hamiltonian*, that takes into account the interaction of the magnetic moment of the electron with the magnetic field.

The unperturbed Hamiltonian H_0 is characterized by two contributions: H_C describes the Coulomb interaction of the electron with the nuclear charge and the electronic cloud, and H_LS represents the coupling between the spin angular momentum of the electron S and the orbital angular momentum L.

We are interested in the effect of the new term H_B on the unperturbed Hamiltonian H_0 to study how the energy levels of the atom change in the presence of a magnetic field. The magnetic Hamiltonian is given by

$$\mathrm{H}_\mathrm{B} = \mu B, \tag{3.8}$$

$$\mu = \mu_0 (L + 2S), \tag{3.9}$$

$$\mu_0 = \frac{eh}{4\pi m_e c}, \tag{3.10}$$

where e and m_e are, respectively, the charge and the mass of the electron, B is the magnetic field strength, h is the Planck constant, c the speed of light and $\mu_0 = 9.27\ 10^{-21}$ ergs G^{-1} is the Bohr magneton.

In the total Hamiltonian $\mathrm{H} = \mathrm{H}_0 + \mathrm{H}_\mathrm{B} = \mathrm{H}_\mathrm{C} + \mathrm{H}_\mathrm{LS} + \mathrm{H}_\mathrm{B}$ the terms H_LS and H_B are much smaller in magnitude than H_C. In order to calculate the corrections to the energy levels of the total Hamiltonian H due to the magnetic field, we can apply the perturbation theory. We can distinguish three possibilities:

1. Weak magnetic field case, $\mathrm{H}_\mathrm{LS} \gg \mathrm{H}_\mathrm{B}$: in the calculation of the new energy levels, first, H_LS has to be considered as a perturbation to H_C and then H_B to $\mathrm{H}_\mathrm{C} + \mathrm{H}_\mathrm{LS} = \mathrm{H}_0$. This is the so-called *Zeeman regime*.

2. Strong magnetic field case, $\mathrm{H_B} \gg \mathrm{H_{LS}}$: first, $\mathrm{H_B}$ has to be considered as a perturbation to $\mathrm{H_C}$ and then $\mathrm{H_{LS}}$ to $\mathrm{H_C} + \mathrm{H_B}$. We are in the *Paschen-Back regime*.

3. $\mathrm{H_B} \sim \mathrm{H_{LS}}$, the two contributions are comparable. $\mathrm{H_{LS}} + \mathrm{H_B}$ is a perturbation to $\mathrm{H_C}$. We are in the *intermediate regime*.

In this section we will concentrate on the first case, describing the Zeeman effect regime; in the next section the theory of the Paschen-Back effect will be introduced.
In order to estimate the effect of $\mathrm{H_B}$ on the unperturbed Hamiltonian $\mathrm{H_0}$ in case of weak magnetic field, as we already mentioned, we can apply the perturbation theory. According to this theory, the corrections to the degenerate energy E_J (eigenvalues of $\mathrm{H_0}$) of any atomic level of total angular momentum quantum number J can be obtained by diagonalization of the magnetic Hamiltonian on the basis of the degenerate eigenvectors of $\mathrm{H_0}$ corresponding to the eigenvalues E_J. Since the unperturbed Hamiltonian $\mathrm{H_0}$ is invariant under rotation, J and M (the projection of J along an arbitrary z-axis) are good quantum numbers so that the eigenvectors of $\mathrm{H_0}$ can be written in the form $|JM\rangle$. This means that the corrections to the degenerate energy E_J can be obtained by diagonalization of the matrix $\langle JM|\mathrm{H_B}|JM'\rangle$. By choosing the quantization z-axis of total angular momentum along the magnetic field vector, one finds

$$\langle JM|\mathrm{H_B}|JM'\rangle \quad = \quad \mu_0 B g M \delta_{MM'}, \tag{3.11}$$

where g is the so-called Landé factor. In the Russell-Saunders coupling scheme (or L-S coupling scheme, where L and S are good quantum numbers) g can be written as:

$$g = \begin{cases} \frac{3}{2} + \frac{S(S+1)-L(L+1)}{2J(J+1)} & \text{if } J \neq 0 \\ 0 & \text{otherwise} \end{cases} \tag{3.12}$$

We find that to the first order of perturbation theory, the magnetic field removes the degeneracy of the atomic level, introducing the splitting of any atomic level of quantum number J in $(2J+1)$ equally spaced sublevels with possible values for $M = -J, ..., +J$. The splitting is proportional to the Landé factor g and to the magnetic field.
Let us now describe the Zeeman pattern arising in the transitions between two atomic levels, split by the presence of the magnetic field. We will consider the case of an electric-dipole interaction, which is the simplest and the most common case in the solar atmosphere. According to the selection rules for electric-dipole transitions, new transitions can occur between the new levels if $\Delta J = J_u - J_l = 0, \pm 1$ and $\Delta M = M_u - M_l = 0, \pm 1$ (indexes u and l stand for upper and lower energy levels of the transition). Transitions with $\Delta M = 0$ are called π-components, while the ones characterized by $\Delta M = \pm 1$ are called σ_b and σ_r components, respectively. The wavelength position corresponding to the π transition is the same as the original one while the wavelengths corresponding to the σ_b and σ_r components are shifted towards shorter or longer values (blue or red side of the spectrum) with respect to the unperturbed π transition. The shift is:

$$\Delta\lambda = \frac{e\lambda_0^2 B}{4\pi m_e c}(g_l M_l - g_u M_u). \tag{3.13}$$

The simplest case (referred as *normal Zeeman effect*) occurs when one of the levels involved in the transitions has angular momentum $J = 0$ or when the two levels have the

	$J_u = J_l + 1$	$J_u = J_l$	$J_u = J_l - 1$
$M_u = M_l + 1\ (\sigma_b)$	$\frac{3(J_u+M_u+1)(J_u+M_u+2)}{2(J_u+1)(2J_u+1)(2J_u+3)}$	$\frac{3(J_u-M_u)(J_u+M_u+1)}{2J_u(J_u+1)(2J_u+1)}$	$\frac{3(J_u-M_u)(J_u-M_u-1)}{2J_u(2J_u-1)(2J_u+1)}$
$M_u = M_l\ (\pi)$	$\frac{3(J_u-M_u+1)(J_u+M_u+1)}{(J_u+1)(2J_u+1)(2J_u+3)}$	$\frac{3M_u^2}{J_u(J_u+1)(2J_u+1)}$	$\frac{3(J_u-M_u)(J_u+M_u)}{2J_u(2J_u-1)(2J_u+1)}$
$M_u = M_l - 1\ (\sigma_r)$	$\frac{3(J_u-M_u+1)(J_u-M_u+2)}{2(J_u+1)(2J_u+1)(2J_u+3)}$	$\frac{3(J_u+M_u)(J_u-M_u+1)}{2J_u(J_u+1)(2J_u+1)}$	$\frac{3(J_u+M_u)(J_u+M_u-1)}{2J_u(2J_u-1)(2J_u+1)}$

Table 3.1: Analytical expressions for the normalized strength of the Zeeman components.

same value of the Landé factor. The number of the Zeeman components is 3 (σ_b, π and σ_r). Other cases are referred to as *anomalous Zeeman effect* and more complicated patterns occur.

The normalized strengths of the various components can be written as algebraic functions of M_l and M_u. They are summarized in Table 3.1. The strengths have symmetry properties, this means that for any σ_r (σ_b) component there is a σ_b (σ_r) component of the same strength symmetrical about line center, and for any π component (except the one corresponding to $M = M' = 0$, when it exists) there is another π component of the same strength symmetrical about line center. Note that the symmetry in wavelength is only valid in the Zeeman regime.

3.3 Paschen-Back effect

The case in which the magnetic field is strong enough to produce a J-level splitting comparable with the energy separation between different J-levels, is called the Paschen-Back effect. The perturbation theory presented for the Zeeman effect cannot be applied any longer. The energy levels have to be found by diagonalization of the total Hamiltonian H on the basis of the eigenvectors $|JM\rangle$ of H_0. This implies the evaluation of matrix elements of the form

$$\langle JM|\mathrm{H_B}|J'M'\rangle \quad = \quad \mu_0\langle JM|(L+2S)B|J'M'\rangle. \tag{3.14}$$

The eigenvalues and the eigenvectors of H can be found only by numerical methods in the general case. By choosing the quantization z-axis of total angular momentum along the magnetic field vector and assuming that the atomic system is exactly described by the L-S coupling scheme, the eigenstates of H_0 are of the form $|LS\,JM\rangle$. In this case the analytical calculation can be pushed further. We are not interested in showing the details of the calculations, that are completely described in Landi Degl'Innocenti & Landolfi (2004), our aim is to evaluate how the positions and strengths of the Zeeman components, in particular in the case of the He ɪ triplet, are affected when we are in the Paschen-Back effect regime. As a results of these calculations, it is found that the magnetic field produces a J-mixing of the various levels belonging to a particular term (L, S) so that the eigenvalues of the levels start to cross each other. J is not a good quantum number as it was in the Zeeman effect regime.

We have to distinguish between the *incomplete* and the *complete Paschen-Back effect regime*. The calculations (Landi Degl'Innocenti & Landolfi 2004) show that for intermediate values of the magnetic field, as we said, the eigenvalues of the levels start to

Line	Wavelength (Å)	Transition
He Ia	10829.0911	$2^3S_1 - 2^3P_0$ (Tr1)
He Ib	10830.2501	$2^3S_1 - 2^3P_1$ (Tr2)
He Ic	10830.3397	$2^3S_1 - 2^3P_2$ (Tr3)

Table 3.2: Line parameters.

cross each other and the linearity with the magnetic field is, in general, lost (incomplete Paschen-Back regime); for large values of the magnetic field, the positions behave again linearly with B (complete Paschen-Back regime). In the last case, the spin-orbit interaction can be considered as a perturbation in comparison to the magnetic interaction. The magnetic Hamiltonian is diagonal on the basis $|LS\,M_L M_S\rangle$ and the corrections to the energy eigenvalues are given by

$$\langle LS\,M_L M_S|\mathrm{H_B}|LS\,M_L M_S\rangle = \mu_0 B(M_L + 2M_S), \tag{3.15}$$

which explains their linear behavior with the magnetic field in the complete Paschen-Back regime. The term (L, S) splits into a number of components corresponding to particular values of $(M_L + 2M_S)$. As the magnetic field increases, going from the incomplete to the complete Paschen-Back regime, the energy eigenvectors gradually evolve from the form $|LS\,JM\rangle$ to $|LS\,M_L M_S\rangle$. The magnetic field induces a gradual basis-transformation on the energy eigenstates.

Since the spin-orbit coupling increases rapidly with increasing nuclear charge, the conditions for a strong field are met at much lower field with light atoms (such as helium) than with heavy atoms.

3.4 The He I 10830 Å lines

As an example of how the Zeeman effect acts on the atomic levels we consider the behavior of the lines that are the subject of this work: the He I 10830 Å triplet. They originate between the atomic levels 2^3S_1 and $2^3P_{2,1,0}$, comprising a 'blue' component at 10829.09 Å with $J_u = 0$ (Tr1), and two 'red' components at 10830.25 Å with $J_u = 1$ (Tr2) and at 10830.34 Å with $J_u = 2$ (Tr3) which are blended at solar chromospheric temperatures. The line parameters are summarized in Table 3.2.

The formation of the He I triplet in the solar chromosphere is due to two competing mechanisms (Andretta & Jones 1997). First, coronal photons penetrate in the upper chromosphere and photoionize neutral He atoms; these ions then recombine producing the He I lines. The second mechanism is due to direct collisional excitation produced by collisions with electrons at temperatures above 20000 K, in regions between chromosphere and corona. The major advantages of analyzing the He I lines are due to the fact that they are optically thin, narrow and are formed almost entirely in the upper chromosphere, meaning that there is no presence of any significant photospheric contributions (Avrett et al. 1994). We will see in the next paragraphs that in these conditions the radiative transfer equation for these lines can be solved analytically.

The components of the He I lines are sensitive to the Zeeman and the Paschen-Back

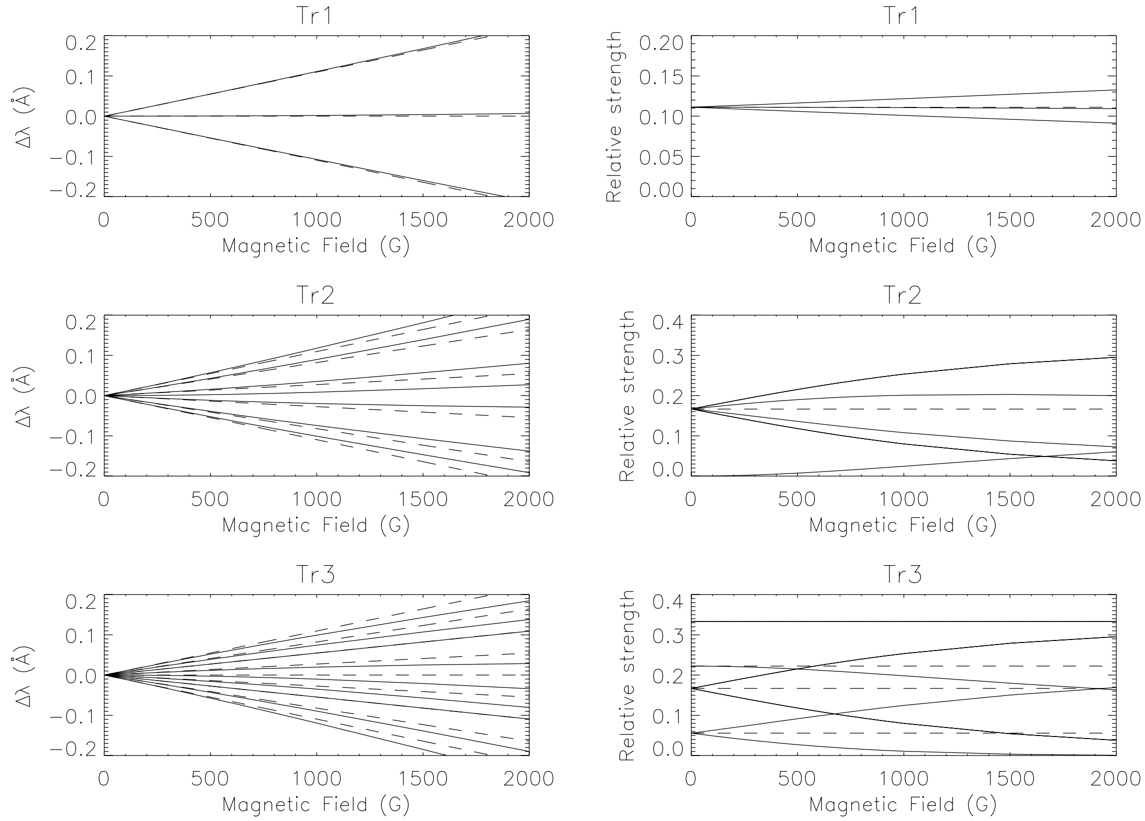

Figure 3.1: Positions and strengths of the Zeeman components as a function of the magnetic field. The solid lines represent calculations considering the incomplete Paschen-Back splitting (IPBS), while the dashed lines represent those using the linear Zeeman splitting (LZS) approximation. In the IPBS case, the Zeeman components exhibit asymmetric displacement and strengths. This figure has been produced using data kindly provided by Socas-Navarro et al. (see Fig. 1 of Socas-Navarro et al. 2005).

effect. Figure 3.1 shows the behavior of the positions and strengths of the Zeeman components as a function of the magnetic field for the three transitions from which the triplet originates. The calculations are performed in two different ways, by using the linear Zeeman slitting (LZS) approximation (dashed lines) and by taking into account the incomplete Paschen-Back splitting (IPBS; solid lines). The figure has been obtained using data kindly provided by Socas-Navarro et al. (Socas-Navarro et al. 2005). In the LZS case we can see that the behavior of the positions of the Zeeman components is the one we have described with central π components and symmetric σ_b and σ_r components shifted by the same amount with respect to the unperturbed π transition. The strengths are constant, they do not depend on the magnetic field.

In the IPBS case, the positions of the transitions are strongly influenced by the Paschen-Back effect, especially for magnetic field strengths above a few hundred Gauss. The relative strengths of the transitions also depend on the field strength. The incomplete Paschen-Back effect is to be considered for magnetic field strength values between 400 and 1500 G (Socas-Navarro et al. 2004).

3.5 Radiative transfer equation

The radiative transfer equation (RTE) in the presence of a magnetic field describes how a polarized light beam is transferred in a magnetized medium taking into account the changes of its polarization state due to the magnetic field. In the particular case of this thesis, the magnetized medium is the solar atmosphere. If we choose a z-axis along the direction of propagation of light and perpendicular to the solar surface, the RTE, usually, is written as

$$\frac{\mathrm{d}\mathbf{I}(z)}{\mathrm{d}z} = -\hat{k}[\mathbf{I}(z) - \mathbf{S}(z)] \tag{3.16}$$

where $\mathbf{I}$ is the Stokes vector $\mathbf{I}=(I, Q, U, V)$ emerging from the magnetized medium and $\mathbf{S}(z)$ the source function vector. In the case of local thermodynamic equilibrium (LTE), $\mathbf{S}(z)$ is the Planck function with a temperature corresponding to a local height z in the atmosphere, $\mathbf{B}(\mathrm{T}(z))$. Its radiation field is unpolarized: $\mathbf{S}(z)=(\mathrm{B}(z),0,0,0)$. $\hat{k}$ is the so-called *propagation matrix*.

Some manipulations can be done in order to shape the RTE into a useful form to describe the formation of spectral lines in an anisotropic medium. $\hat{k}$ can be rewritten taking into account contributions from both the continuum and line forming processes, so that

$$\hat{k} = k_c\mathbf{1} + k_{lin}\,\hat{\phi}, \tag{3.17}$$

where k_c is the continuum absorption coefficient, $\mathbf{1}$ is the 4×4 identity matrix, k_{lin} is the line absorption coefficient and $\hat{\phi}$ contains only the normalized absorption and dispersion profiles. Defining the *line to continuum absorption coefficient ratio,* $\eta_0 \equiv \frac{k_{lin}}{k_c}$, we can write

$$\hat{k} = k_c(\mathbf{1} + \eta_0\hat{\phi}). \tag{3.18}$$

Introducing the *continuum optical depth scale,* $\mathrm{d}\tau_c = -k_c\mathrm{d}z$ we can write the RTE in this form:

$$\frac{\mathrm{d}\mathbf{I}(\tau_c)}{\mathrm{d}\tau_c} = \hat{k}[\mathbf{I}(\tau_c) - \mathbf{S}(\tau_c)], \tag{3.19}$$

where

$$\hat{k} = \begin{pmatrix} \eta_I & \eta_Q & \eta_U & \eta_V \\ \eta_Q & \eta_I & \rho_V & -\rho_U \\ \eta_U & -\rho_V & \eta_I & \rho_Q \\ \eta_V & \rho_U & -\rho_Q & \eta_I \end{pmatrix}. \tag{3.20}$$

Following the calculus by Landi Degl'Innocenti & Landolfi (2004), the elements of the propagation matrix are expressed as:

$$\eta_I = 1 + \frac{\eta_0}{2}\left(\phi_p \sin^2\gamma + \frac{1}{2}[\phi_b + \phi_r](1 + \cos^2\gamma)\right), \tag{3.21}$$

$$\eta_Q = \frac{\eta_0}{2}\left(\phi_p - \frac{1}{2}[\phi_b + \phi_r]\right)\sin^2\gamma\cos 2\chi, \tag{3.22}$$

$$\begin{aligned}
\eta_U &= \frac{\eta_0}{2}\left(\phi_p - \frac{1}{2}[\phi_b + \phi_r]\right)\sin^2\gamma\sin 2\chi, && (3.23)\\
\eta_V &= \frac{\eta_0}{2}[\phi_r - \phi_b]\cos\gamma, && (3.24)\\
\rho_Q &= \eta_0\left(\psi_p - \frac{1}{2}[\psi_b + \psi_r]\right)\sin^2\gamma\cos 2\chi, && (3.25)\\
\rho_U &= \eta_0\left(\psi_p - \frac{1}{2}[\psi_b + \psi_r]\right)\sin^2\gamma\sin 2\chi, && (3.26)\\
\rho_V &= \frac{\eta_0}{2}[\psi_r - \psi_b]\cos\gamma. && (3.27)
\end{aligned}$$

The absorption and anomalous dispersion profiles are given by:

$$\begin{aligned}
\phi_j &= \sum_{i_j=1}^{N_j} s_{i_j} H(a, v + v_D + v_{i_j}), && (3.28)\\
\psi_j &= 2\sum_{i_j=1}^{N_j} s_{i_j} F(a, v + v_D + v_{i_j}), && (3.29)
\end{aligned}$$

In equations 3.21- 3.29, $j = b, p, r$ refer to the Zeeman components σ_b, π and σ_r. s_{i_j} are the normalized strength of the various Zeeman components summarized in Table 3.1 and the summation over $i_j = 1, ..., N_j$, indicates that in the calculation of the absorption and dispersion profiles, all the Zeeman components have to be taken into account. The functions H and F are the Voigt and the Faraday functions at a given damping a and a given distance from line center, λ_0, in units of Doppler width, $v = \frac{\lambda - \lambda_0}{\Delta\lambda_D}$.

$$\begin{aligned}
H(a, v') &= \frac{a}{\pi}\int_{-\infty}^{+\infty} \frac{e^{-y^2}}{(v' - y)^2 + a^2}\mathrm{d}y && (3.30)\\
F(a, v') &= \frac{1}{2\pi}\int_{-\infty}^{+\infty} \frac{(v' - y)e^{-y^2}}{(v' - y)^2 + a^2}\mathrm{d}y && (3.31)
\end{aligned}$$

For each component of the Zeeman pattern we have a shift of the central position due to two factors: the Doppler effect and the Zeeman splitting. The first takes into account the wavelength shift, equal for all the Zeeman components, due to a net macroscopic velocity along the vertical axis, v_z, so that:

$$v_D = \frac{v_z \lambda_0}{c\Delta\lambda_D}. \qquad (3.32)$$

The Zeeman splitting causes a shift of the absorption and the dispersion profiles of each component of the Zeeman pattern by: $v_{i_j} = \frac{\Delta\lambda_{i_j}}{\Delta\lambda_D}$ with $\Delta\lambda_{i_j}$ given in Eq. 3.13.
The damping a and the Doppler width $\Delta\lambda_D$ are expressed as follows:

$$\begin{aligned}
a &= \frac{\lambda_0^2}{4\pi c\Delta\lambda_D}\Gamma, && (3.33)\\
\Delta\lambda_D &= \frac{\lambda_0}{c}\left(\frac{2KT}{M} + v_{mic}^2\right)^{1/2}, && (3.34)
\end{aligned}$$

where Γ is the damping factor given by two contributions, Γ_{rad} and Γ_{col}, respectively, the radiative and the collisional line broadening parameters. $\Delta\lambda_D$ is calculated for a given temperature T and microturbulent velocity v_{mic}.
The angles γ and χ are the inclination and azimuthal angle of the magnetic field vector with respect to the observer line-of-sight (LOS).
When the LOS is not aligned with the z-axis then, in a plane parallel atmosphere, the RTE has to be written as:

$$\mu \frac{\mathrm{d}\mathbf{I}(z)}{\mathrm{d}z} = -\hat{k}[\mathbf{I}(z) - \mathbf{S}(z)] \tag{3.35}$$

with $\mu = \cos\theta$ and θ is the angle between the line-of-sight (LOS) and the z-axis. In the Eq. 3.32, v_z becomes v_{LOS} and in order to write the RTE in the same form as in the Eq. 3.19 we have to define the optical depth scale along the LOS as $\mathrm{d}\tau_c^{LOS} = -(k_c/\mu)\mathrm{d}z$.

3.6 Solution of the RTE

In order to solve the RTE we introduce the *evolution operator* $\hat{O}(\tau_c, \tau_c')$ that, in absence of any emission along the path, acts on the Stokes vector transforming it as seen at an optical depth τ_c to another optical depth location τ_c' in this way:

$$\mathbf{I}^*(\tau_c) = \hat{O}(\tau_c, \tau_c')\mathbf{I}^*(\tau_c'). \tag{3.36}$$

The index * indicates the solution for the homogenous equation associated with the non-homogenous differential equation 3.19.
$\hat{O}(\tau_c, \tau_c')$ fulfills the following properties:

$$\hat{O}(\tau_c, \tau_c) = \mathbf{1} \tag{3.37}$$

$$\hat{O}(\tau_c, \tau_c'') = \hat{O}(\tau_c, \tau_c')\hat{O}(\tau_c', \tau_c''). \tag{3.38}$$

It can be used as an integration factor of the Eq. 3.19 to obtain:

$$\mathbf{I}(\tau_1) = \hat{O}(\tau_1, \tau_0)\mathbf{I}(\tau_0) - \int_{\tau_0}^{\tau_1} \hat{O}(\tau_1, \tau_c)\hat{(}\tau_c)\mathbf{S}(\tau_c)\mathrm{d}\tau_c \tag{3.39}$$

where τ_0 and τ_1 are two optical depth points, indicating the bottom and the top points of the medium under study. Considering that the observer is located at $\tau_1 = 0$, then if the inner point is chosen to be deep enough ($\tau_0 \to \infty$), the atmosphere is so optically thick that no radiation emitted at τ_0 can reach the observer:

$$\lim_{\tau_0 \to \infty} \hat{O}(0, \tau_0)\mathbf{I}(\tau_0) = 0. \tag{3.40}$$

Finally, combining Eq. 3.38 and 3.39 we obtain the formal solution of the RTE:

$$\mathbf{I}(0) = \int_0^\infty \hat{O}(0, \tau_c)\hat{k}(\tau_c)\mathbf{S}(\tau_c)\mathrm{d}\tau_c. \tag{3.41}$$

There are no analytical ways to know the evolution operator for a general atmosphere. It has to be evaluated numerically.

3.6.1 Milne-Eddington approximation

In the case in which the propagation matrix is height-independent $\hat{k}(\tau_c) = \hat{k}_0$, i.e. constant throughout the atmosphere and the source function varies linearly with optical depth $\mathbf{S}(\tau_c) = (S_0 + S_1\tau_c, 0, 0, 0)$, we are in the *Milne-Eddington approximation*. In this case, the expression of the evolution operator can be evaluated. From its properties we can derive the following differential equation:

$$\frac{\mathrm{d}\hat{O}(\tau_c, \tau_c')}{\mathrm{d}\tau_c} = \hat{k}(\tau_c)\hat{O}(\tau_c', \tau_c). \tag{3.42}$$

In the particular case of the Milne-Eddington approximation the equation can be integrated and we obtain:

$$\hat{O}(0, \tau_c) = e^{-\int_0^{\tau_c} \hat{k}(t)\mathrm{d}t}. \tag{3.43}$$

The Eq. 3.41 becomes:

$$\mathbf{I}(0) = \int_0^{\infty} e^{-\hat{k}_0\tau_c}\hat{k}_0(S_0 + S_1\tau_c)\mathrm{d}\tau_c \tag{3.44}$$

It is possible now to solve this equation analytically and to obtain the explicit expressions of the 4 Stokes parameters. The solution is also known as the Unno-Rachkowsky solution of the transfer equation (Unno 1956, Rachkowsky 1962, 1967):

$$I(0) = S_0 + \frac{\eta_I}{\Delta}[\eta_I^2 + \rho_Q^2 + \rho_U^2\rho_V^2]S_1 \tag{3.45}$$

$$Q(0) = -\frac{S_1}{\Delta}[\eta_I^2\eta_Q + \eta_I(\eta_V\rho_U - \eta_U\rho_V) + \rho_Q R] \tag{3.46}$$

$$U(0) = -\frac{S_1}{\Delta}[\eta_I^2\eta_U + \eta_I(\eta_Q\rho_V - \eta_V\rho_Q) + \rho_U R] \tag{3.47}$$

$$V(0) = -\frac{S_1}{\Delta}[\eta_I^2\eta_V + \eta_I(\eta_U\rho_Q - \eta_Q\rho_U) + \rho_V R] \tag{3.48}$$

where

$$\Delta = \eta_I^2(\eta_I^2 - \eta_Q^2 - \eta_U^2 - \eta_V^2 + \rho_Q^2 + \rho_U^2 + \rho_V^2) - R^2 \tag{3.49}$$

$$R = \eta_Q\rho_Q + \eta_U\rho_U + \eta_V\rho_V. \tag{3.50}$$

3.7 Inversion of Stokes profiles

In this thesis we are interested in retrieving information on the full magnetic field vector, the line-of-sight velocity and other physical quantities in the solar upper chromosphere by inverting the Stokes profiles of the He I 10830 Å multiplet lines starting from their spectropolarimetric observations. The basic idea of an inversion code is to produce synthetic profiles using an atmospheric input model by solving the RTE. The initial guess atmosphere is a given set of parameters defining the relevant physical quantities of the atmospheric layer under study, in which the lines are formed. Once the synthetic profiles are obtained, they are compared with the observed ones and the initial atmosphere is then iteratively modified by means of a χ^2 minimization algorithm until a best fit to the observations is achieved.

3.7.1 HeLIx

To analyze the Stokes profiles obtained in the He I 10830 Å wavelength range we use the code HeLIx (Linefit He-Line Information Extractor) described in the paper of Lagg et al. (2004). It is based on a simple Milne-Eddington model for describing the radiative transfer in the He I 10830 Å multiplet lines. This approach is justified since the lines, as we already mentioned in the Par. 3.4, show weak saturation and are almost optically thin. It is also reasonable because due to the lack of knowledge of the conditions of their formation, a more complicated solution of the RTE is not justified.

The arbitrary initial atmosphere is made up of 8 parameters assuming a Voigt profile for the Zeeman components of the spectral lines. This set of initial guess parameters is defined as an *atmospheric component*. The free parameters are: the magnetic field strength B and direction (inclination angle γ and azimuthal angle χ), line-of-sight velocity v_{LOS}, Doppler width $\Delta\lambda_D$, damping factor Γ in units of velocity of light, the ratio of the line center to the continuum intensity η_0 and the gradient of the source function S_1. We have defined all these parameters in the previous paragraphs. The source function at $\tau = 0$ (solar surface) is eliminated as a free parameter by considering that the intensity of the unpolarized signal I outside the line must be equal to the observed continuum intensity I_c: $S_0 + \mu S_1 = I_c$.

The fit to the observed profiles is based on a minimization of the function δ, the goodness of fit function:

$$\begin{aligned}\delta = &\sum \omega_I(I_{\text{obs}} - I_{\text{syn}})/(I_{\text{c}}\sigma_I)\\ &+ \sum \omega_Q(Q_{\text{obs}} - Q_{\text{syn}})/\sigma_Q\\ &+ \sum \omega_U(U_{\text{obs}} - U_{\text{syn}})/\sigma_U\\ &+ \sum \omega_V(V_{\text{obs}} - V_{\text{syn}})/\sigma_V,\end{aligned} \tag{3.51}$$

where the sum runs over n wavelength points of the profiles, the subscripts "obs" and "syn" refer to observed and synthesized Stokes profiles respectively, $\sigma_{I,Q,U,V}$ are parameters defining the strength of the signal

$$\sigma_I = \frac{1}{n}\sum_\lambda |I_{\text{obs}}/I_{\text{c}} - 1|, \tag{3.52}$$

$$\sigma_{Q,U,V} = \frac{1}{n}\sum_\lambda |(Q,U,V)_{\text{obs}}|, \tag{3.53}$$

and $\omega_{Q,U,V}$ are the wavelength dependent weighting functions.

To ensure that this optimization process finds the global minimum of δ in the parameter space, the code uses the genetic algorithm PIKAIA (Charbonneau 1995). The robustness of a genetic algorithm is higher compared with that of a standard minimization routine, such as the Levenberg-Marquardt technique. It finds the global minimum in the multidimensional hypersurface independent of the initial parameter values and allows us to specify a range for every parameter to be fitted in order to guarantee that the result of the inversion stays within the regime of physically useful solutions. The disadvantage is higher computation time. Since in this case the synthesized profiles are calculated using

Milne-Eddington atmospheres, the computation time is not so critical so that the preference can be given to the robustness of the fit. For the PIKAIA algorithm the fitness function is defined as $f = 1/\delta$.
The code includes a treatment of the Hanle effect for a special geometry case. The Hanle effect modifies the He lines' linear polarization signal due to atomic polarization, creating a complicated dependence of the linear polarization on magnetic field strength, direction and viewing geometry. For a detailed presentation of the theory of the atomic polarization and the Hanle effect see, e.g., Trujillo Bueno (2001), Trujillo Bueno et al. (2002). The main observational characteristics are Q or U profiles of the same shape as Stokes I, but with opposite signs for the He ɪa line and the He ɪb–He ɪc blend. In the special case of a LOS direction perpendicular to the solar surface (disc center) and a magnetic field inclined with respect to the local vertical, the Hanle effect creates measurable linear polarization in the He ɪ multiplet (Trujillo Bueno et al. 2002). The He ɪ 10830 line needs also to be in the saturated Hanle effect that occurs for magnetic strength larger than a few Gauss. Choosing as a reference direction for Stokes Q the projection direction of the magnetic field vector on the solar surface and the magnetic field is more inclined than the Van Vleck's angle (54.73°), then $Q < 0$ in the He ɪa line and $Q > 0$ in the He ɪb and He ɪc line. If the field is less inclined than 54.73° then $Q > 0$ in the He ɪa line and $Q < 0$ in the He ɪb and He ɪc line (Trujillo Bueno 2003). With these settings, we can use the following relation $\tan(2\chi) = (U/Q)$ to infer the azimuth of the magnetic field vector. This is the magnetic field direction along which the polarization signal due to Hanle effect is oriented.

3.7.2 Multi-component inversion

In the observations we will present and analyze in this thesis, we have to deal with the presence of different unresolved atmospheric components of the He lines, coexisting in the same resolution element. Due to the limited spatial resolution of the observations multiple components may well be present in some resolution elements. The code allows inversions of a single spectrum using multiple atmospheric components. This leads to an increase of the number of free parameters. These atmospheric components are mixed via a filling factor, α, defining the contribution of an atmospheric component to the total observed profile. The sum of the filling factors of all atmospheric components within a resolution element is required to be unity. To limit the number of free parameters in a multi-component atmosphere the code allows for coupling between different parameters. In the chapter in which the observed profiles will be described we will give details of our way to proceed in facing the high number of parameters.

4 Inversions of the He I 10830 Å Stokes profiles: The influence of the Paschen-Back effect

4.1 Introduction

In previous papers (Rüedi et al. 1995, Solanki et al. 2003, Lagg et al. 2004) the analysis of the observed polarization in the He I 10830 Å multiplet for the determination of the magnetic field vector was carried out considering the linear Zeeman splitting (LZS) approximation. Socas-Navarro et al. (2004) demonstrated that the magnetic field vector from spectropolarimetry in the He I 10830 Å multiplet must be determined by considering the wavelength positions and the strengths of the Zeeman components in the incomplete Paschen-Back splitting regime (IPBS). They demonstrated that neglecting the Paschen-Back effect results in significant errors in the calculation of its polarization profiles. For example, Socas-Navarro et al. (2004) pointed out that the Paschen-Back effect produces a $\sim 25\%$ reduction in the amplitude of the red component, which implies that the linear Zeeman effect theory underestimates the magnetic field strength. In the previous chapter the theory of the Zeeman and the Paschen-Back effects was presented.

The shift in wavelength position and the asymmetric change of the strengths between the blue and the red Zeeman sublevels shown in Fig. 3.1 introduce asymmetries in the resulting Stokes Q, U and V profiles. In their paper Socas-Navarro et al. (2004) show that this asymmetry is strong enough to produce a measurable effect in the observations.

Within the scope of this thesis the Paschen-Back effect was implemented into the HeLIx code.

In this chapter we present systematic tests of the influence of the Paschen-Back effect on parameters retrieved from Stokes profile observations of the He I triplet. We pay particular attention to the asymmetry of the Stokes V-profile. This parameter is often used to diagnose combined gradients of the velocity and the magnetic field along the line of sight, but the IPBS also introduces an asymmetry into the Stokes V-profiles. It is therefore of considerable interest to see if the asymmetry seen in many Stokes V-profiles of the He I 10830 Å triplet is due to the IPBS, or if this line parameter provides information on the structure of the upper solar chromosphere.

4.2 Methods and results

In order to calculate the Zeeman components and strengths of the He I 10830 Å multiplet in the IPBS regime, we have improved the numerical code HELIX for the synthesis and inversion of Stokes profiles in a Milne-Eddington atmosphere (Lagg et al. 2004), by using the polynomial approximants as proposed by Socas-Navarro et al. (2005). The positions and strengths of the various components of the Zeeman structure of the multiplet are approximated by polynomials.

Fig. 4.1 compares the synthetic Stokes profiles of the He I 10830 Å multiplet for a 50 G and a 1000 G field, inclined by 30° with respect to the line of sight, obtained considering LZS only and including the IPBS. The difference between the profiles obtained when considering the IPBS (dotted line) or the LZS (dashed line) approximation, is clearly evident. For example, the Q and U profiles are symmetric and the V profiles antisymmetric in the LZS case, while they are all asymmetric in the presence of IPBS. Moreover, if we compare the two panels we can see that the absolute difference between the profiles calculated using IPBS and LZS, increases with increasing magnetic field strength although the relative difference remains roughly the same (note the different vertical scales in the top and bottom parts of the figure).

4.2.1 Inversion of synthetic profiles

In a next step we analyzed the effect of the IPBS on synthetic Stokes profiles by estimating the error we make when retrieving the values of the physical parameters (such as the magnetic field vector, the LOS-velocity, etc.) by using LZS instead of IPBS. For this purpose we calculated synthetic profiles including IPBS, which are taken to represent an observation. We then inverted these IPBS profiles assuming LZS only. The difference between the original magnetic field and velocity values and the values retrieved from the LZS inversion are displayed in Fig. 4.2. We see, in both panels, a significant deviation of the retrieved values from the correct ones, indicated by the solid line at ordinate 0. More precisely, the error introduced by neglecting the IPBS increases with the strength of the magnetic field for both parameters and, for the LOS-velocity, it decreases with increasing inclination γ of the magnetic field to the LOS. Neglecting IPBS gives artificial downflows of up to 350 m/s. On average the field strength is underestimated by 16% if IPBS is neglected, with the exact fraction lying in the range 14-18% depending on the magnetic field's inclination γ and its azimuth, χ.

The same analysis for the inclination and the azimuthal angle of the magnetic field shows that these two parameters are accurately retrieved by inversions even in the LZS approximation.

4.2.2 Inversion of observational data

We can now do a similar analysis using the observational data. We choose the observations of the emerging flux region NOAA 9451 located at 33° W, 22° S that were recorded with the Tenerife Infrared Polarimeter (TIP-I; Martínez Pillet et al. 1999) mounted behind the Echelle spectrograph on the Vacuum Tower Telescope (VTT) at the Teide observatory on Tenerife (in the next chapter, a brief description of the instruments we used will be

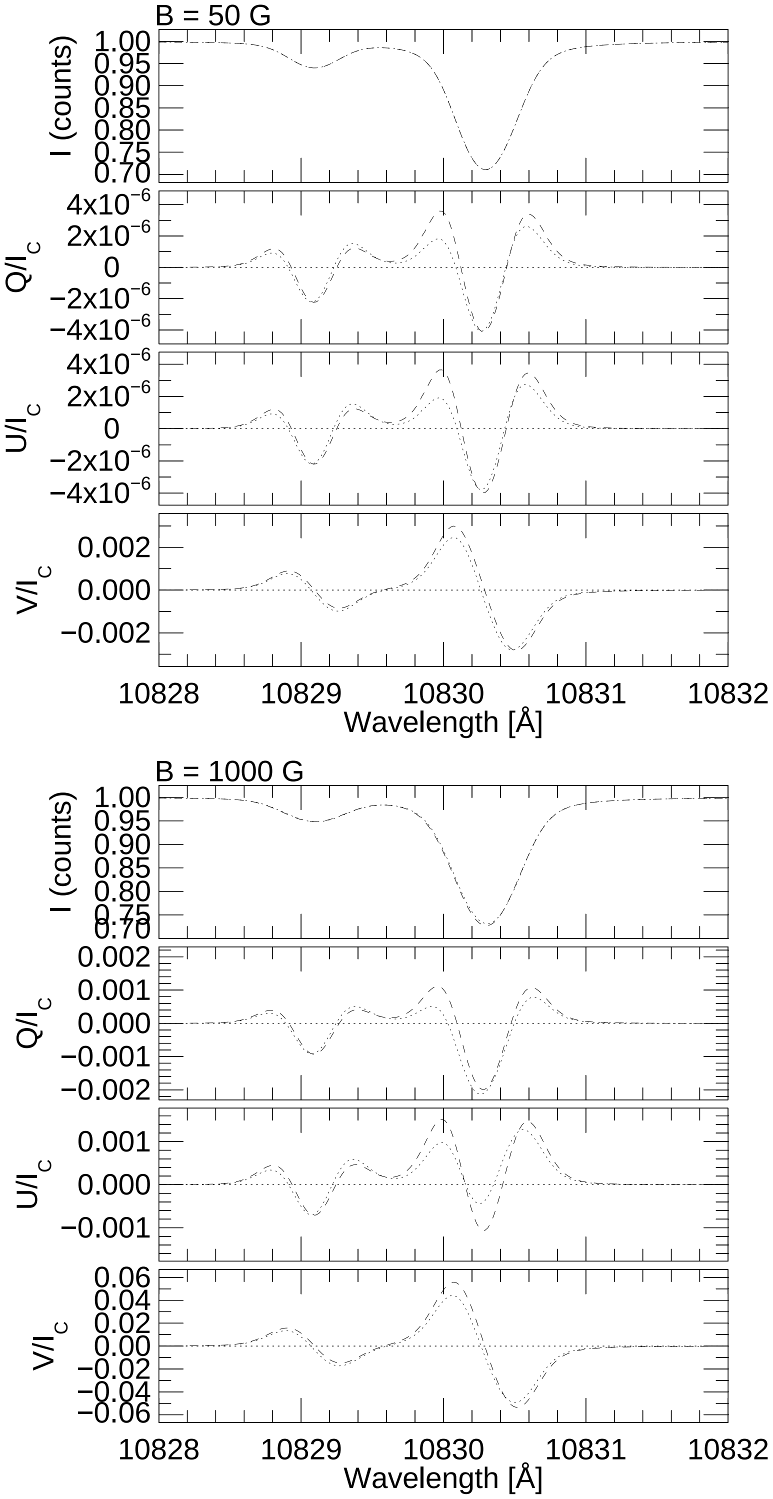

Figure 4.1: Synthetic Stokes profiles of the He I 10830 Å triplet, assuming a 50 G (top) and a 1000 G (bottom) field, respectively, inclined by 30° with respect to the line of sight. The Milne-Eddington parameters we have used for this synthesis are: $\chi = 22.5^\circ$, $v_{\rm LOS} = 0.0$ m/s, $a = 0.3$, $\Delta\lambda_{\rm D} = 0.2$ Å, $\eta_0 = 5.0$ and $\mu S_1 = 1.0$. (For the notation, see Sect. 3.7.1). The dotted profile is obtained by considering the IPBS, while the dashed one is obtained in the LZS approximation. The reference direction for Stokes Q is along the $+y$-axis of the maps in Fig. 4.3.

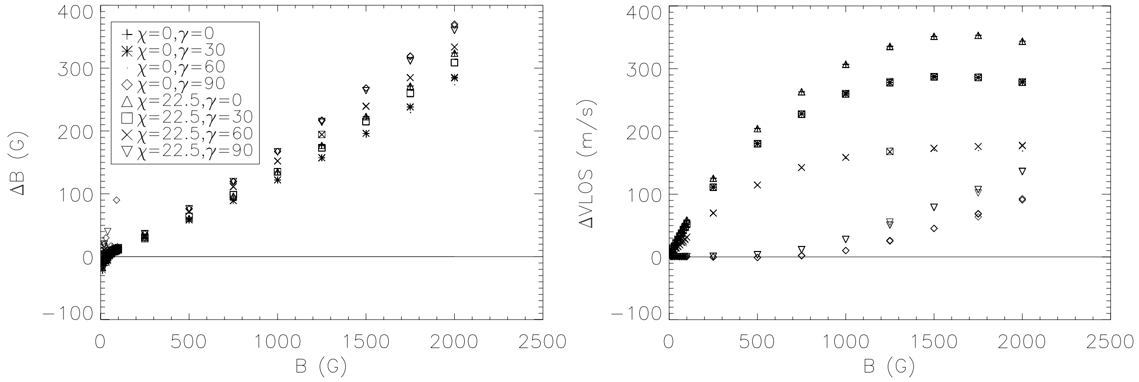

Figure 4.2: On the left: Difference between the values of the magnetic field strength for a synthetic profile computed including IPBS and the ones obtained from the LZS inversion of this synthetic IPBS profile (ΔB), as a function of the magnetic field strength of the synthetic profile for different inclination (γ) and azimuthal angles (χ) of the magnetic field vector (in degrees). On the right: The same for the LOS-velocity. The retrieved values for magnetic field (left) and LOS-velocity (right) deviate significantly from the correct values (horizontal solid line).

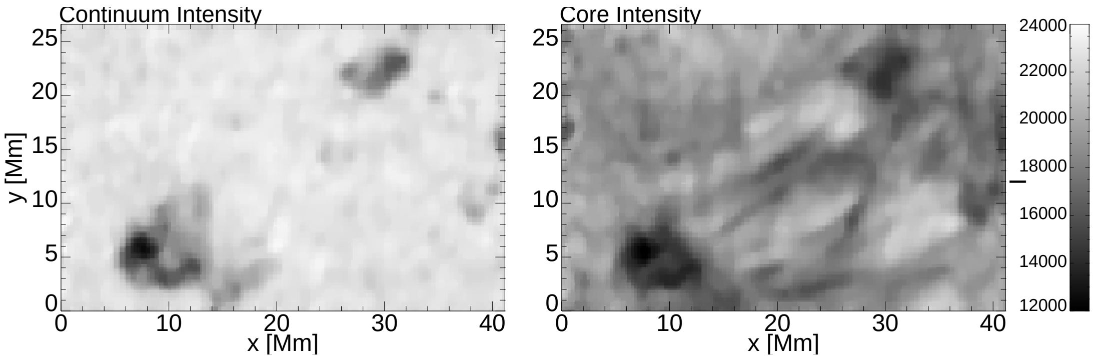

Figure 4.3: Continuum (left) and He core (right) intensity maps of an emerging flux region (NOAA active region 9451, 33° W, 22° S)

given). Figure 4.3 displays Stokes *I* maps for the observed region in the continuum and in the core of the He ɪ line. This active region was previously studied assuming LZS (Solanki et al. 2003, Lagg et al. 2004). We chose this particular observation for analysis partly because Socas-Navarro et al. (2004) suggest that some IPBS signatures described in their paper could be present in this observation, referring, in particular, to profile asymmetries. This data set is inverted twice, once in the LZS approximation and once including IPBS. All other particulars of the inversion remain unchanged. We consider the error in the retrieved value of the magnetic field strength if LZS is assumed when carrying out the inversions. Figure 4.4 confirms the result shown in Fig. 4.2 that the retrieved magnetic field values are roughly 16% higher using the IPBS inversions. This result is also clearly displayed in the two maps of Fig. 4.5. It implies that the field strengths at the chromospheric level in this region were underestimated by on average 16% by Solanki et al. (2003) and Lagg et al. (2004). We do not expect, however, that any of the main conclusions of these publications (or of Wiegelmann et al. 2005) are affected.

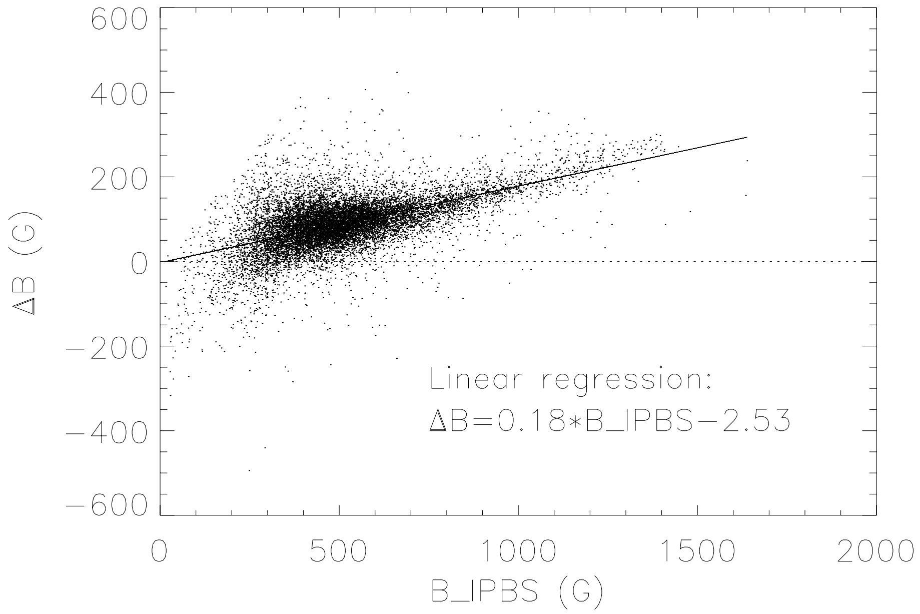

Figure 4.4: Influence of IPBS on the retrieval of the magnetic field strength for NOAA 9451. Difference in field strength, ΔB, deduced from inversions including the IPBS, B_{IPBS}, and those without it, versus B_{IPBS}. The solid line represents a linear regression. The larger scatter present in the figure for $B_{IPBS} \leq 800$ G is due to the noise that affects the observation.

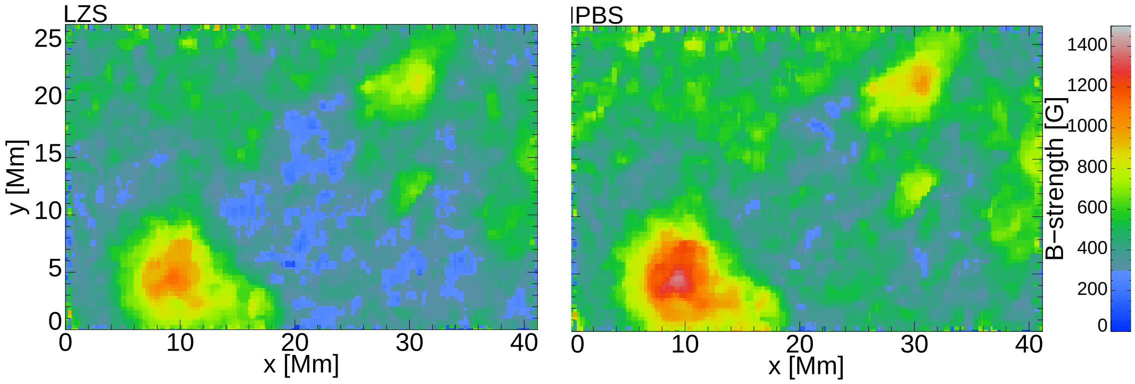

Figure 4.5: Maps of magnetic field strength of the active region shown in Fig. 4.3. Left frame: result of an inversion assuming LZS; right frame: the same, but with IPBS. Note that both images have the same color scale.

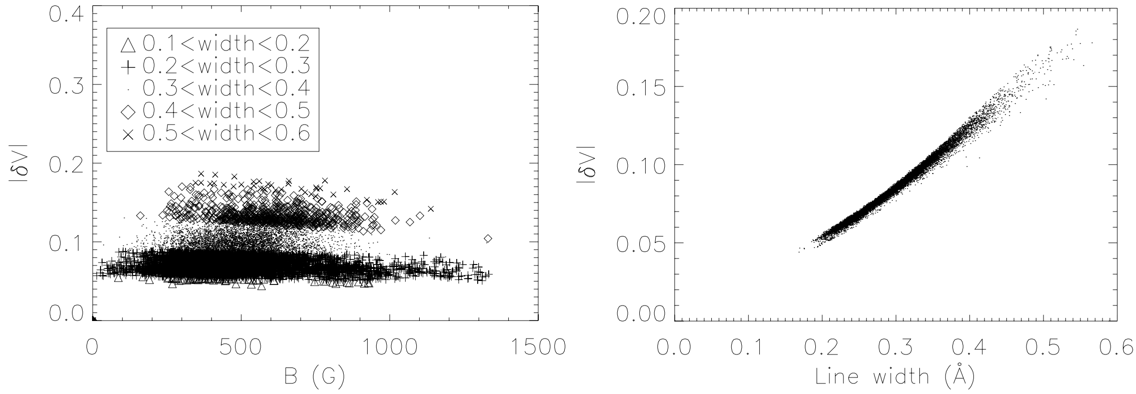

Figure 4.6: Left: Absolute value of the relative broad-band circular polarization ($|\delta V|$) of synthetic IPBS V-profiles as a function of the magnetic field strength. The symbols distinguish between different ranges of the e-folding width of the lines. Right: $|\delta V|$ as a function of the width of the lines.

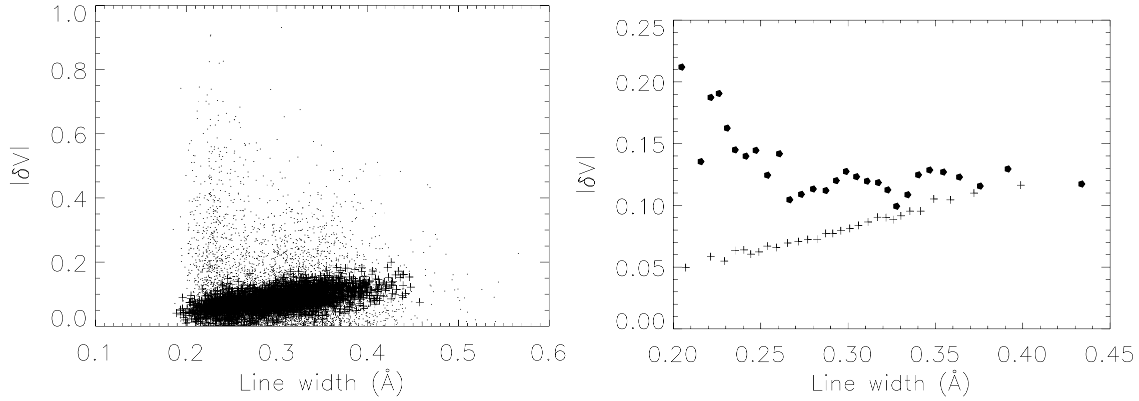

Figure 4.7: Left: Absolute value of the relative broad-band circular polarization of the fitted, synthetic IPBS V-profiles (crosses) to which we have added random noise and of the observed V-profiles (dots) as a function of the line width. Right: The same, but here the values are averaged over bins containing the same number of points.

4.2.3 Stokes *V* asymmetry

In this section we evaluate the influence of the Paschen-Back effect on the Stokes V-profile relative area asymmetry defined as (Solanki & Stenflo 1984)

$$\delta\mathcal{A} = \frac{A_b - A_r}{A_b + A_r}, \tag{4.1}$$

where A_b and A_r (both positive) are, respectively, the areas of the blue and the red Stokes V-profile wings. The parameter $\delta\mathcal{A}$ is often used to provide information on the LOS gradient of the velocity and of B$\cos\gamma$ in the height range of line formation (e.g. Solanki 1993). An alternative to this definition, which is more easily applicable to a whole multiplet (including complex-shaped profiles; Lagg et al. 2007), is the relative broad-band circular polarization

$$\delta V = \frac{\int_{-\infty}^{+\infty} V(\lambda) d\lambda}{\int_{-\infty}^{+\infty} |V(\lambda)| d\lambda}. \tag{4.2}$$

Socas-Navarro et al. (2004) investigated how the area asymmetry produced by the Paschen-Back effect varies with the magnetic field strength and pointed out that for a typical Doppler width of 105 mÅ, $|\delta V| \approx 0.11$ for $B < 1000$ G, which suggests that significantly larger observed values of $|\delta V|$ cannot be solely due to the effects of Paschen-Back effect splitting if the inferred B turns out to be smaller or similar to 1000 G.

In Fig. 4.6 (left panel) we plot the absolute value of the relative broad-band circular polarization ($|\delta V|$) of the best-fit IPBS V-profiles to the observed profiles as a function of the magnetic field strength for different ranges of the values of the e-folding width of the lines. The δV is calculated over the whole wavelength range of the He multiplet. The $|\delta V|$ of the best-fit synthetic IPBS V-profiles is nearly independent of B, but is a strong function of the width of the lines, as indicated by different symbols. This behavior is displayed more clearly in the right panel of Fig. 4.6 where we plot $|\delta V|$ as a function of the width of the lines. We expect that the $|\delta V|$ of the observed profiles should exhibit a similar dependence, if $|\delta V|$ solely results from the IPBS. The $|\delta V|$ of the observed profiles (see dots in Fig. 4.7, left panel) clearly shows no such dependence. In order to test if noise is the reason for the lack of this dependence we add random noise to the synthetic IPBS V-profile of the same order as the one we have in the observational data. We restrict our analysis to synthetic profiles with a maximum V-signal at least three times higher than the noise level and to the corresponding observed profiles. The $|\delta V|$ of synthetic, noisy IPBS V-profiles (represented by crosses in the left panel of Fig. 4.7) retains the dependence on the width of the lines. Fig. 4.7 (left) shows that the observed $|\delta V|$ values can be up to 4 times as large as those of the synthetic profiles. Values of the observed $|\delta V| \geq 0.2$ cannot be explained by IPBS or noise. The difference between the two sets of $|\delta V|$ values is displayed more markedly in the right panel of Fig. 4.7, where the values are grouped into bins containing the same number of points. For each bin the mean value is displayed in the x- and y-coordinates. Moreover, the difference between the δV values of the synthetic IPBS V-profiles and of the observed V-profiles is even larger than suggested by Fig. 4.7 because, for 54% of the profiles, they have the opposite sign.

In Fig. 4.8 we analyze, in particular, the observed profiles at position $x = 9$ Mm, $y = 4$ Mm of Fig. 4.3. We tried to reproduce the observed profile (solid line in Fig. 4.8) by running the inversion considering the LZS approximation (dashed line) or IPBS (dotted line). The synthetic I profiles are almost indistinguishable and they agree well with the observed profile. For the case where the IPBS is included, the fit appears to be somewhat worse for the Q, U, and V Stokes profiles. The IPBS inversion also fails to reproduce the asymmetries of the observed V profile. The Stokes V zero-crossing for the ’red’ components of the triplet (Tr2+Tr3) is also better reproduced by the LZS inversion. However, the relevant atmospheric parameters returned by both fits are almost unaffected whether IPBS is included or not.

Consequently, another mechanism must be acting to produce at least the larger values of the asymmetry. The most obvious one is the combination of velocity and magnetic-field gradients (see Solanki 1993, for a review). Support for this mechanism comes from

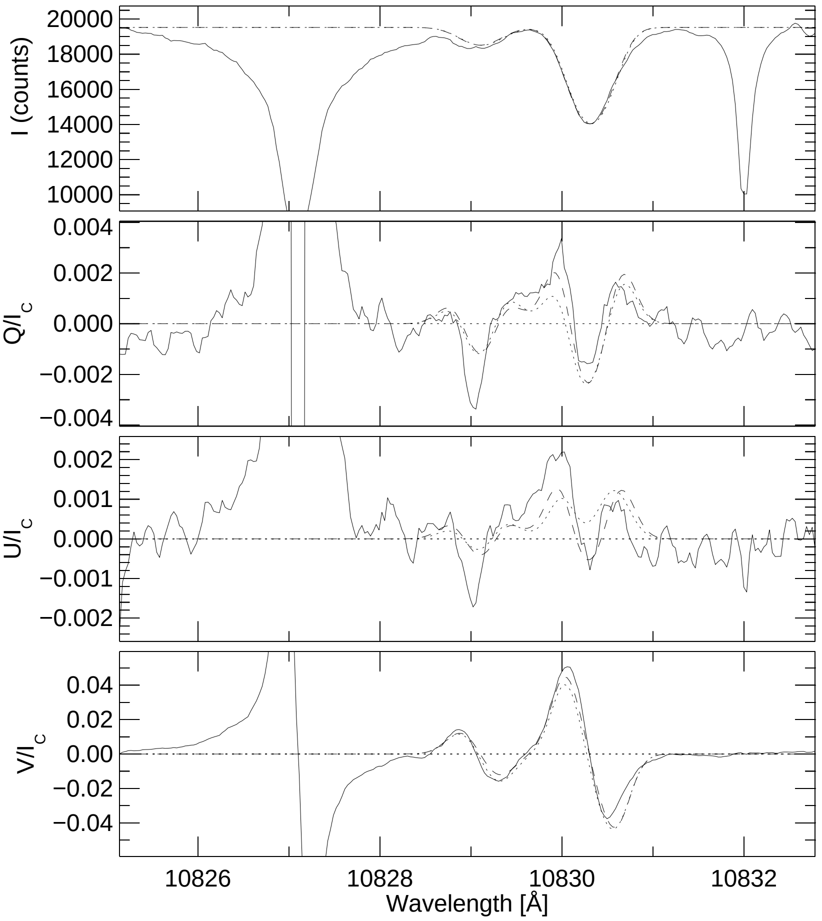

Figure 4.8: Stokes I, Q, U and V profiles at position $x = 9$ Mm, $y = 4$ Mm of Fig. 4.3. The observed profile is the solid line, the profile obtained from the inversion done considering the LZS is the dashed line and the one obtained using IPBS is the dotted line.

the fact that the observed δV is larger for narrow lines, for which smaller velocity and magnetic-field gradients are required to produce a large δV (Grossmann-Doerth et al. 1989).

4.3 Conclusions

We analyzed the influence of the Paschen-Back effect on the Stokes profiles of the He I 10830 Å multiplet lines, estimating its relevance using synthetic profiles and investigating its influence on the inversion of a spectropolarimetric scan of an emerging active region.
Our results support the conclusion of Socas-Navarro et al. (2004) that IPBS should be taken into account when modeling the polarization profiles of the He I 10830 multiplet. For example, we found that by including the incomplete Paschen-Back effect into our inversion code, on average 16% higher field strength values are retrieved from inversions, while other atmospheric parameters are affected less significantly.
We also showed that the Paschen-Back effect is not the main cause of the area asymmetry exhibited by the many He I 10830 Stokes profiles that showed a line width smaller than

$\sim$ 0.30 Å in Lagg et al.'s (2004) emerging flux region observation. The spatial points corresponding to such Stokes V-profiles are those for which the inferred value of the magnetic field strength is lower than $\sim$ 1.1 kG when IPBS is taken into account. The fact that the area asymmetry of the observed V-profiles is considerably stronger than of the synthetic V-profiles indicates that some other effect drives the area asymmetry more strongly than the Paschen-Back effect. The main candidates are LOS-gradients of the magnetic field vector and the velocity.

5 Observations

In this chapter we will introduce the spectropolarimetric observations of a filament located in an active region, obtained in May 2005. The observations follow the change of the magnetic structure of the filament resulting in interesting different features visible in the He ɪ 10830 Å Stokes profiles. In the first section, a brief description of the instruments we used to obtain the data is also given.

5.1 Instruments

The data presented in this thesis were recorded with two different instruments mounted at the 70 cm aperture Vacuum Tower Telescope (VTT) at the Teide observatory in Tenerife. The observations analyzed in Chap. 4 were obtained with the Tenerife Infrared Polarimeter (TIP-I; Martínez Pillet et al. 1999), while the data presented in this chapter were recorded with the update of the TIP-I, the second generation Tenerife Infrared Polarimeter TIP-II (Collados et al. 2007). In combination with the main spectrograph of the VTT, both instruments are able to obtain full Stokes spectropolarimetric data with high spectral resolution in the infrared region of the solar spectrum (1–1.8 μm). The new TIP-II instrument has a larger detector with more pixels compared to the TIP-I and it allows for a spectral window of 11 Å around the He 10830 Å line to be observed with a wavelength dispersion of 11 mÅ per pixel. The TIP-I instrument covered a shorter range of wavelengths of 8 Å. The data we are going to analyze in the following sections were obtained in the first campaign done with the new TIP-II instrument. The wider range of wavelength turned out to be absolutely necessary to cover the full range of possible He absorption signatures observed during the evolution of the filament. For example, in the work of Aznar Cuadrado et al. (2005) the analysis of some supersonic downflows seen in the He ɪ lines was limited by the available spectral range of the TIP-I instrument.
The spectral window of TIP-II (10825-10836 Å) contains photospheric lines of Si ɪ at 10827.0877 Å, Ca ɪ at 10829.268 and 10833.382 Å and Na ɪ at 10834.85 Å, the chromospheric He ɪ multiplet and two telluric blends at 10832.1 Å and 10833.9 Å. For the TIP-I instrument the spectral window was limited to the first telluric line (see Fig. 4.8).

5.2 Observations

On 2005 May 18 we recorded with the TIP-II instrument, observations of the active region NOAA 10763, located at 24° W, 14° S on the solar disc, which corresponds to a cosine of the heliocentric angle $\mu = 0.9$. During the observations a flare of GOES class C2.0

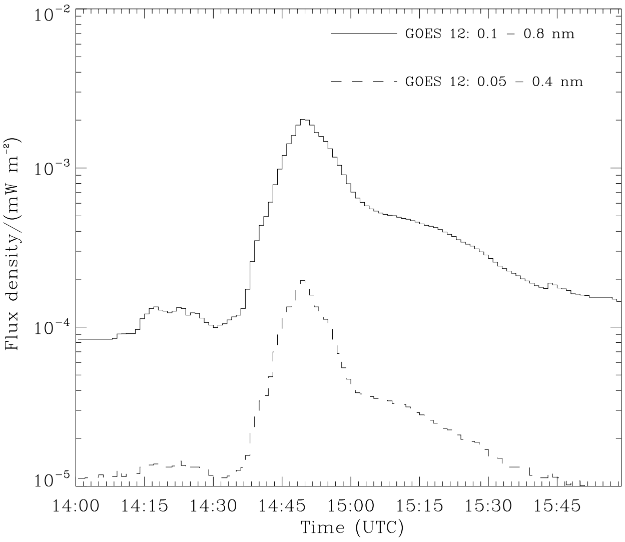

Figure 5.1: Soft X-ray full-disc flux in the 0.5-4 (dashed line) and 1-8 Å (solid line) bands, around the time of the flare, as provided by the GOES 12 data.

erupted in the west part of the active region. In Fig. 5.1 we show the soft X-ray flux in the 0.5-4 and 1-8 Å range provided by the GOES 12 satellite.

A filament was present in the active region and the observations follow the evolution of its magnetic structure occurring after the flare eruption. In Fig. 5.2, eight images obtained with the Hα slit-jaw camera at the VTT are presented. They illustrate the very rapid temporal evolution of the filament (darker structure) visible at the center of the images in between the two flare ribbons (bright structures) that are also clearly visible. The vertical line that we see in the images is the slit of the spectrometer while the two hairlines (horizontal lines) delimitate the field of view of the spectra. The black spot in the lower-right corner is an impurity on the mirror holding the spectrograph slit. It does not affect our observations since it is only visible in the slit-jaw images. The evolution of the filament was covered by scanning in steps of 0.35" perpendicular to the slit orientation, from 14:38:29 to 15:02:26 UT, providing a map of the region of 36.5×25 Mm^2. In the first image (upper left) we can see that when we started our scan a part of the filament material was already ejected southward after the flare eruption happened at 14:34. However, the filament does not show a global eruption and it was not associated with a coronal mass ejection.

Figure 5.3 (top) displays the magnetogram obtained with the Michelson Doppler Imager (MDI) instrument on-board of the Solar and Heliospheric Observatory (SOHO) spacecraft of the observed active region. The red box delimitates the part of the active region that was scanned with the TIP-II camera. In the bottom panel of Fig. 5.3, the observed Stokes-V map is displayed in the same system of coordinates. The map was obtained by integrating the Stokes-V parameter within a wavelength range of 0.2 Å in the left wing of the Si I line. The alignment is obtained from a cross–correlation of the two images. The cross–correlation was maximized by rotating, shifting and scaling the TIP image with respect to the MDI one. We can clearly distinguish two different main patches in the map with opposite magnetic field polarity. The filament was lying above the neutral line.

Figure 5.4 shows Stokes I maps of the observed region obtained in the continuum (top)

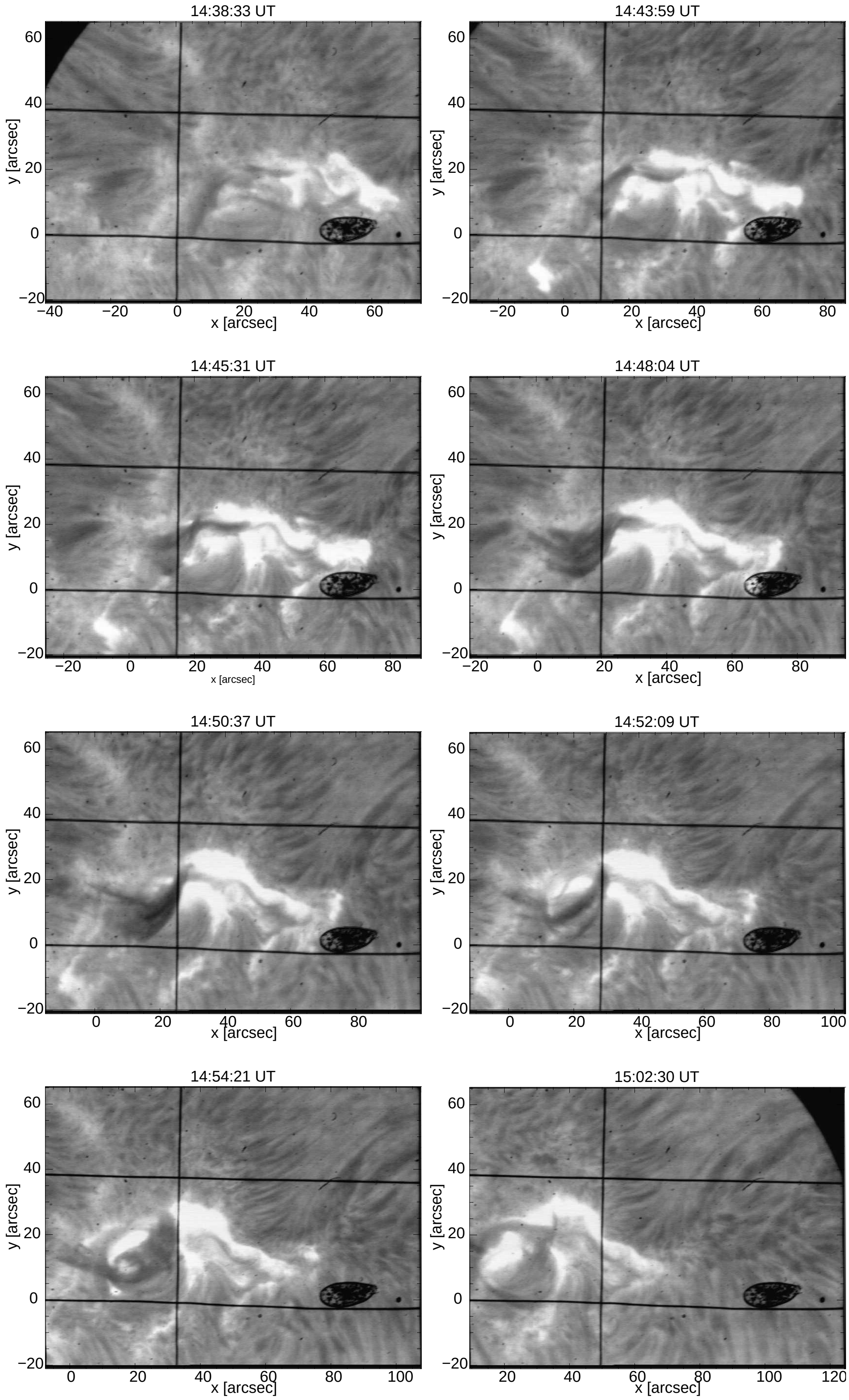
14:38:33 UT
14:43:59 UT
14:45:31 UT
14:48:04 UT
14:50:37 UT
14:52:09 UT
14:54:21 UT
15:02:30 UT
y [arcsec]
x [arcsec]
60
40
20
0
−20
−40
80
100
120

Figure 5.2: Hα images of the active region NOAA 10763 obtained with the slit-jaw camera at the VTT. We can follow the evolution of the filament from the beginning of the observation at 14:38:33 to the end of the scan at 15:02:30.

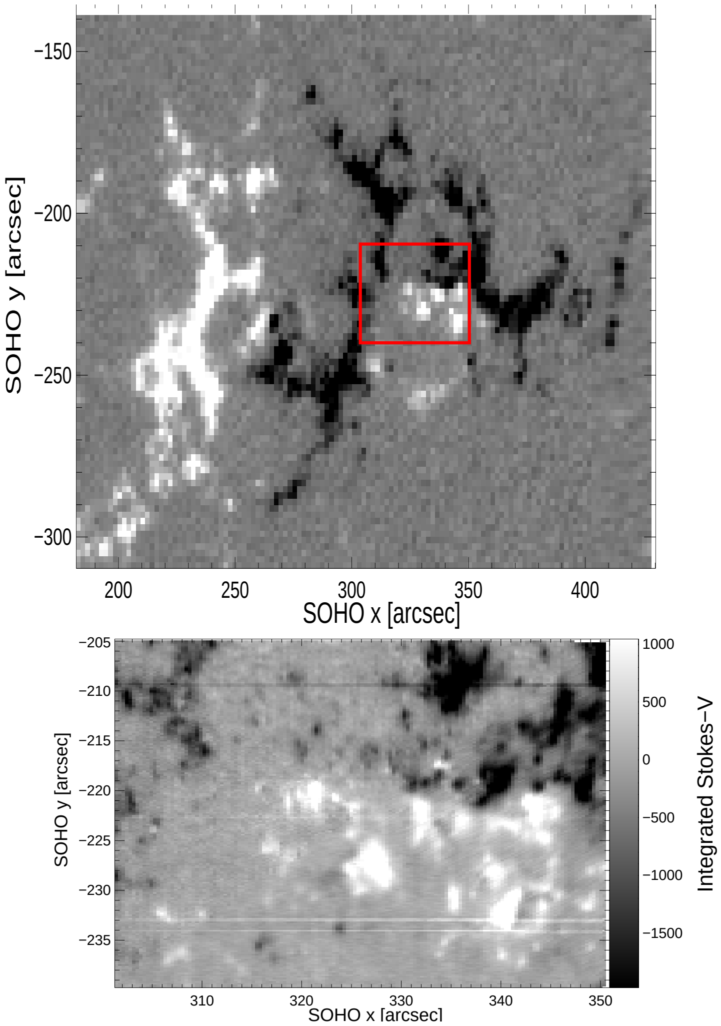

Figure 5.3: Top: Magnetogram of the active region NOAA 10673 obtained with the MDI instrument on board of SOHO spacecraft. Bottom: Stokes-*V* map of the part of the active region scanned with the TIP-II instrument. The two images are in the same coordinates. The frame in the upper image marks the field of view of the lower magnetogram.

and in the minimum of the ‘red’ component of the He I triplet (bottom). The slit is oriented along the y-axis and the direction of the scan is along the x-axis. Therefore, the information that we have from the scan along the x-axis is both spatial and temporal. In addition to a few small pores, the upper panel clearly shows the granulation across the whole image, suggesting that the seeing conditions during the scan were particularly good and stable, allowing on average a resolution of 1.2" to be reached. Note that the diffraction limited performance of the VTT at this wavelength will provide a resolution of 0.7". From the lower panel of Fig. 5.4 the presence of a strong absorption in the He I lines at 9” $< x <$ 33”, observed from ~ 14:43 to 14:53 UT, is clearly visible. The intensity map in the Hα line has been put together from vertical slices placed through the slit-jaw camera images just next to the slit (Fig. 5.5), so that the lower frame of Fig. 5.4 and Fig. 5.5 can be directly compared. A comparison between Figs. 5.4 and 5.5 clearly shows that the strong absorption seen in the He line comes from the filament material. Actually, the filament

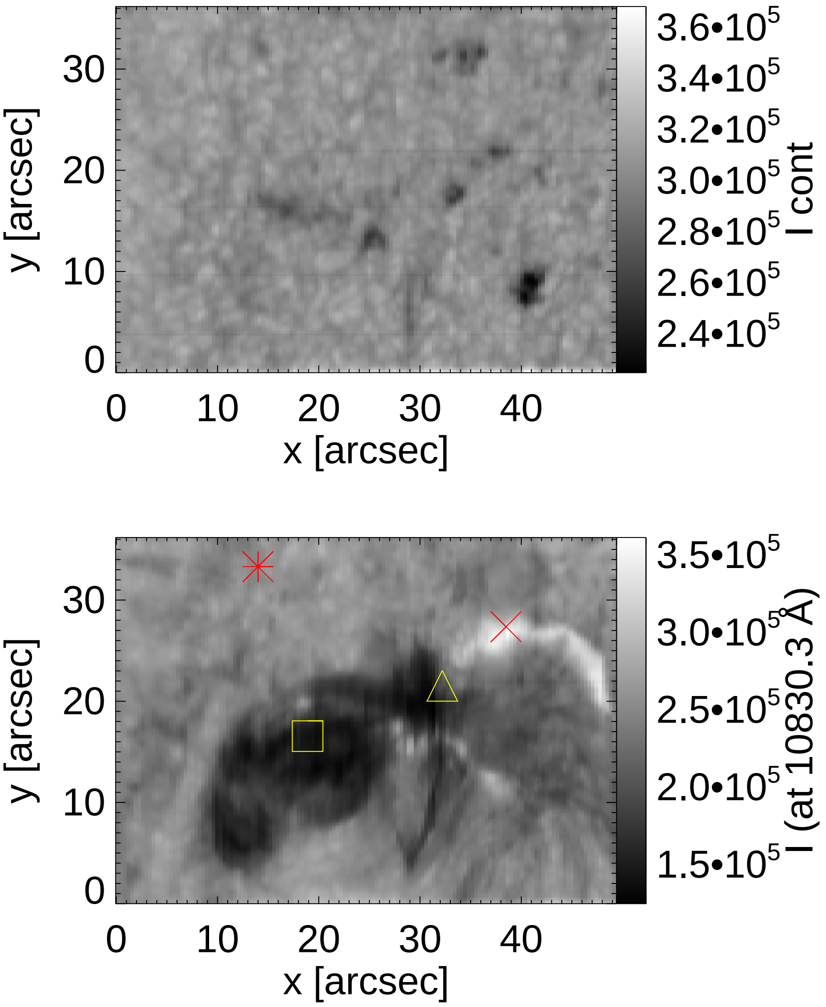

Figure 5.4: Intensity maps at different wavelengths of the scanned portion of active region NOAA 10763 (24° W, 14° S). Top: Continuum. Bottom: He I line minimum of the ‘red’ component. The different symbols refer to the line profiles shown in Fig. 5.6.

is larger and more prominent in the He 10830 than in Hα. However, this may have to do with the rather wide passband of the Hα slit-jaw filter. It is a Lyot filter with a full width at half maximum (FWHM) of 0.05 nm. The spectral resolution of the spectrograph is higher for the He 10830 wavelength region, the FWHM of the spectrograph is approximately 0.004 nm.

In the last part of the map (33” $< x <$ 49”), at $y \approx$ 19”-28", during the scan of a flare ribbon, the absorption in the He I lines is weaker than in quiet sun regions and the spectra also show emission profiles (visible as brightenings in the image). In this region the Hα slit-jaw images also display flare ribbons.

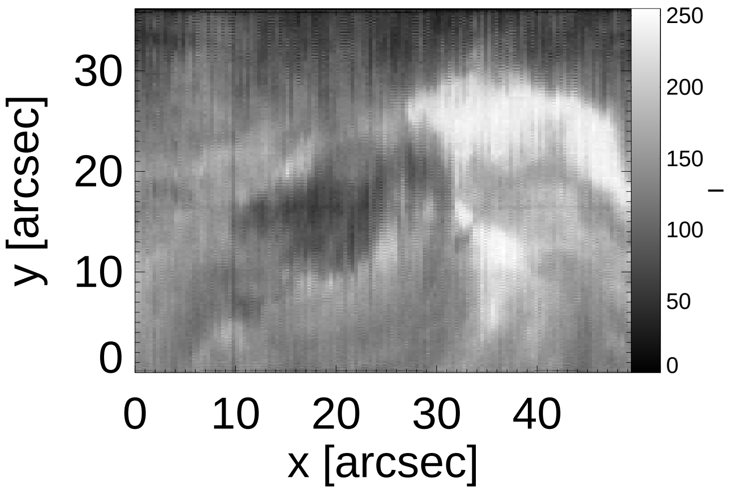

Figure 5.5: Intensity map of the scanned portion of active region NOAA 10763 obtained in the Hα line.

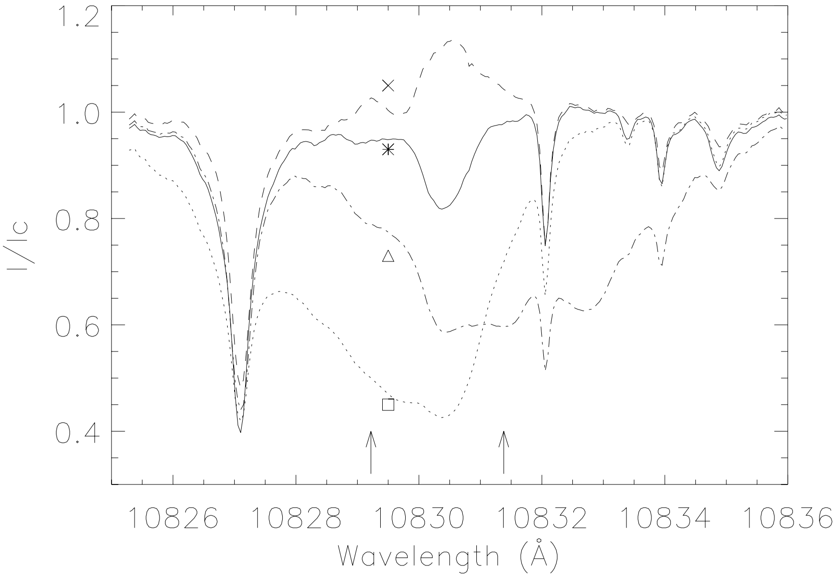

Figure 5.6: Observed Stokes *I* profiles at different locations, indicated by the different symbols in Fig. 5.4. Solid line: quiet sun profile. Dashed line: He ɪ emission profile. Dot-dashed line: very broad He ɪ profile indicating different redshifted atmospheric components. Dotted line: deep absorption in the He lines, partly strongly blueshifted.

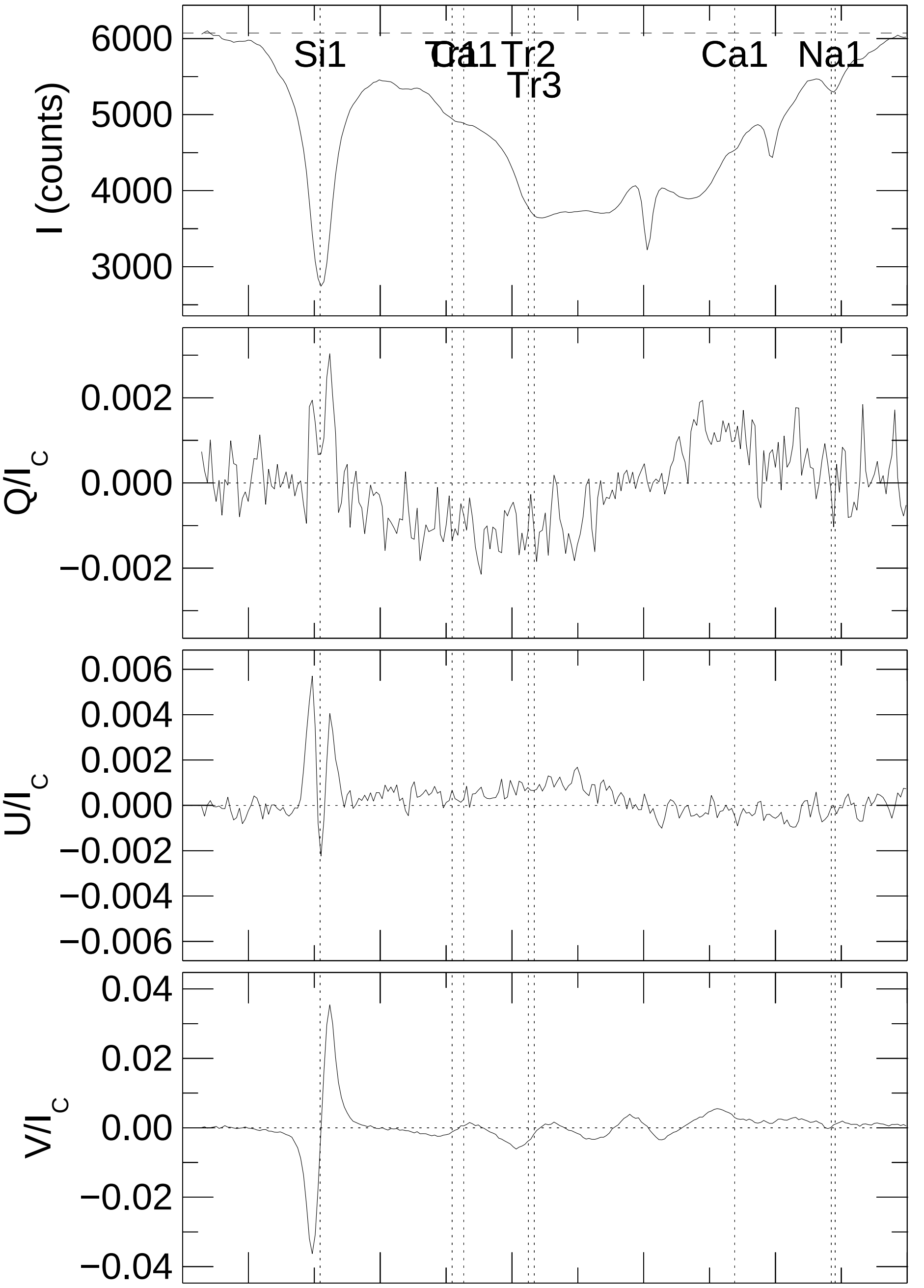

Figure 5.7: Example of an observed Stokes vector (dot-dashed profile of Fig. 5.6). The unusually broad Stokes *I* profile and the signatures of the *V* profile suggest the presence of different atmospheric components for the He I lines.

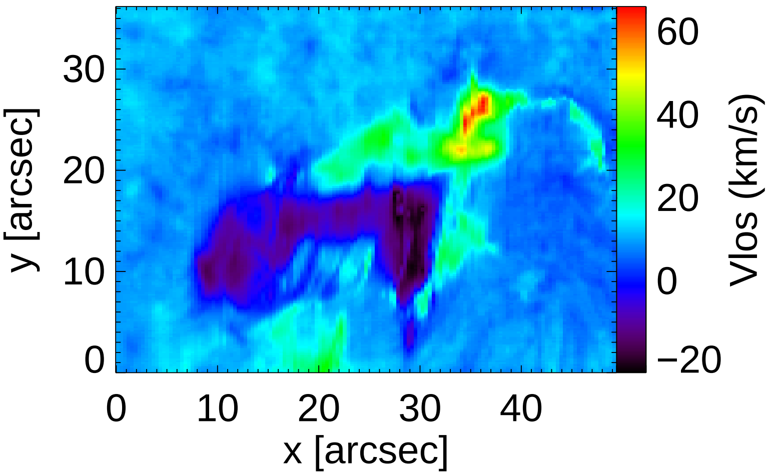

Figure 5.8: Wavelength center of gravity position of the absorption in the intensity profiles for the whole scan expressed in velocity dimensions (km/s).

5.3 Analysis of the Stokes profiles

The analysis of the Stokes profiles of the scan reveals huge differences in their shapes and behaviors. In Fig. 5.6 four observed Stokes I profiles normalized to the continuum intensity are plotted as an example of the unusually wide range of Stokes profiles observed. The spectra are binned over four spectral pixels and eight spatial pixels in order to increase the signal-to-noise level to $\sim$ 2000. In some spectra the signal-to-noise level is still not good enough to detect significant signal in the Q and U Stokes profiles but no larger bins are possible due to the relevant differences between profiles belonging to adjacent pixels. The solid line represents a profile observed in a comparatively quiet region of the map (at the location of the asterisk in the lower frame of Fig. 5.4), the dashed spectrum shows a He ɪ profile in emission observed in a flare ribbon (cross in Fig. 5.4), the dot-dashed (triangle) and the dotted (square) lines show a very broad and deep absorption, respectively, in the He ɪ lines observed in the filament. The absorption in the dot-dashed profile covers the wavelength range from 10829 Å to 10835 Å.

The Stokes I profiles exhibit multiple minima not corresponding with any line center position. This fact clearly indicates the presence of multiple atmospheric components for the He ɪ lines at different velocities within the resolution element. In the case of the dot-dashed profile these components are redshifted (see also Fig. 5.7). By contrast, the dotted profile shows the presence of upward propagating gas in the He ɪ lines. The blueshift is so large that it reaches even beyond the blue wing of the Si ɪ line at 10827.1 Å, which corresponds to $\sim$ 90 km/s.

In Fig 5.7 the full Stokes vector for the dot-dashed profile of Fig. 5.6 (pixel position x = 32” , y = 22” in Fig. 5.4) is displayed. Clearly, the maxima of Stokes I absorption correlate with a signature in Stokes V, indicating that the downflows are located in magnetized regions of the solar atmosphere. In Fig. 5.7 the wavelength positions at rest of the different lines present in the wavelength range are indicated by the vertical dotted lines.

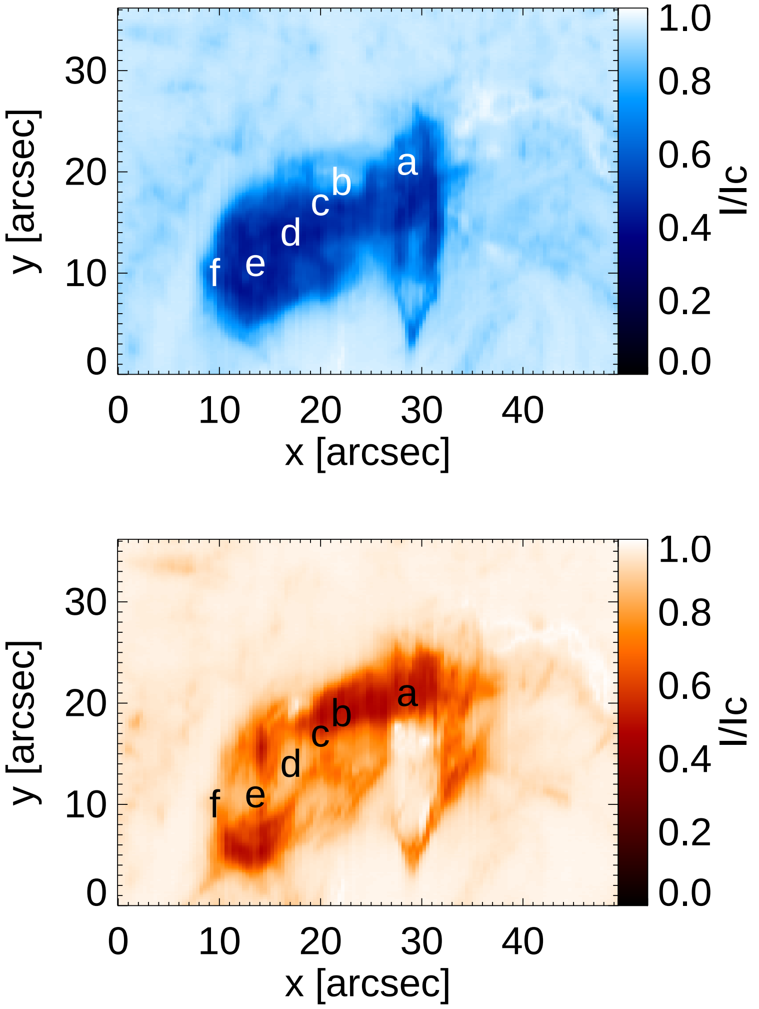

Figure 5.9: Intensity maps of the scanned active region obtained at different wavelength positions. Top: At -30 km/s with respect to the central position of the ‘red’ component of the He lines. Bottom: At +30 km/s with respect to the central positions of the ‘red’ component of the He lines. The different letters refer to the line profiles shown in Figs. 5.10 and 5.11.

5.4 Supersonic flows

In order to investigate how the multiple He components are related with the motion of the filament material we have plotted in Fig. 5.8 the wavelength center of gravity position of the absorption in the intensity profiles for the whole scan expressed in velocity dimensions (km/s). $v_{LOS} = 0$ corresponds to the He I profiles at rest. Positive values correspond to redshifted absorption and negative values to blueshifted absorption. Most of the filament displays a strong blueshift. A smaller area is covered by strong downflows. These downflows are concentrated mainly near the edge of the filament (upper right and to a smaller extent also lower left). Although this figure displays the topography of general up- and downflows, it must be interpreted with care, since it neglects the possibility of multiple velocity components indicated in Figs. 5.6 and 5.7.

In Fig. 5.9 we show two intensity maps of the scanned active region at wavelength positions -1.08 Å (upper panel) and $+1.08$ Å (lower panel) with respect to the central position of the 'red' component of the He lines. The wavelength locations are also marked by arrows in Fig. 5.6. These correspond to up- and downflows of 30 km/s, respectively. From these maps we can see that not only most of the profiles indicated by the strong absorptions present in Fig. 5.9 show either blue- or redshifted components, but also that there are profiles where blue- and redshifted components coexist within a resolution element. Upflows and downflows are present at the same spatial position. In Fig. 5.10 and 5.11 we present some examples of observed Stokes *I* and Stokes *V* profiles respectively at different pixel positions marked by the letters a-f in Fig. 5.9. All these profiles show the presence of different atmospheric components of the He I lines and in some of them, e.g., (c) and (e), blueshifted and redshifted components coexist. We have also evidence of different He components showing emission and absorption within the same profile, which are generally co-located with the bright Hα flare kernel.

5.5 Conclusions

From the analysis of the observed profiles discussed here, there is evidence of the presence of different unresolved atmospheric components of the He lines, coexisting within the same pixel. Multiple unresolved magnetic components (Lagg et al. 2004) are found not only in a filament. In our case, they are more common and show supersonic upflows and downflows, sometimes within the same resolution element. In the next chapter further analysis will be performed in order to determine the magnetic topology of the supersonic flows and the filament. A fitting technique based on a Milne-Eddington type inversions described in Chap. 3 will be applied. This study will help also to answer the question whether the up and downflows originate from different flux tubes.

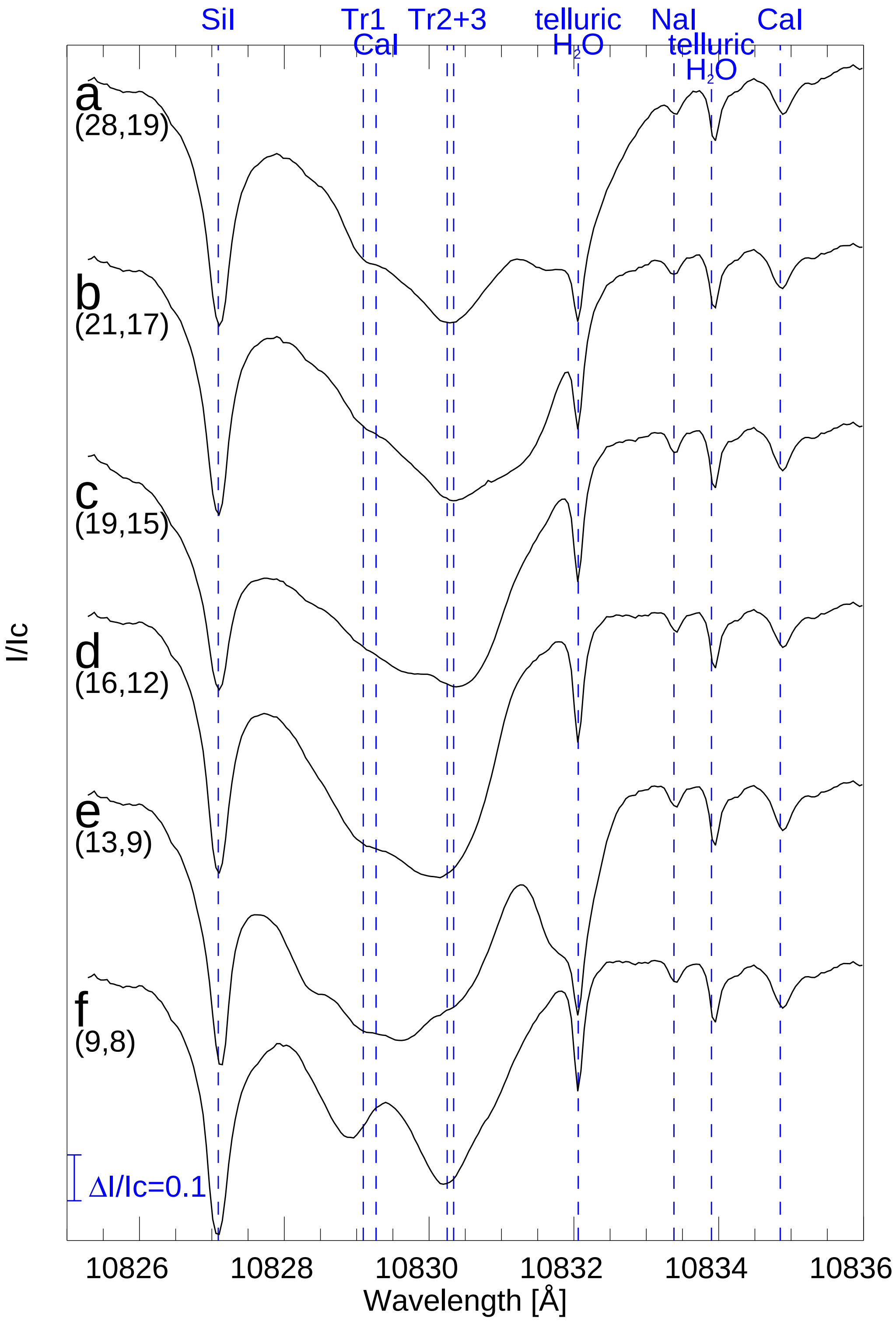

Figure 5.10: Observed Stokes *I* profiles, at the locations marked by letters in Fig. 5.9. The dashed, vertical lines mark the central position of the spectral lines present in the wavelength field of view of the TIP-II instrument. The (x,y) coordinates in arcseconds are written next to each profile.

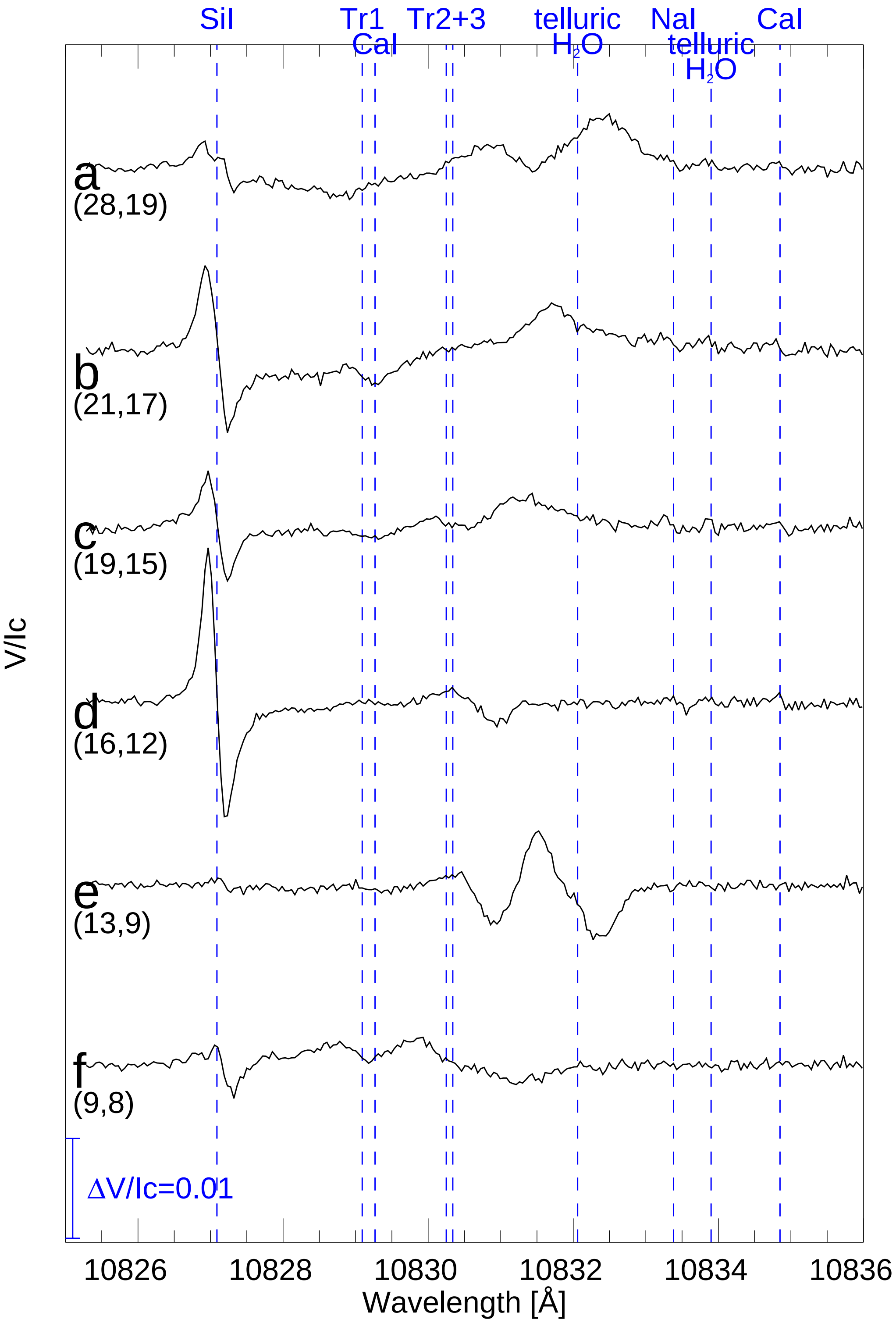

Figure 5.11: Same as Fig. 5.10, but now showing the observed Stokes *V* profiles, at different locations of Fig. 5.9.

6 Analysis and Results

In this chapter we analyze the spectropolarimetric observations, shown in the previous chapter, by using the inversion procedure as described in Sect 3.7.1. We retrieved the values of the atmospheric parameters like the magnetic field vector and the LOS-velocity for each profile we have observed. Maps of the retrieved atmospheric parameters will be interpreted to give a picture of the magnetic structure of the observed filament during the activity phase.

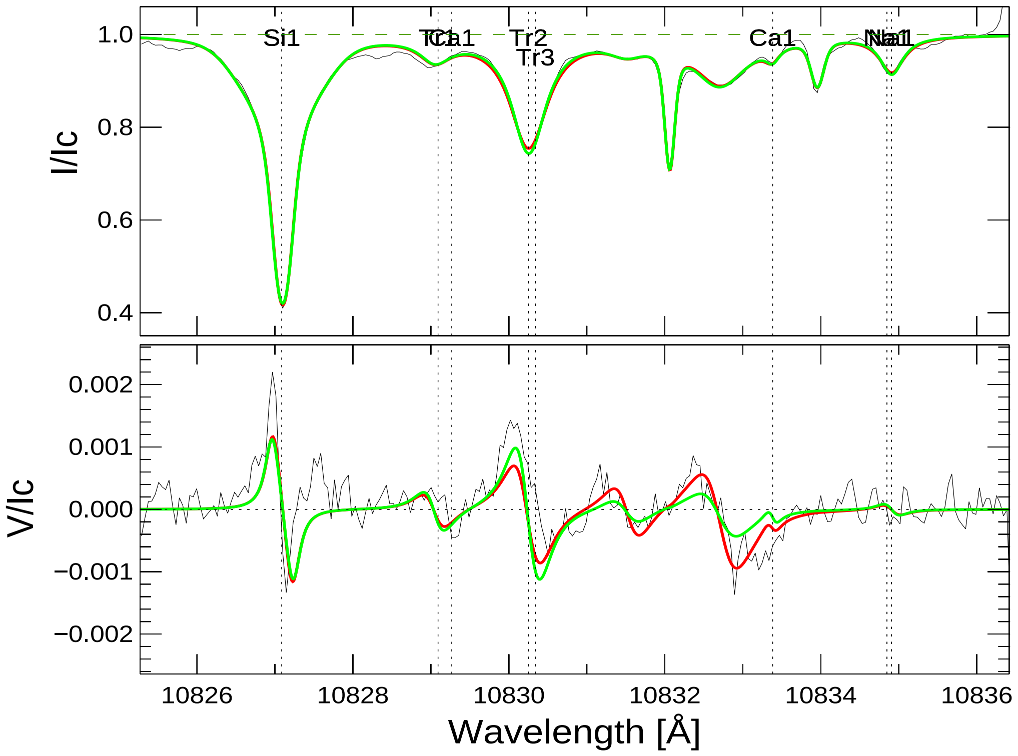

Figure 6.1: Inversions of the Stokes *I* and *V* profiles at the location (20",3") of the map in Fig. 5.4. The fits (red and green lines) to the observed profiles (black lines) are obtained by allowing two different atmospheric components to describe the He I lines. The fits are obtained by coupling the magnetic field vector between the two He components (green line) or leaving it free (red line).

Parameter	Green line fit Component 1/2	Red line fit Component 1	Component 2
B (G)	128.42	275.60	325.15
γ (°)	78.73	85.75	79.90
χ (°)	-25.91	-42.91	-55.53
v_{LOS} (km/s)	-1.29/66.86	-1.29	67.15
α	0.68/0.38	0.85	0.14

Table 6.1: Parameters returned for the He line by the two components fits displayed in Fig. 6.1.

fitness f=1.79

Parameter	Component 1
B (G)	83.18
γ (°)	129.03
χ (°)	2.25
v_{LOS} (km/s)	3.09
α	1.0

Table 6.2: Parameters returned for the He line by the one component fit displayed in Fig. 6.2.

fitness f=1.61

Parameter	Component 1	Component 2
B (G)	53.16	165.50
γ (°)	51.88	64.76
χ (°)	-31.16	-48.35
v_{LOS} (km/s)	-54.44	1.25
α	0.32	0.68

Table 6.3: Parameters returned for the He line by the two components fit displayed in Fig. 6.3.

fitness f=2.13

Parameter	Component 1	Component 2	Component 3
B (G)	95.01	331.80	295.64
γ (°)	80.14	107.37	70.11
χ (°)	-10.87	-71.36	25.10
v_{LOS} (km/s)	-53.98	-28.77	1.78
α	0.37	0.17	0.46

Table 6.4: Parameters returned for the He line by the three components fit displayed in Fig. 6.4.

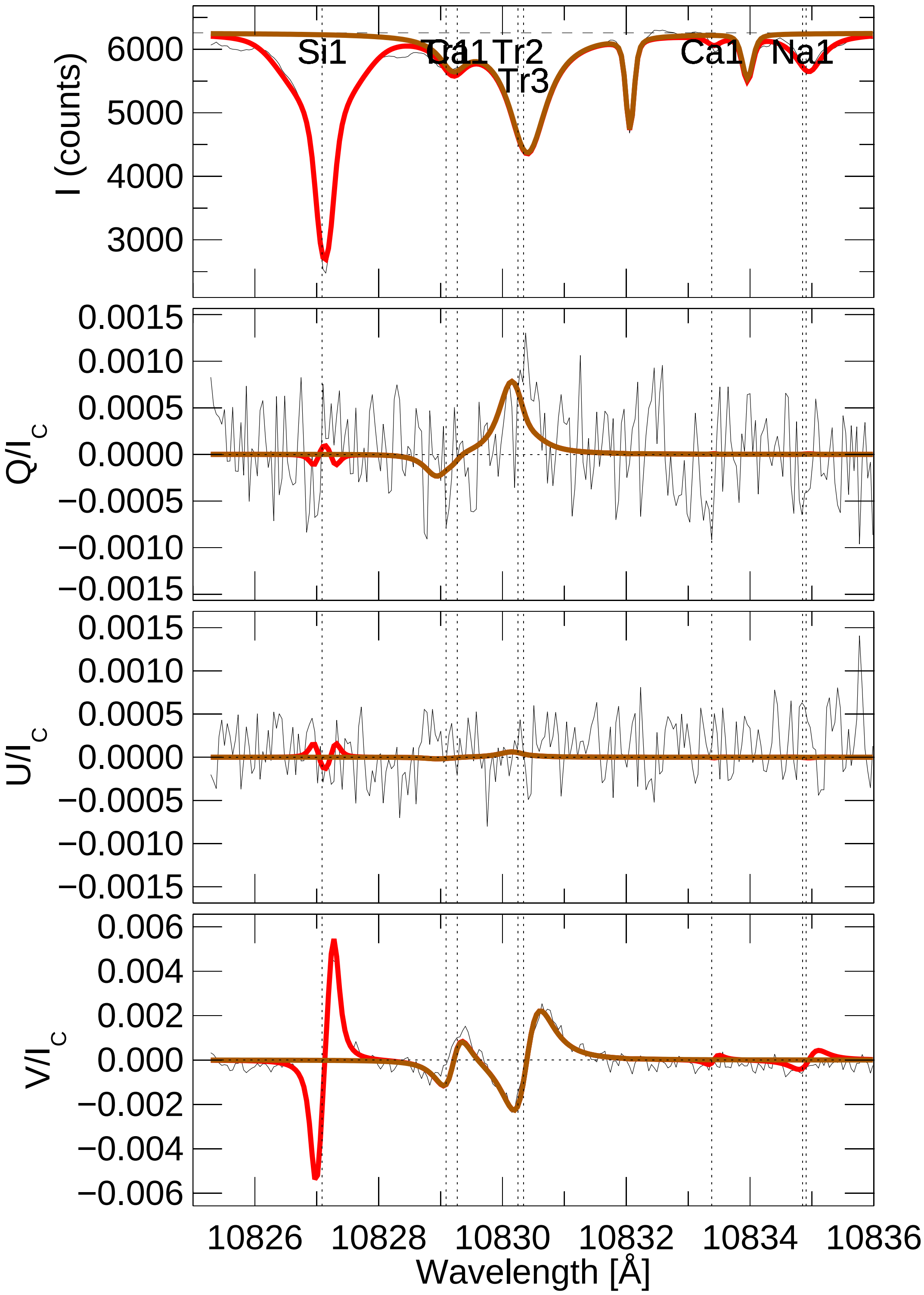

Figure 6.2: Inversions of the Stokes *I*, *Q*, *U* and *V* profiles at the location (5",13") of the map in Fig. 5.4. The black lines are the observed profiles while the red lines are the fits to all the observed lines obtained imposing one atmospheric component to describe the He I lines (brown line), and two for the photospheric lines.

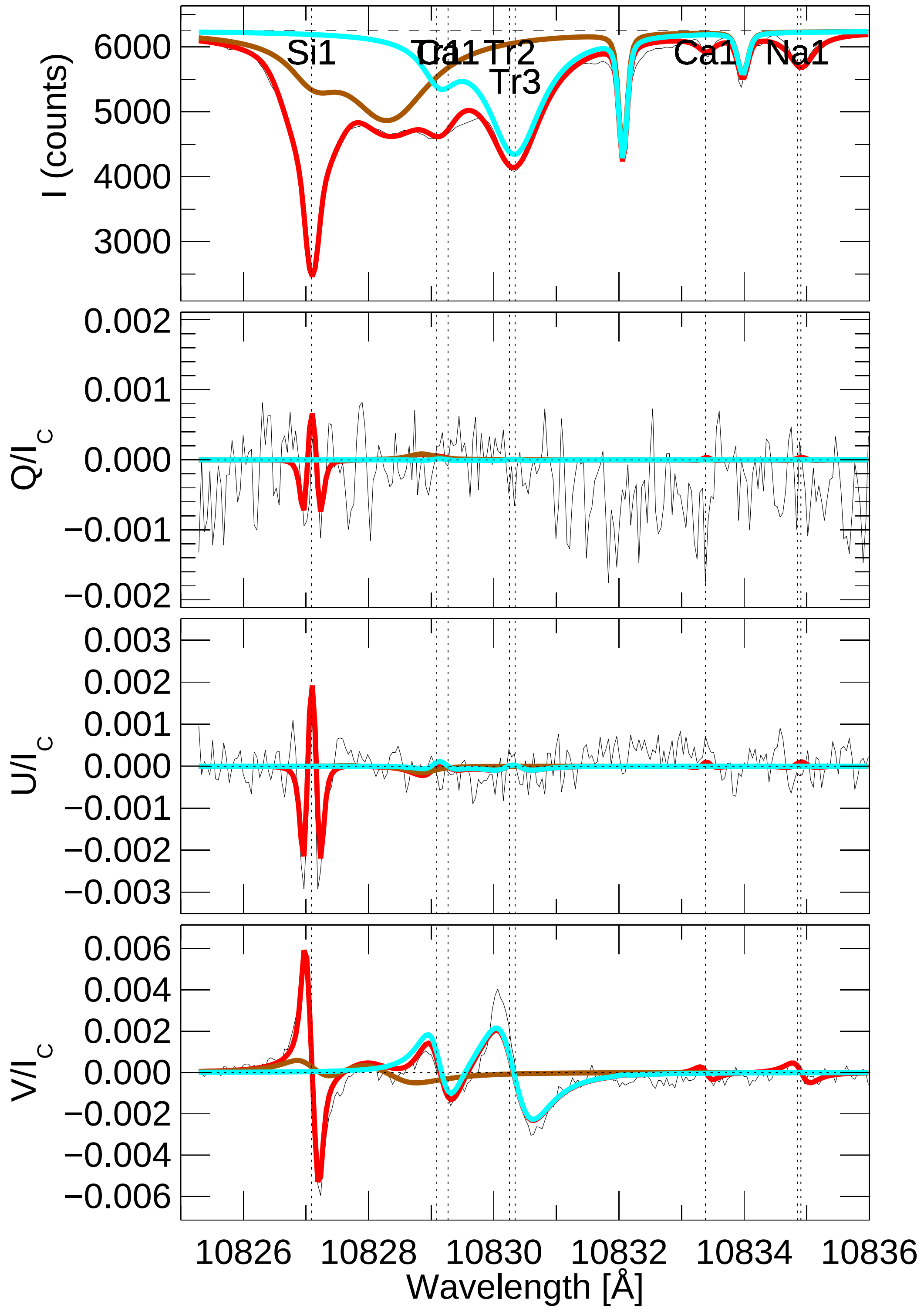

Figure 6.3: Inversions of the Stokes *I*, *Q*, *U* and *V* profiles at the location (27",9") of the map in Fig. 5.4. The black lines are the observed profiles while the red lines are the fits obtained imposing two different atmospheric components to describe the He I lines (brown and light blue lines).

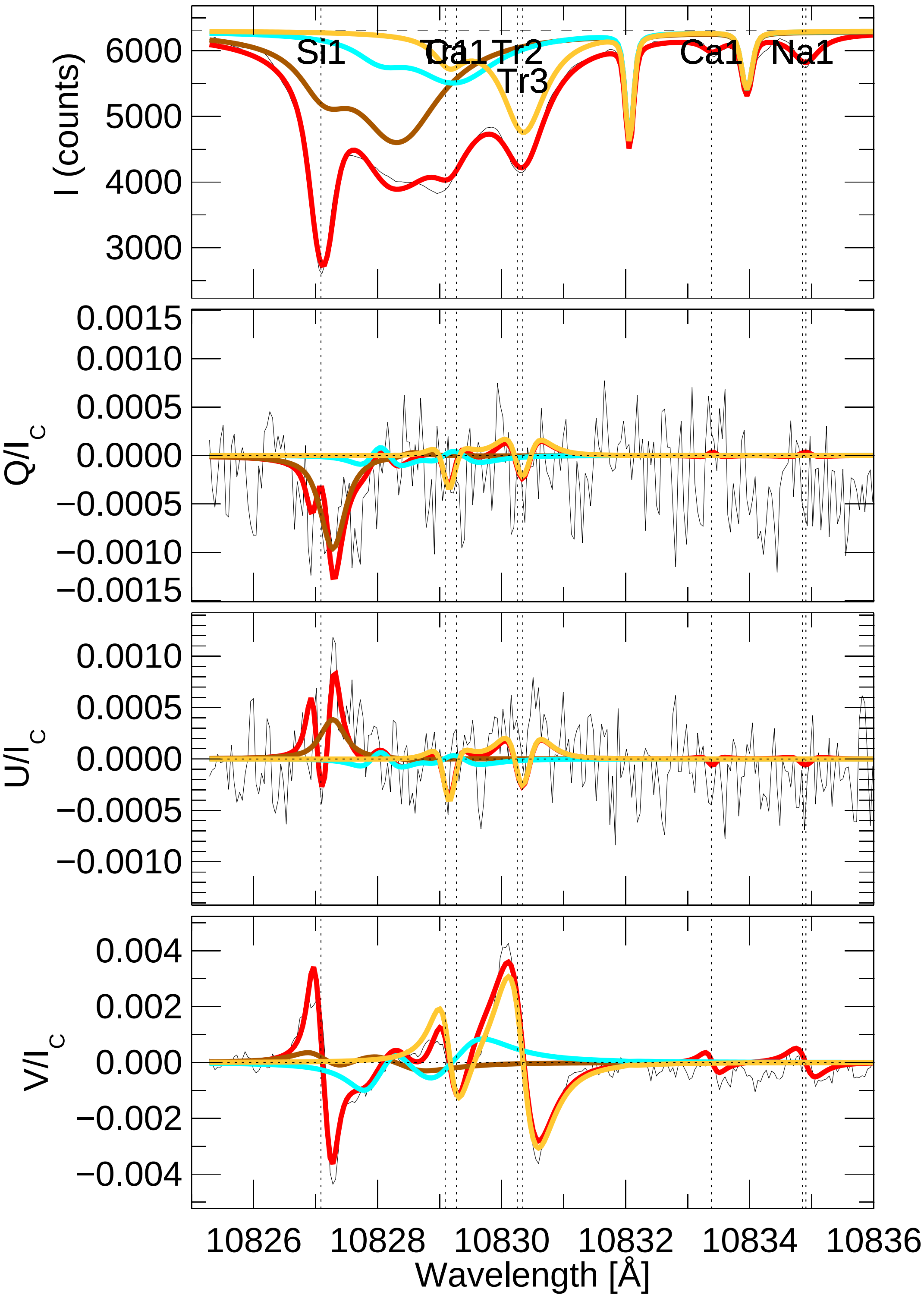

Figure 6.4: Inversions of the Stokes *I*, *Q*, *U* and *V* profiles at the location (29",14") of the map in Fig. 5.4. The black lines are the observed profiles while the red lines are the fits obtained by allowing three different atmospheric components to describe the He I lines (brown, light blue and yellow lines).

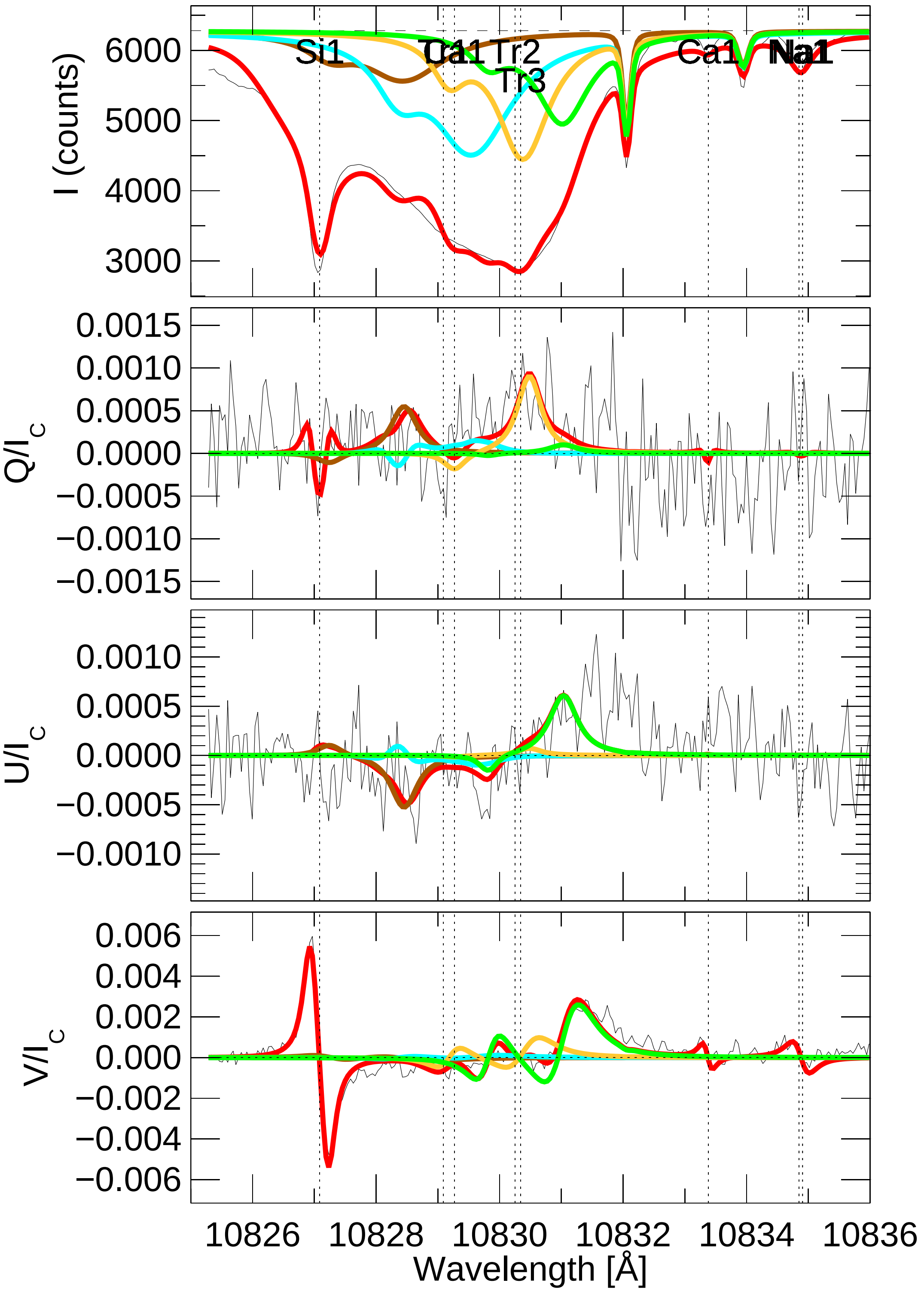

Figure 6.5: Inversions of the Stokes *I*, *Q*, *U* and *V* profiles at the location (18",20") of the map in Fig. 5.4. The black lines are the observed profiles while the red lines are the fits obtained by allowing four different atmospheric components to describe the He I lines (brown, light blue, yellow and green lines).

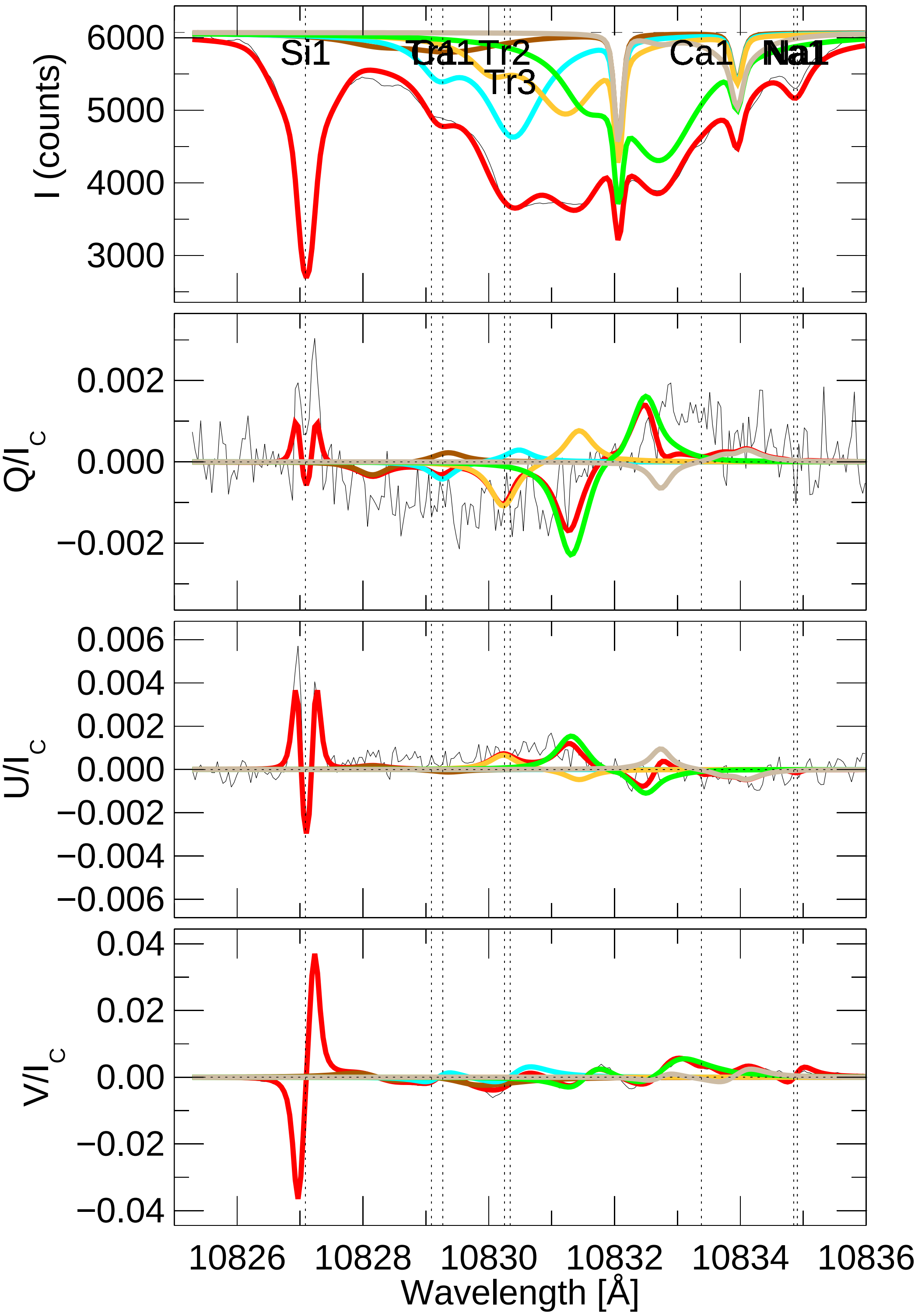

Figure 6.6: Inversions of the Stokes *I*, *Q*, *U* and *V* profiles at the location (32",22") of the map in Fig. 5.4. The black lines are the observed profiles while the red lines are the fits obtained by allowing five different atmospheric components to describe the He I lines (brown, light blue, yellow, green and dark grey lines).

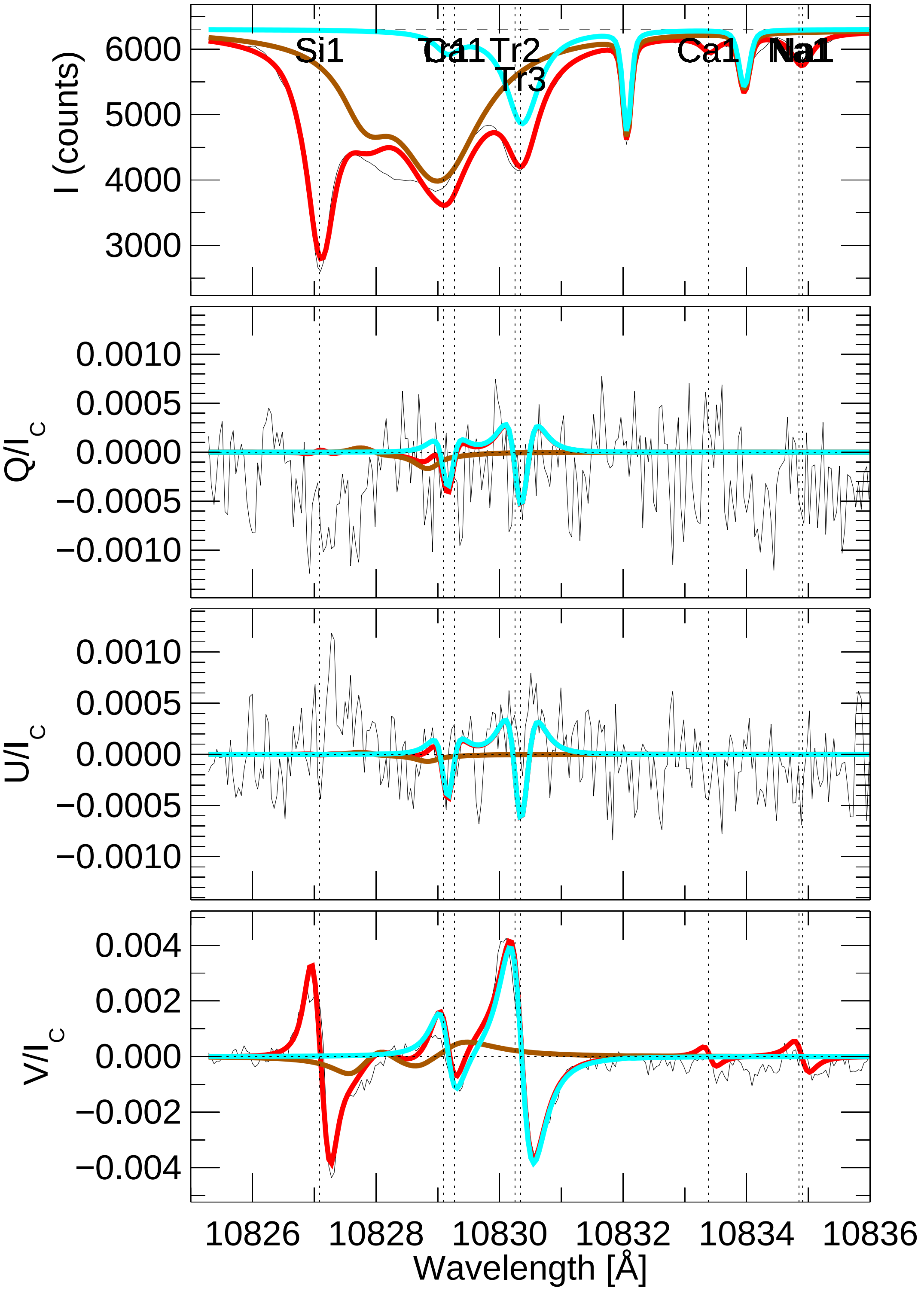

Figure 6.7: Inversions of the same profiles of Fig. 6.4. The fits (red lines) to the observed profiles (black lines) are obtained by allowing two different atmospheric components to describe the He I lines (brown and light blue lines), one component less than in the case of Fig. 6.4. The fitness function f (see Sect.3.7.1) is 1.53.

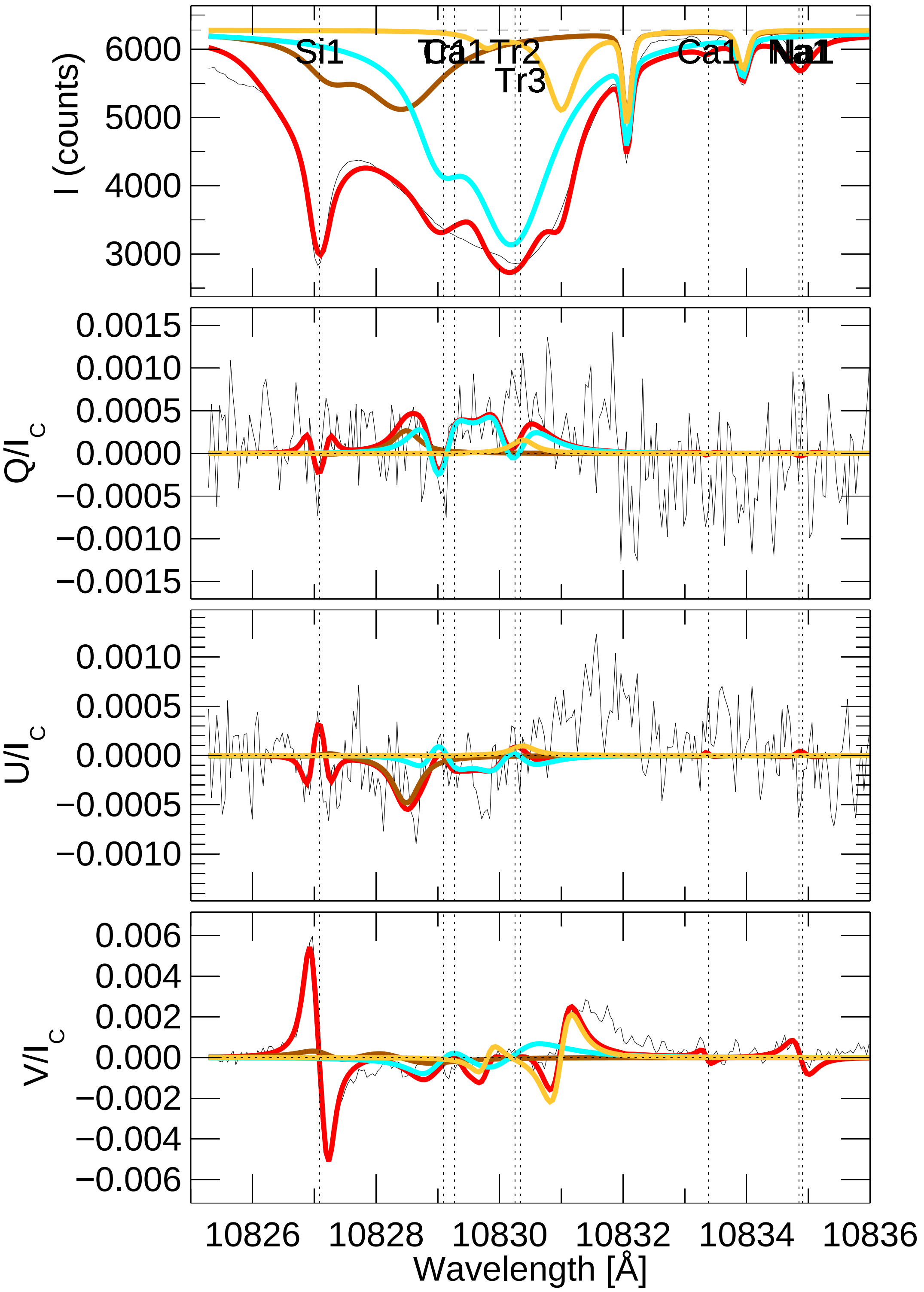

Figure 6.8: Inversions of the same profiles of Fig. 6.5. The fits (red lines) to the observed profiles (black lines) are obtained by allowing three different atmospheric components to describe the He I lines (brown, light blue and yellow lines), one component less than in the case of Fig. 6.5. The fitness function f is 1.63.

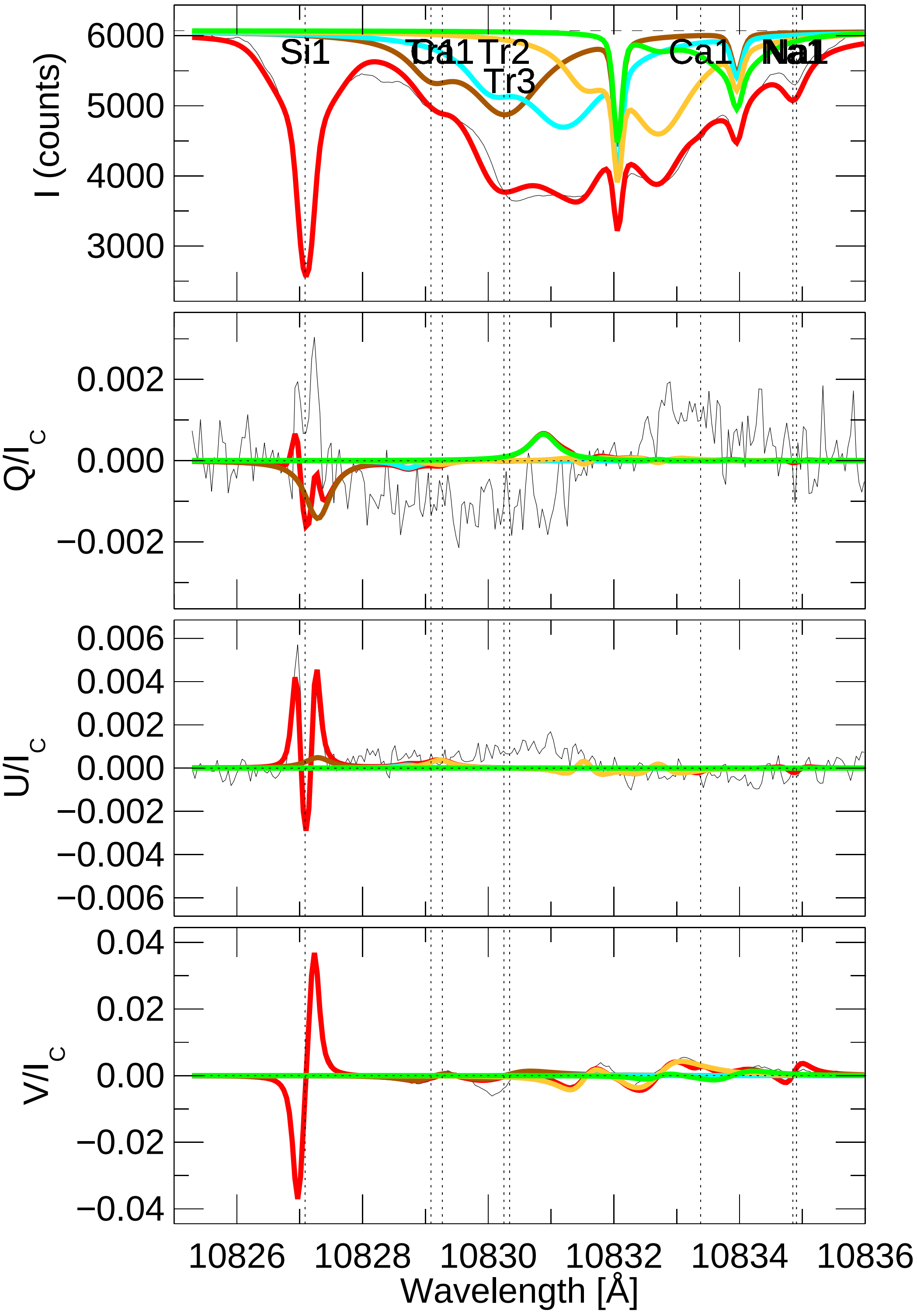

Figure 6.9: Inversions of the same profiles of Fig. 6.6. The fits (red lines) to the observed profiles (black lines) are obtained by allowing four different atmospheric components to describe the He I lines (brown, light blue, yellow, and green lines), one component less than in the case of Fig. 6.6. The fitness function f is 1.29.

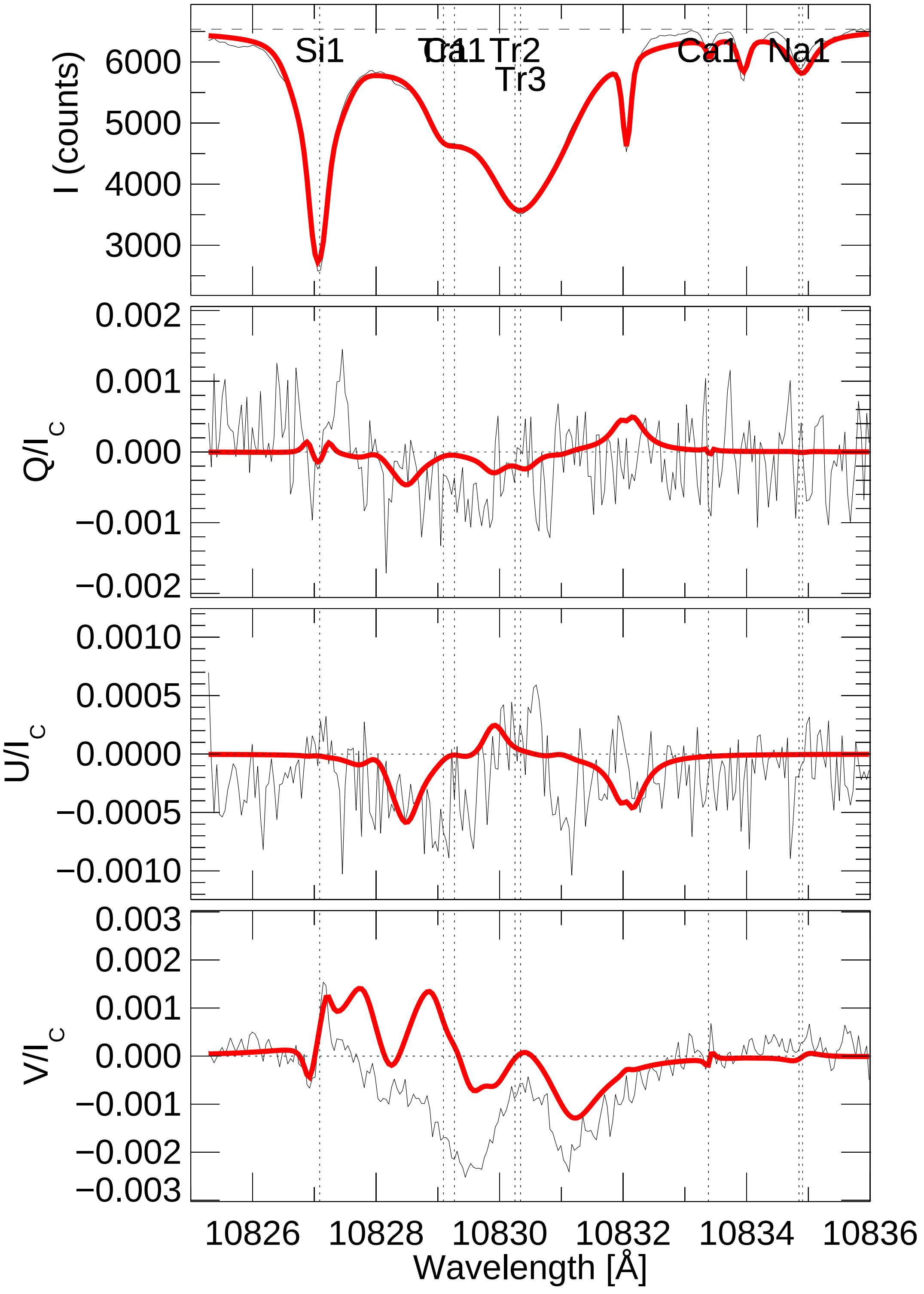

Figure 6.10: Inversions of the Stokes *I*, *Q*, *U* and *V* profiles at the location (12",18") of the map in Fig. 5.4. The black lines are the observed profiles while the red lines are the best fits.

fitness f=1.88

Parameter	Component 1	Component 2	Component 3	Component 4
B (G)	14.32	203.80	37.34	113.14
γ (°)	2.79	91.06	129.34	132.01
χ (°)	-21.87	-16.45	2.30	40.37
v_{LOS} (km/s)	-50.74	-20.11	-2.57	20.19
α	0.11	0.28	0.34	0.26

Table 6.5: Parameters returned for the He line by the four components fit displayed in Fig. 6.5.

fitness f=1.68

Parameter	Component 1	Component 2	Component 3	Component 4	Component 5
B (G)	613.10	111.48	1.24	291.58	501.02
γ (°)	7.58	151.62	150.22	127.72	118.79
χ (°)	-13.85	-0.21	-15.65	-17.01	-27.94
v_{LOS} (km/s)	-24.17	-3.00	26.12	67.43	100.92
α	0.05	0.30	0.22	0.32	0.11

Table 6.6: Parameters returned for the He line by the five components fit displayed in Fig. 6.6.

6.1 Fit to the observations

In the previous chapter, the variety of spectropolarimetric He 10830 profiles observed at positions corresponding to the presence of filament material in the Hα images has been introduced. The profiles are very complicated and clearly exhibit multiple He line components coexisting in one resolution element. The number of such components varies from one location to the next. We are interested in retrieving information on the full magnetic vector, the line-of-sight velocity and other physical quantities in the filament by inverting the observed Stokes profiles. The HELIX inversion code, presented in Sect. 3.7.1, allows the observed profiles to be fitted using a multi-components input atmosphere.

Since the number of He components observed per pixel changes during the scan that follows the evolution of the filament, we could not use a unique input atmosphere to invert all the profiles, but we had to differentiate between the input atmospheres, depending on the number of necessary He components. The different atmospheric components of the He line are mixed via a parameter, the filling factor α, that defines the contribution of the single atmospheric component to the total observed He profile. The sum of the filling factors of all atmospheric components within a resolution element is required to be unity. The maximum number of He atmospheric components we need is five. We have tested that we do not employ more components than necessary by first fitting each profile with a smaller number of free parameters. Only a significantly improvement of the fitness function f (defined in Sect. 3.7.1) warrants the use of more parameters. Usually, an insufficient number of free parameters results in parts of the observed line profile being poorly fit. For some extreme profiles we face the problem of a very large number of free parameters to be fitted. The spectral region covered by the He absorption signature also contains four photospheric lines and two telluric blends. Therefore, we also have to fit the four photospheric spectral lines, increasing the total number of components. To fit the strong photospheric Si ɪ line at 10827.0877 Å, we had to consider two atmospheric components: a magnetic component to fit the core of the line and a non-magnetic stray-light component for the wings. The two telluric blends result in eight additional free parameters, originating from fitting two Voigt profiles to the telluric lines.

The high number of free parameters can compromise the goodness of the fit to the observed profiles, because there are more possibilities for the code to arrange their values to get a good fit to the observations. This could result in the presence of multiple minima in the parameter space and the code would require an infinite number of iterations to find the global minimum. In this case, the stability of the code is affected and subsequent runs can result in a similar fit to the profiles but different retrieved values of the atmospheric parameters. To face this problem we must decrease the number of free parameters. This was achieved by coupling some atmospheric parameters between the atmospheric components meaning that a given atmospheric parameter was forced to have the same (but not prescribed) value in all atmospheric components, or that all lines from the same atmospheric layer (in particular the photosphere) must be formed in the same atmosphere. We also narrowed the ranges for some other parameters, which also helps to ensure the uniqueness of the solution. In particular, we coupled the magnetic field vector (B, γ and χ) and the gradient of the source function S_1 between the four photospheric lines, assuming that their values stay approximatively constant in the photosphere. This is consistent with the assumption that the four lines are formed at similar heights and can be represented by a single atmosphere. Among the photospheric lines, the Si ɪ line is the strongest one and shows clear signatures in the Stokes profiles (best signal-to-noise). Changes in the atmospheric parameters will have a larger influence on the Stokes profiles of the Si line than of the weaker photospheric lines. Therefore, the photospheric parameters are mainly determined by the shapes of the Si profiles. Then, we made an inversion run for the whole map, fitting only the photospheric and the telluric lines. From the results of the fit, assuming that the lines are not disturbed by the filament activity happening at higher atmospheric layers, we could select a narrower input range for the Doppler width $\Delta\lambda_D$ of the photospheric lines and the width and the damping of the Voigt profile for the telluric blends. The narrower input ranges are then used for the inversion done including also the He lines. This avoids that the code broadens and shifts these lines by large amounts to mimic a further He component.

For the different He components, we chose not to couple the magnetic field vector. The choice of leaving the magnetic field vector free for the He components allows the possibility for the filament material to belong to different magnetic field lines (observed contemporarily in one pixel element resolution). Test runs showed, that a coupling of the magnetic field vector between the individual components resulted in worse fits, i.e. the fitness function, f, was lower. In Fig. 6.1 we show the result of inversions of the observed I and V profiles (black lines) at the location (20",3") of the map in Fig. 5.4. The fits (green and red lines) are obtained, in both the cases, by allowing two different atmospheric components to describe the He I lines. The green line represents a fit obtained by coupling the magnetic field vector between the He components while for the fit represented by the red line we allowed the magnetic field vector to be free. The retrieved values of the atmospheric parameters are listed in Table 6.1. The green line fit shows that coupling the magnetic field vector between the two He components, we are not able to reproduce the

Stokes V profile of the component with the smaller filling factor. We need to leave the magnetic field vector free to obtain a better fit to the observed profiles. The average values of the fitness function f obtained on 100 inversion runs of this same profile are 2.43 for the red line fit and 2.26 for the green line fit.

We coupled the gradient of the source function S_1 between the He atmospheric components and from the visual analysis of the observed profiles we could also assign a very narrow input range for v_{LOS} of each He component. In fact, when the velocity separation between the He profiles is large enough ($\sim$ 10 km/s) we can clearly distinguish the positions of the different minima in the I profile.

There are profiles in the scan in which the He lines show emission features. These profiles were excluded from further analysis. Even if the HELIX code can fit emission profiles by setting the gradient of the source function S_1 to a negative number, the analysis technique is not optimized to produce reliable results. Moreover, in some profiles the He emission profiles coexist with blue- or redshifted He absorption profiles, making the retrieval even more complicated. In the maps we are going to show in the next section, the pixels containing profiles that were not inverted will be black.

Examples of the inversions of increasingly complex He Stokes I, Q, U and V profiles are shown in Figs. 6.2– 6.6. In each plot, the black lines are the observed profiles while the red lines are the best fits to the observations obtained considering, as input to the inversion code, one, two, three, four and five atmospheric components of the He I lines, respectively. The plots show also the different He components (brown, light blue, yellow, green and dark grey lines) whose sum gives the red lines. In Tables 6.2–6.6 we give the values of the atmospheric parameters B, γ, χ, v_{LOS} and α returned for each component of the He line by the multiple-components fits displayed in Fig. 6.2–6.6, respectively. For each fit we also give the value of the fitness function, f.

The fits reproduce the observed Stokes vector reasonably well in almost the entire map. We already pointed out in the beginning of the chapter that tests have been done to be sure that we are using the right number of components and that it is not possible to get equally good fits with fewer free parameters. Figs. 6.7–6.9 give examples of fits to the observed profiles already displayed in Figs. 6.4–6.6, obtained by allowing one less He component to reproduce the observed profiles with respect to the corresponding previous fits. The values of the fitness function f, written in the caption of each figure, are always smaller than the one obtained for the correspondent fit with one more component. We see that an insufficient number of components results in a poor fit of the observed line profiles.

There are some pixels concentrated in a region of the map (approximately at 11” $< x <$ 17” and 17” $< y <$ 19”) for which we could not get satisfactory fits due to a very strong negative signature in the Stokes V profile that the code is not able to reproduce. In Fig. 6.10 an example of such a profile is given. Again, the black lines are the observed profiles while the red lines are the best fits. These profiles are likely to be contaminated by crosstalk from I to V, which the data reduction routines were not able to remove. We also exclude these profiles from further analysis. The Stokes I profile can indeed be well reproduced (in this example we are considering four He components as input).

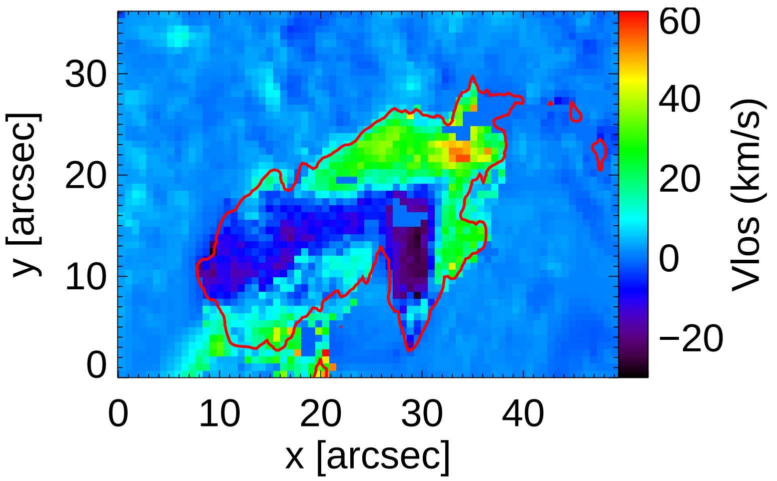

Figure 6.11: Map of the mean value of the retrieved v_{LOS} for the He components weighted with the respective filling factor α. The red contour outlines the position of the filament, $I_c - I = 2 \times 10^4$ counts in Fig. 6.12.

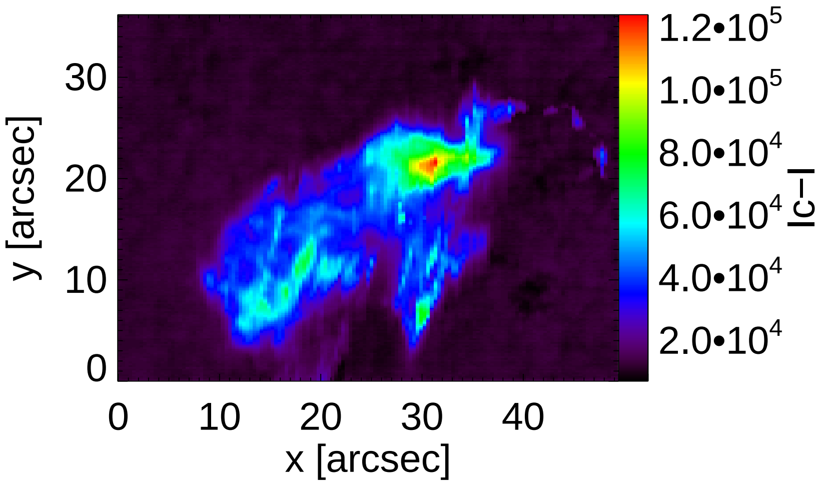

Figure 6.12: Intensity map obtained by integrating $I_c - I$ over the wavelength covered by the He absorption (10828-10835.7 Å). The intensity contribution due to the other spectral lines has been subtracted.

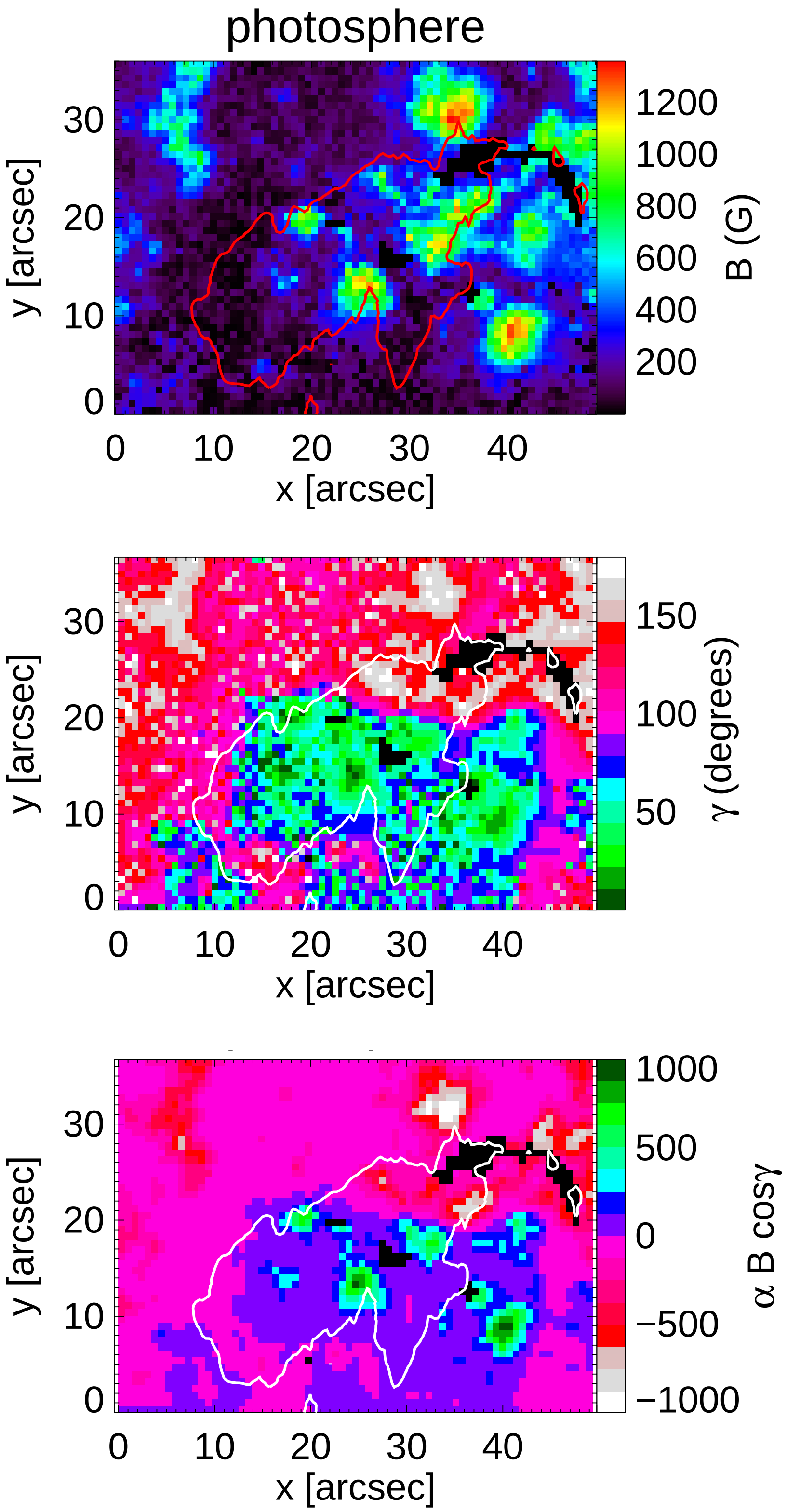

Figure 6.13: Upper panel: Map of the photospheric magnetic field strength determined from the photospheric lines. Middle panel: Map of the photospheric magnetic field inclination with respect to LOS. Lower panel: Map of the LOS magnetic field component averaged over magnetic and stray light contribution. Red and white contours outline the border of the filament.

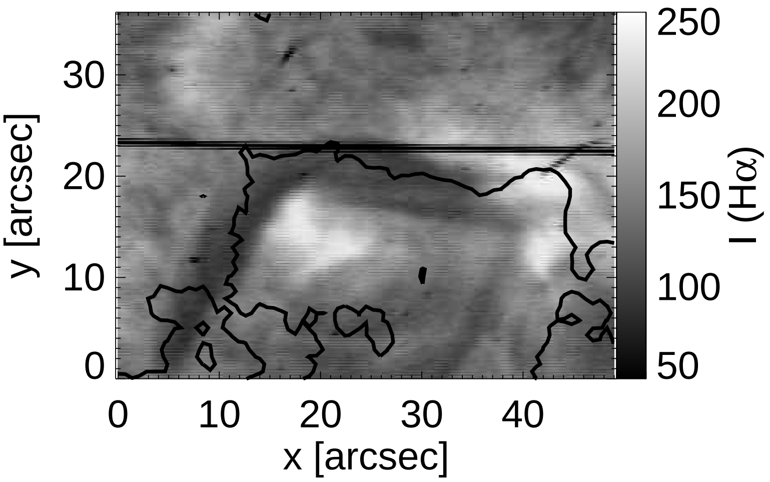

Figure 6.14: Hα image obtained with the slit-jaw camera at the VTT at 14:22:33 UT. The contour line indicates the position of the inversion line of the magnetic field in the photosphere, i.e. where $\gamma = 90°$.

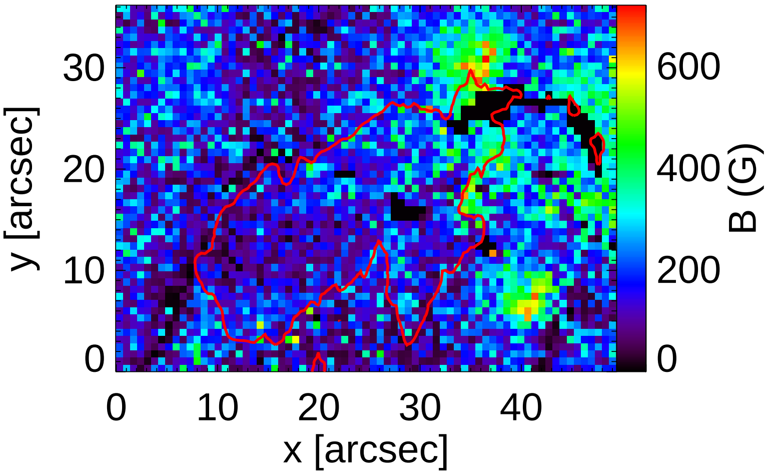

Figure 6.15: Map of the chromospheric magnetic field strength. The magnetic field strength values are the result of a weighted mean of the strengths of the individual components reproducing the measured Stokes profiles of the He ɪ 10830 Å. The weights are the filling factors of the relative He atmospheric components.

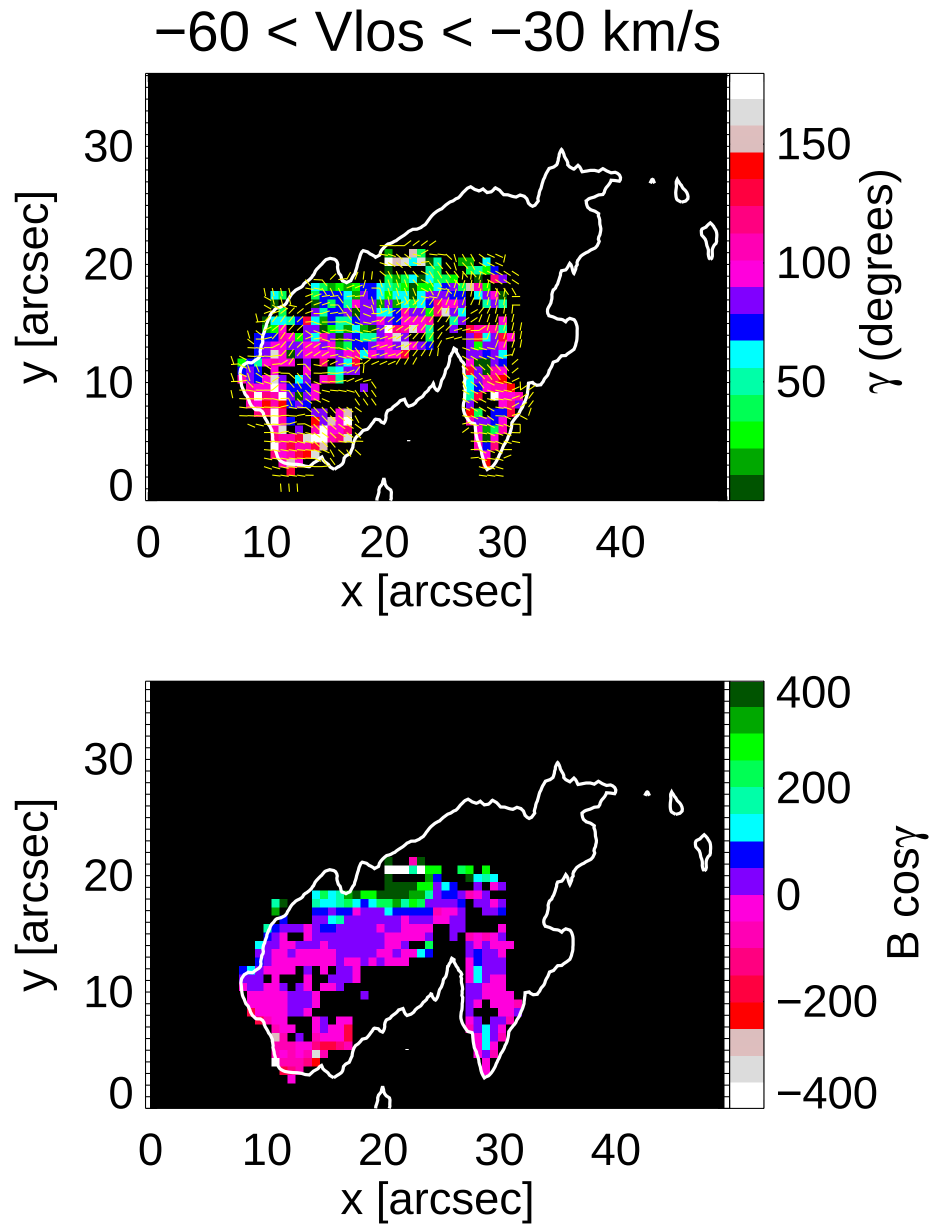

Figure 6.16: Upper panel: Map of the retrieved magnetic field inclination (γ) with overplotted azimuthal direction (χ, yellow lines). The azimuth values shown are a median averages over 9 pixels. Lower panel: Map of the LOS magnetic field component ($B\cos\gamma$). Both maps are for the He components with retrieved LOS velocity in the range $-60 < v_{LOS} < -30$ km/s.

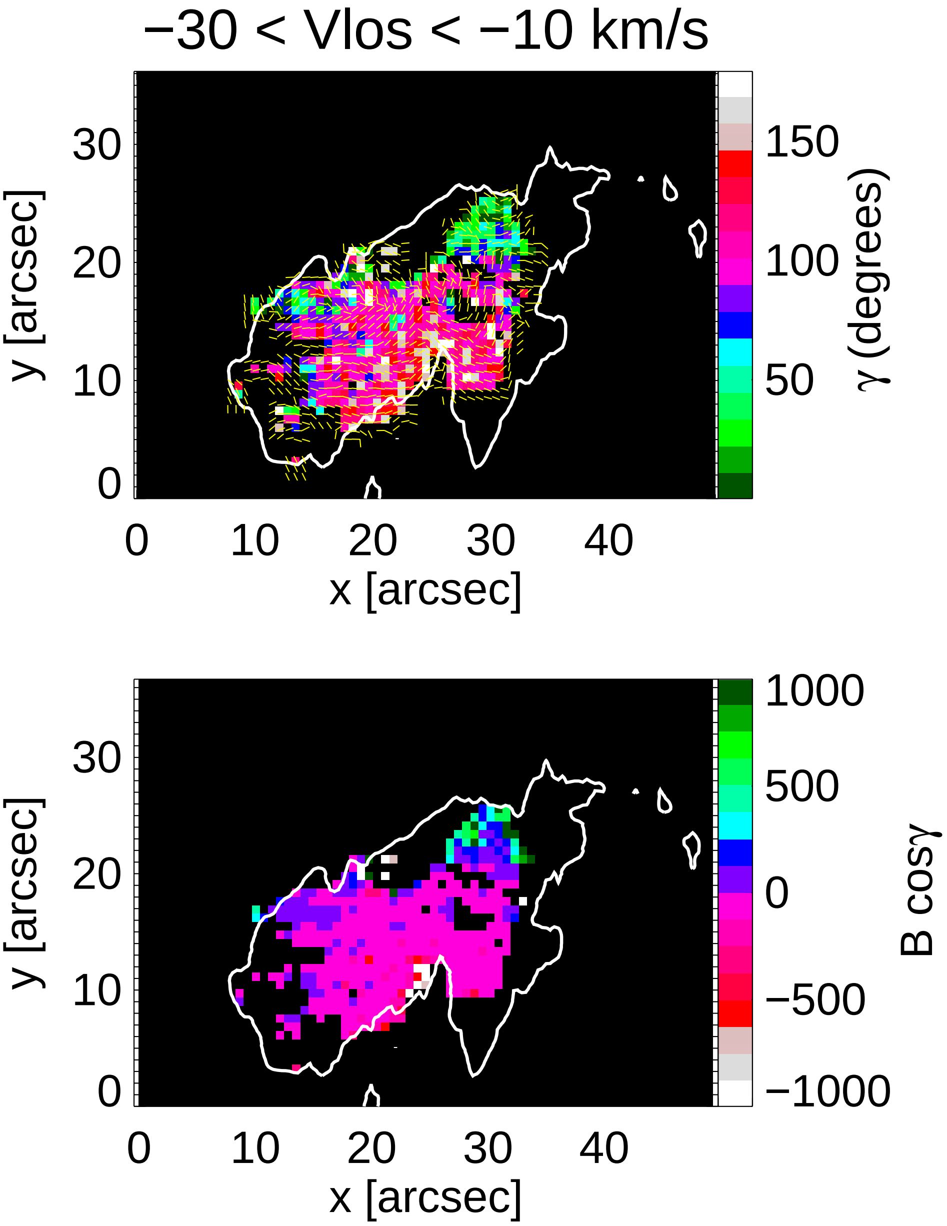

Figure 6.17: Upper panel: Map of the retrieved magnetic field inclination (γ) with overplotted azimuthal direction (χ, yellow lines). The azimuth values shown are a median averages over 9 pixels. Lower panel: Map of the LOS magnetic field component ($B\cos\gamma$). Both maps are for the He components with retrieved LOS velocity in the range $-30 < v_{LOS} < -10$ km/s.

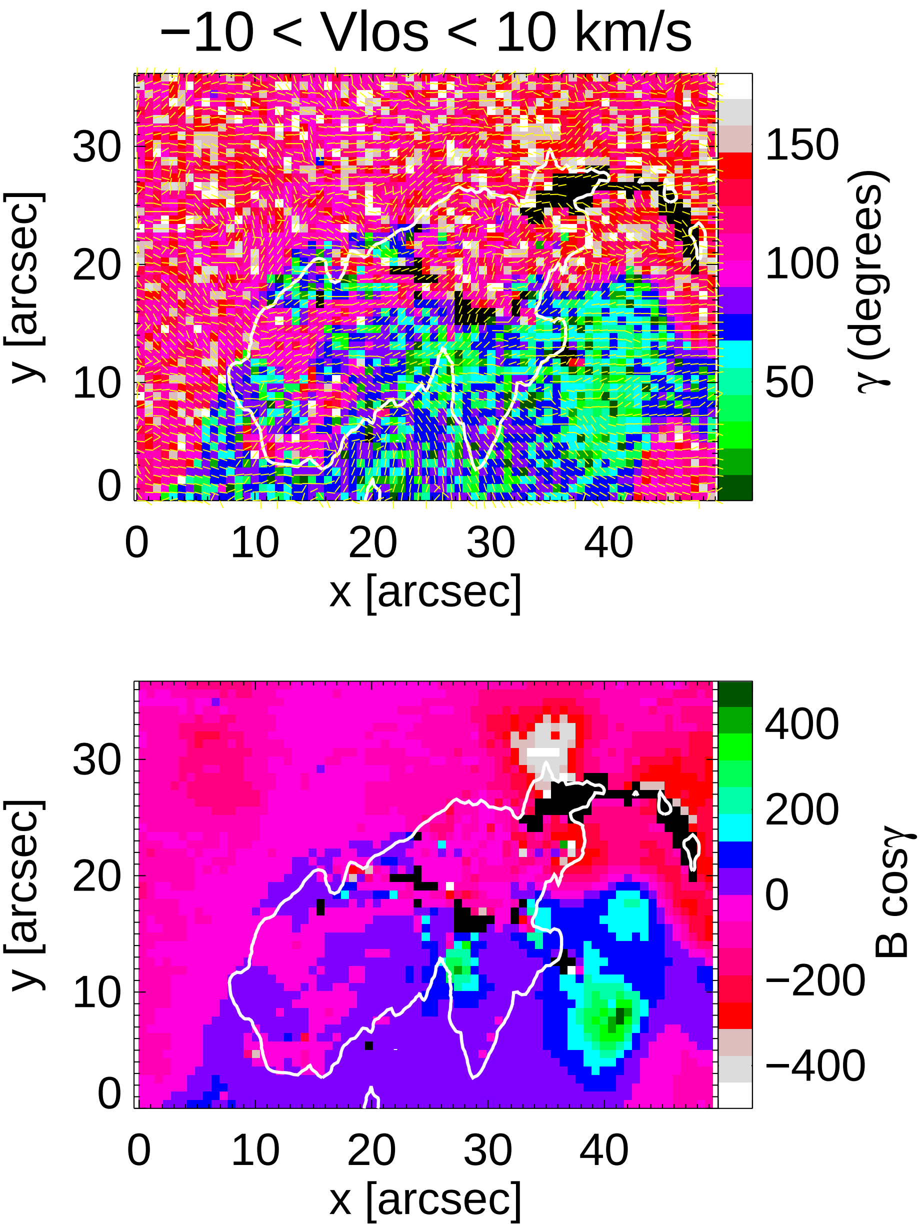

Figure 6.18: Upper panel: Map of the retrieved magnetic field inclination (γ) with overplotted azimuthal direction (χ, yellow lines). The azimuth values shown are a median averages over 9 pixels. Lower panel: Map of the LOS magnetic field component ($B\cos\gamma$). Both maps are for the He components with retrieved LOS velocity in the range $-10 < v_{LOS} < 10$ km/s.

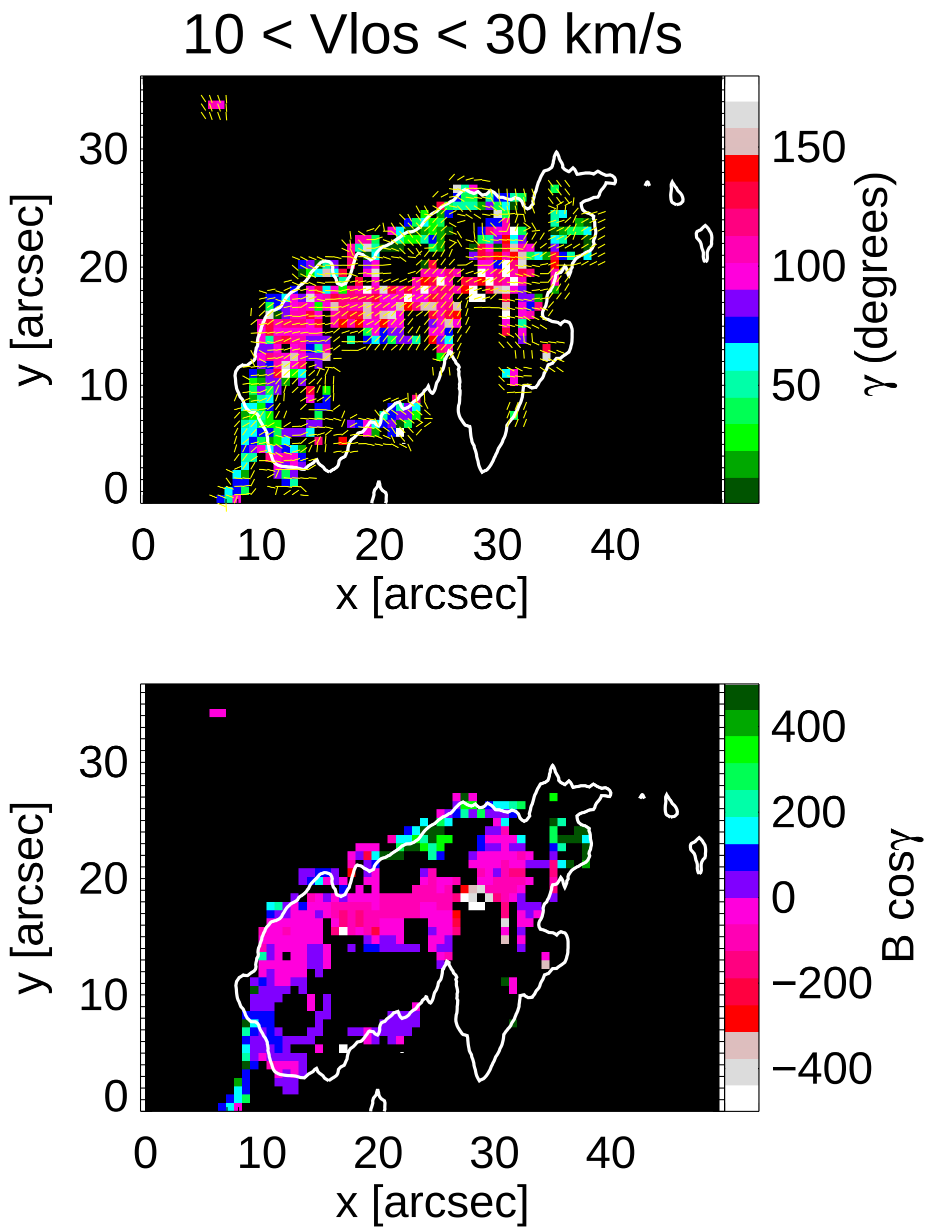

Figure 6.19: Upper panel: Map of the retrieved magnetic field inclination (γ) with overplotted azimuthal direction (χ, yellow lines). The azimuth values shown are a median averages over 9 pixels. Lower panel: Map of the LOS magnetic field component ($B\cos\gamma$). Both maps are for the He components with retrieved LOS velocity in the range $10 < v_{LOS} < 30$ km/s.

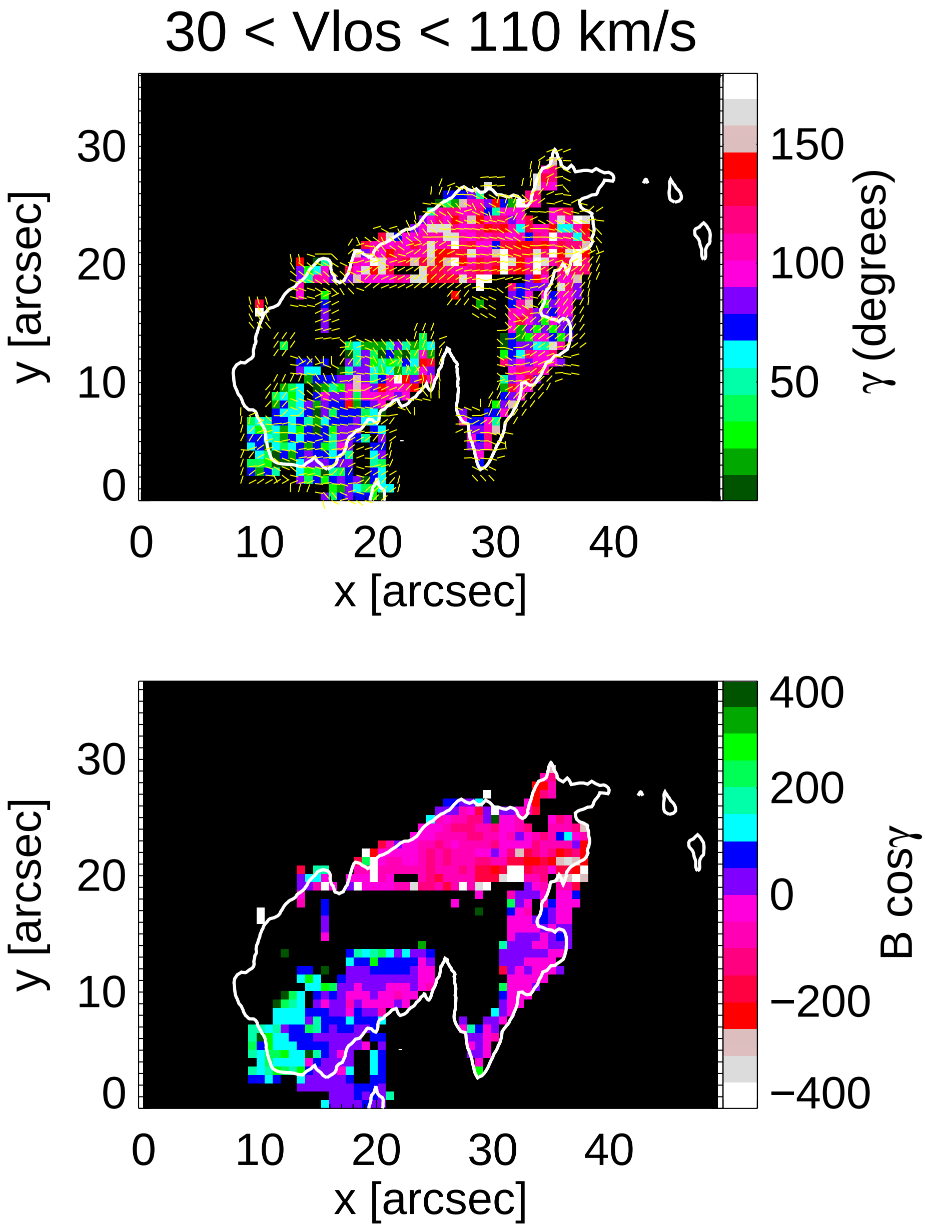

Figure 6.20: Upper panel: Map of the retrieved magnetic field inclination (γ) with overplotted azimuthal direction (χ, yellow lines). The azimuth values shown are a median averages over 9 pixels. Lower panel: Map of the LOS magnetic field component ($B\cos\gamma$). Both maps are for the He components with retrieved LOS velocity in the range $30 < v_{LOS} < 110$ km/s.

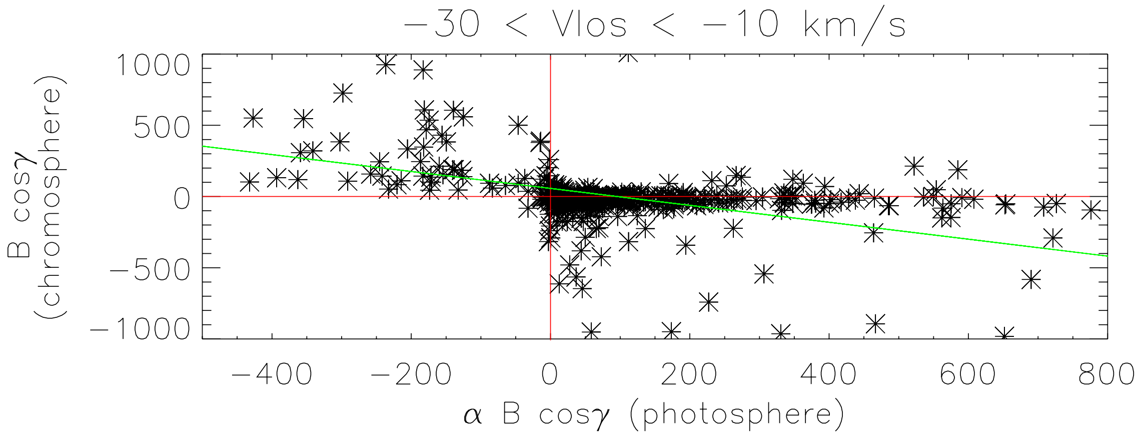

Figure 6.21: LOS magnetic field component in the chromosphere versus the LOS magnetic field component in the photosphere for the He components with retrieved LOS velocity in the range $-30 < v_{LOS} < -10$ km/s. The green line represents a linear regression.

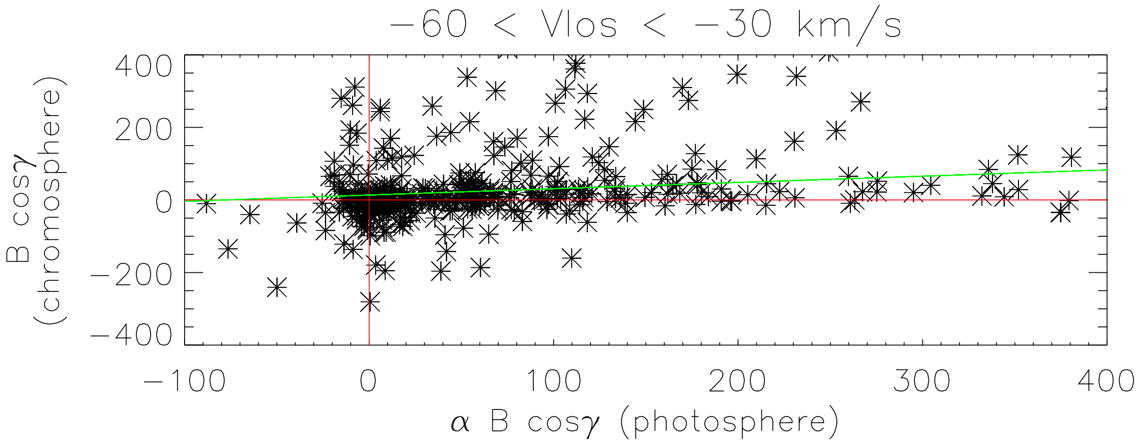

Figure 6.22: LOS magnetic field component in the chromosphere versus the LOS magnetic field component in the photosphere for the He components with retrieved LOS velocity in the range $-60 < v_{LOS} < -30$ km/s. The green line represents a linear regression.

6.2 Maps of retrieved parameters

Once all the profiles at each pixel position of the map are inverted, it is possible to start a general analysis of the retrieved atmospheric parameters.

As a quick test to check if the inversions are retrieving the right values of v_{LOS} for the He components, we can create a map like the one in Fig. 5.8 but with the retrieved values of v_{LOS}. We calculated for each pixel, the mean value of v_{LOS} for the He components weighted with the respective filling factor α. The obtained plot (Fig. 6.11) can be compared with Fig. 5.8, which was obtained from the observed profiles. The observed and retrieved values of v_{LOS} display the same behavior also quantitatively.

The contour line (red line) present in Fig. 6.11 gives the contour drawn at $(I_c - I) = 2.0 \times 10^4$ of the intensity map shown in Fig. 6.12. It is obtained by integrating the values of $I_c - I$ over the wavelength range covered by the He absorption (10828-10835.7 Å). The

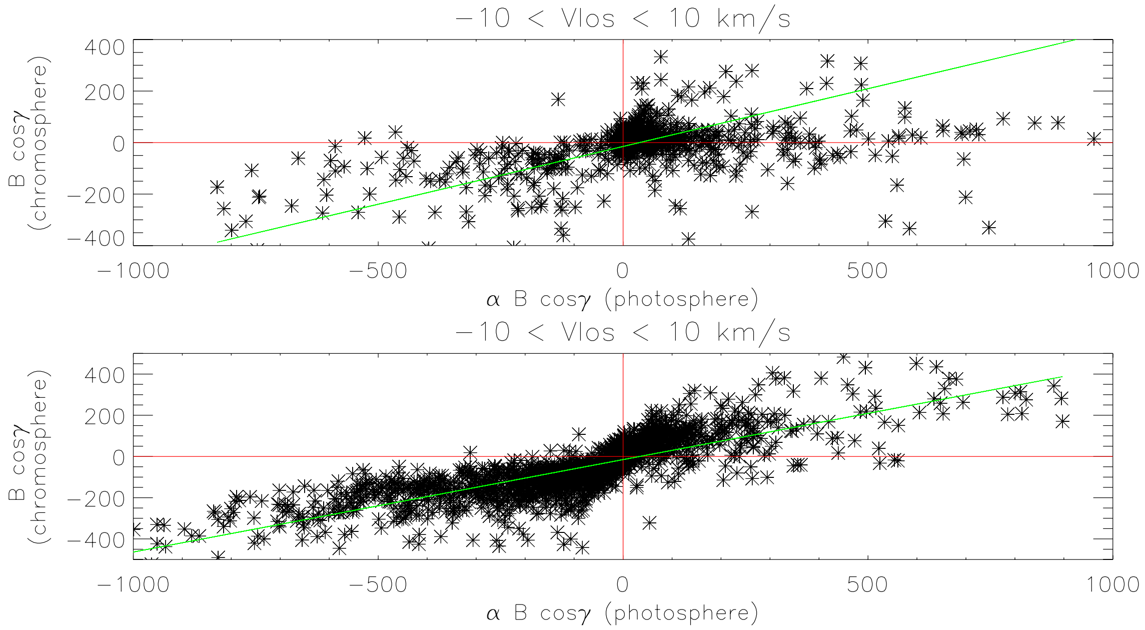

Figure 6.23: LOS magnetic field component in the chromosphere versus the LOS magnetic field component in the photosphere for the He components with retrieved LOS velocity in the range $-10 < v_{LOS} < 10$ km/s. The green lines represent a linear regression. In the upper panel, the points inside the filament are plotted, while in the lower panel, the points outside the filament.

intensity contributions due to the other spectral lines present in the chosen wavelength range have been subtracted. The same contour will be superimposed also on the next maps of this chapter in order to always keep in mind where the strong He absorption is located. The average value of $I_c - I$ inside the filament is $\approx$ 3.5 times bigger than the average value calculated in the quiet region around the filament and the maximum value of the He absorption observed in the filament is $\approx$ 10 times bigger than the He absorption in the quiet region.

Let us start with the analysis of the map obtained for the photospheric lines. Remember that the inversions are done by coupling the magnetic parameters between the four photospheric lines. In Fig. 6.13 there are three maps: the magnetic field strength (upper panel), the magnetic field inclination angle with respect to the LOS (middle panel) and the LOS magnetic field component averaged over magnetic and stray light contribution ($\alpha B\cos\gamma$, lower panel). In order to get the LOS magnetic component, we need to multiply it by α, that weights the contribution of the magnetic component to the total profile of a photospheric line. The color scales used in the middle and lower panels are chosen in a way that the same colors in the two maps, represent the same behaviors of the magnetic field vector inclination (pointing outward or inward).

In the middle panel, we can clearly identify the position of the inversion line where the magnetic field vector changes its polarity from outward (away from the Sun, inclination angle close to 0°) in the southern part of the scan to the opposite polarity (inclination angle close to 180°) in the northern part. Figure 6.14 displays an Hα image obtained with the slit-jaw camera at the VTT at 14:22:33 UT, prior to our scan and prior to the flare

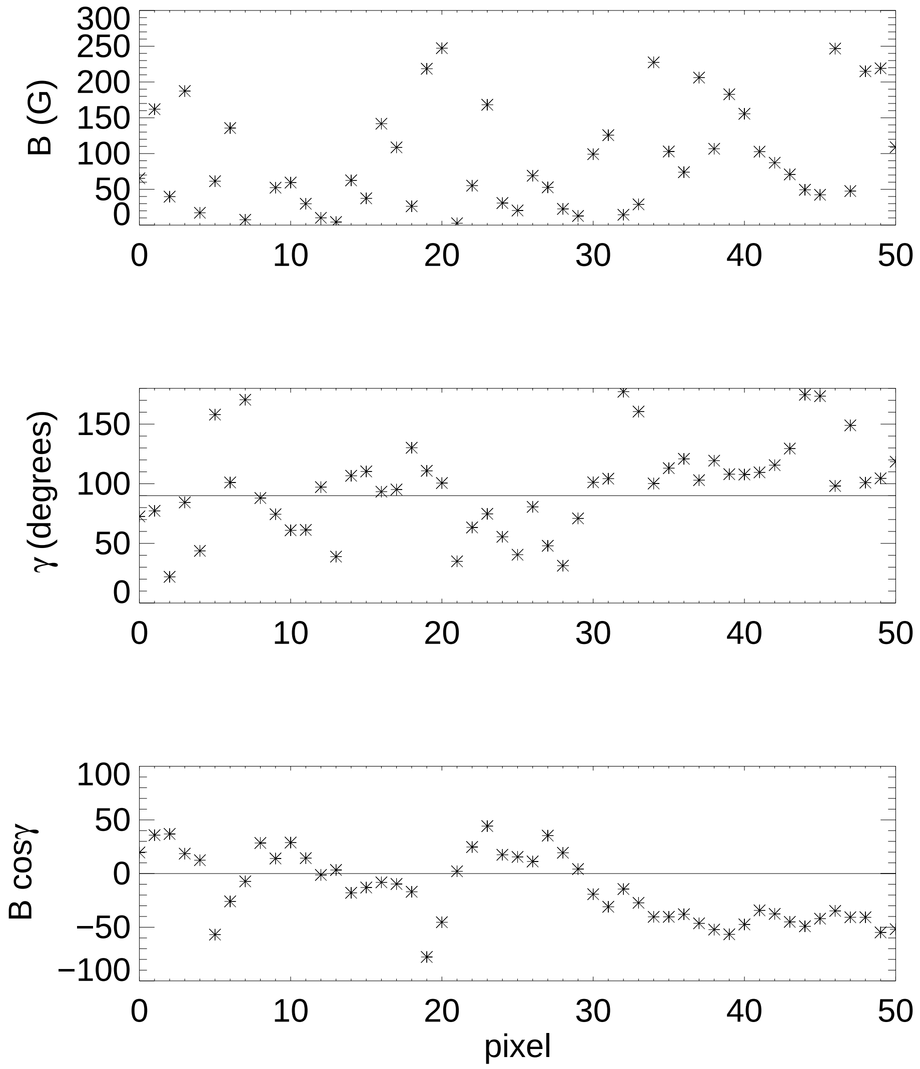

Figure 6.24: Starting from the upper panel: values of the magnetic field strength, inclination and LOS component along a vertical cut through Fig. 6.18 at position x = 12”.

eruption. The spectrograph slit was in a different position with respect to the scan studied in this work but the filament was entirely in the $H\alpha$ slit-jaw camera’s field of view and shows no activity. If we overplot the position of the photospheric inversion line (contour line drawn at $\gamma = 90^\circ$, see the middle panel of Fig. 6.13), we see the filament lying at the same position. The horizontal black line is one of the hairlines.

In the case of Fig. 6.13, the filament contour only partly straddles the inversion line, unlike the filament seen in Hα at 14:22:33 (Fig. 6.14). The strong He absorption at least in the first part of the scan is clearly situated only above one polarity of the photospheric field, suggesting that the filament (or better the flux rope structure) was moving during its activity phase. It was not stationary but rather was evolving fast. The movement of the material away from the photospheric inversion line is also deduced from the $H\alpha$ images. What we see, indeed, can be also due to a projection effect since our observations were obtained at a cosine of the heliocentric angle $\mu = 0.9$. We will come back to this point also later when we analyze the chromospheric magnetic field vector’s inclination.

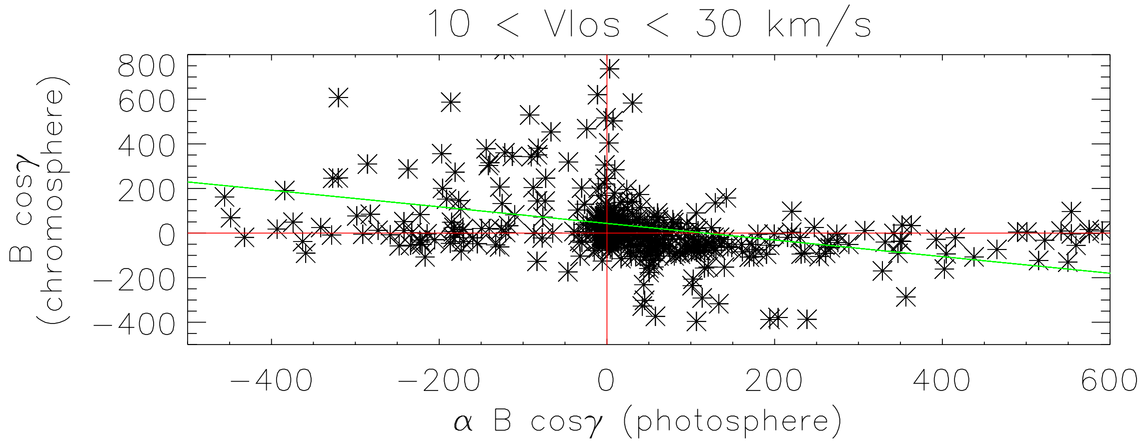

Figure 6.25: LOS magnetic field component in the chromosphere versus the LOS magnetic field component in the photosphere for the He components with retrieved LOS velocity in the range 10 < v_{LOS} < 30 km/s. The green line represents a linear regression.

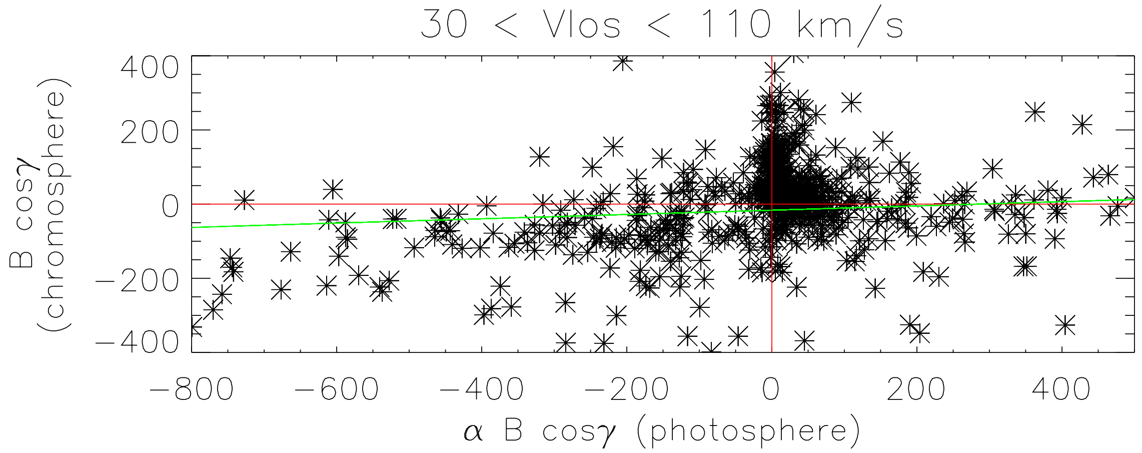

Figure 6.26: LOS magnetic field component in the chromosphere versus the LOS magnetic field component in the photosphere for the He components with retrieved LOS velocity in the range 30 < v_{LOS} < 110 km/s. The green line represents a linear regression.

Figure 6.15 displays the map of the retrieved chromospheric magnetic field strength, obtained by calculating the mean magnetic field strength weighted with the filling factor of the He components for each pixel position. The field strength values are generally lower than 400 G, inside the region of strong He absorption, indicated by the red contour line. Stronger field regions correspond to the positions of small pores visible in the continuum intensity map of Fig. 5.4, and also prominent locations of strong field in the photosphere (Fig. 6.13). The average field strength in the prominence is comparable with its average value in the region around it and it is ~ 180 G.

The maps of the retrieved magnetic field inclination values with respect to the LOS in the chromosphere are shown in the upper panels of Figs. 6.16– 6.20, with overplotted the azimuthal direction (χ, yellow lines). The lower panels of each figure display the values of the LOS magnetic field component. We made different maps for five ranges of LOS velocity to distinguish between the inclinations retrieved from the different He components.

The chosen ranges are: $-60 < v_{LOS} < -30$, $-30 < v_{LOS} < -10$ (blueshifted components), $-10 < v_{LOS} < 10$ (components nearly at rest), $10 < v_{LOS} < 30$, $30 < v_{LOS} < 110$ km/s (redshifted components). If in one pixel more He components with v_{LOS} in the selected range coexist, then we consider the inclination of the component with the highest filling factor.

A collective analysis of all the maps shows that the position of the boundary between the two polarities of the magnetic field in the photosphere and in the chromosphere differs (see, in particular, Figs. 6.16, 6.18 and 6.19). In the chromosphere we see a change of the magnetic field polarity happening inside the white line contour that identifies the presence of the filament material. This observation relates to the previous discussion about the fact that the strong He absorption seems to be shifted with respect to the photospheric inversion line. The retrieved azimuth values are noisy and in order to see if the magnetic field vector shows any preferential direction in the plane perpendicular to the line of sight, we averaged their values by performing a median average over 9 pixels (yellow lines in upper panels of Figs. 6.16– 6.20). The main feature, exhibited by all the maps is that the field lines are found to be almost parallel to the filament axis in the plane perpendicular to the line of sight.

Let us start the detailed analysis from the maps in Figs. 6.16 and 6.17 which show the behavior of the magnetic field inclination (upper panel) and the LOS magnetic field component (lower panel) of the blueshifted He components. In both maps there is a concentration of almost transversal field ($\gamma \approx 90°$) between two regions of more longitudinal field lines with opposite polarities. The magnetic field vector points away from the Sun (outward) in the northern part of the scan and inward in the southern part. The positions of the two polarities are opposite to the ones we have retrieved in the photospheric magnetic field where the magnetic field vector was instead pointing outward in the southern part of the scan and inward in the northern part. This behavior is also clearly identifiable in Fig. 6.21 where we plot the LOS magnetic field component in the chromosphere versus the LOS magnetic field component in the photosphere for the He components with $-30 < v_{LOS} < -10$ km/s. When the LOS magnetic field component in the photosphere is positive (pointing away from the Sun), it appears to be negative in the chromosphere and viceversa. Some points do display the same polarity in chromosphere and photosphere, which is probably due to the different location of the neutral line in the two layers. For the same reason, a plot like the one of Fig. 6.21, done for the range $-60 < v_{LOS} < -30$ km/s does not show the same clear opposite behavior of the LOS magnetic field components (see Fig. 6.22). This may be due to different positions of the neutral lines in photosphere and chromosphere that do not allow to see clearly opposite or equal polarity of photospheric and chromospheric fields in the same pixel. From the maps, we also notice that the photospheric field is more longitudinal than the chromospheric one for which γ is more concentrated around the value of 90°.

In Fig. 6.18 the maps for the He components almost at rest ($-10 < v_{LOS} < 10$ km/s) are shown. Outside the region covered by the filament but also for the majority of the profiles observed in the filament, the magnetic field maintains the same polarities in both atmospheric layers (see also Fig. 6.23), with the photospheric magnetic field generally being more inclined than the chromospheric one. As for the previous maps, we see also in this case that the chromospheric boundary between the magnetic field polarities inside the contour line differs from the photospheric one. If we look carefully, we can also notice that (in particular for 10” $< x <$ 25”, 3” $< y <$ 18”) the chromospheric magnetic field changes its polarity multiple times across the filament, pointing in the opposite direction as compared to the photospheric magnetic field. To see clearly this behavior, we made a cut through the filament along a vertical line at position $x =$ 12” of Fig. 6.18 and we plot in Fig. 6.24 the values of the magnetic field strength, inclination and LOS component along it. We clearly see that the inclination of the field lines changes multiple times from values lower than 90° to higher values and viceversa. The same behavior is displayed by the LOS magnetic field component that changes between positive and negative values.

The retrieved values of the magnetic field inclination for the redshifted He components are displayed in the maps of Fig. 6.19 and 6.20. The general situation is opposite to the one observed in the case of the blueshifted He components. The polarities of the magnetic field resemble the photospheric ones at the same position: the field lines go from outward in the southern part of the scan to the opposite polarity in the northern part, but with the chromospheric inversion line shifted southward. This behavior is displayed in Fig. 6.26 for the fastest downflows where we see that the LOS magnetic field components in the photosphere and in the chromosphere have the same sign. Fig. 6.25 obtained for the range $10 < v_{LOS} < 30$ km/s is not so conclusive for the same reasons we have already discussed in case of profiles with $-60 < v_{LOS} < -30$ km/s. We notice that in the map of the He components with $10 < v_{LOS} < 30$ km/s, there are some pixels in the upper right border of the filament that show a different behavior of the direction of the field from the described one. Their field is directed outward, in the opposite direction of the observed faster downflows shown by the profiles with $60 < v_{LOS} < 110$ km/s.

6.3 Discussion

We can put together all the information obtained from the inversions of the spectropolarimetric data and compare it to the different models of prominence support introduced in Sect. 2.3.1. We find best qualitative agreement of our observations with the flux rope model, better than with the dip model. In particular the presence of upflows and downflows, showing opposite magnetic polarities contemporarily in one element resolution, is well explained by the flux rope model.

Let us summarize the main results obtained from the inversions.

The main feature, exhibited by the retrieved values of the magnetic field azimuth, for all the components, is that the field lines are found to be almost parallel to the filament axis in the plane perpendicular to the line of sight. This is in agreement with previous measurements.

We measure downflow velocities up to 100 km/s and upflows up to 60 km/s along the line-of-sight. These supersonic up- and downflows are always coexisting with an He atmospheric component almost at rest ($-10 < v_{LOS} < +10$ km/s) within the same resolution element. The upflows and downflows are located in the entire filament except at its end points (lower left and upper right) where we see only strongly longitudinal, fast downflows. The He blueshifted components, belonging to more longitudinal field lines, are found at the edges of the filament showing opposite inclinations. In the body of the filament we see mostly transversal field. This picture suggests the presence of dipped field

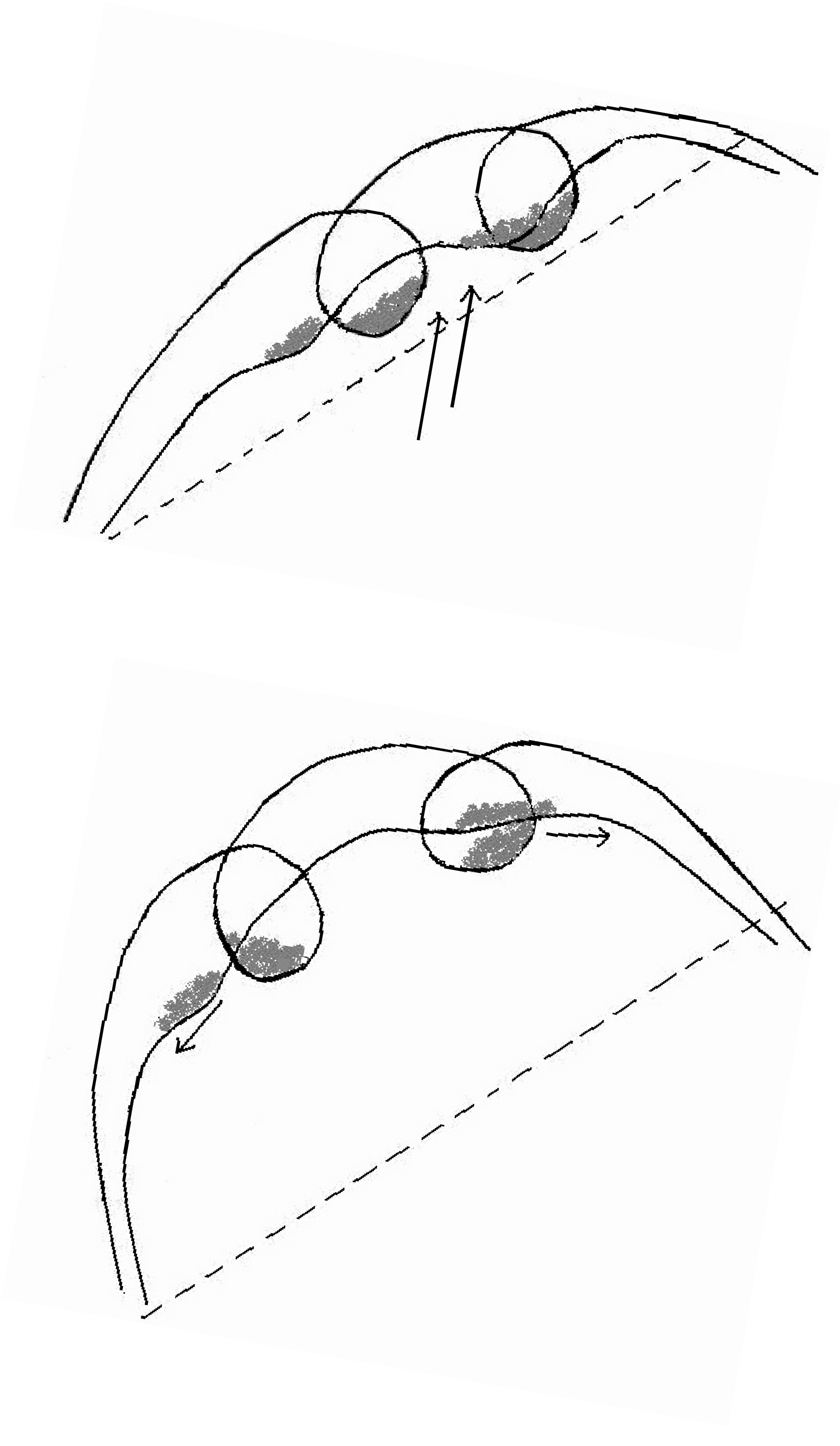

Figure 6.27: First proposed scenario. A flux rope is formed by different types of field lines. In the viewgraphs we represent two of these lines with different degrees of twist. In the upper panel, the flux rope is in equilibrium while in the lower panel is rising up. The filament material is represented by the shadowed regions. The dashed line is the photospheric inversion line.

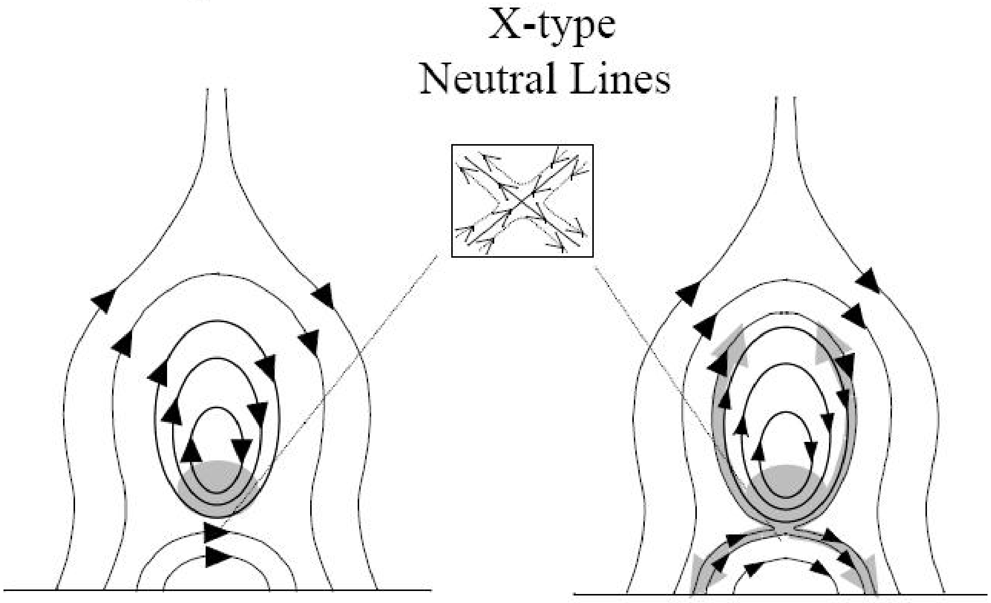

Figure 6.28: Evolution of an inverse polarity flux rope model during vertical reconnection. This type of reconnection allows prominence material to fall down along the reconnected field lines, and if it occurs sufficiently rapidly, prominence material may also get propelled up along the field lines and over the top of the flux rope. The figure has been adapted from Gilbert et al. (2001).

lines that are moving upward, carrying with them the filament material. So, the whole flux rope starts to become active for some reason, probably the nearby flare eruption. It starts moving and in particular it is lifting up, explaining the blueshifts. The presence of dipped field lines is also suggested by the map obtained for the He components at rest.

During this movement, we also observe some filament material flowing down along field lines having opposite inclination with respect to the dipped field lines. These downflows are faster at the filament end points and coincide with magnetic field of the same polarity as the photospheric magnetic field.

We can propose two scenarios to explain the downflows. Viewgraphs of the two scenarios are displayed in Figs. 6.27 and 6.28. First, the present models of flux rope describe magnetic field lines that twist about each other by one or more than one winding, in complicated ways. These lines form dips, where the filament plasma comes to rest. In Fig. 6.27 we show a flux rope made of two representative lines. They both form dips but possess different degrees of twist. When the flux rope is in equilibrium (upper panel), the filament material, represented by the shadowed regions, rests inside the dips. Once the flux rope is destabilized and raises up (lower panel), the filament material still trapped inside the dips moves up with the whole flux rope (observed upflows). Some other material can flow down along the less twisted field line that because of the upward movement is not dipped anymore (observed downflows).

A second explanation of what we observed is proposed in the work of Gilbert et al. (2001). The authors studied an active prominence at the solar limb that did not show a visible eruption of material and was not associated with a coronal mass ejection (as in our case). Their observations are based on He ɪ velocity data and Hα images and show apparent motion of material toward the observer up and around the flux rope (helical motion) and the simultaneous flow of material away from the observer along the filament spine. To interpret which mechanisms are involved in the propelling of prominence material up and around a flux rope, they use the inverse polarity flux rope model. If the gravity force comes to dominate the forces supporting the prominence, the field lines at the bottom of the flux rope will stretch until they meet the oppositely directed field lines of the underlying arcade, leading to vertical field line reconnection. The material can then fall down along the reconnected field lines, and if the reconnection occurs sufficiently rapidly, the prominence material may be propelled up along the field lines and over the top of the flux rope (see Fig. 6.28).

Applying this model to our observations, performed close to disc center, would result in: material flowing down (away from the observer) along the reconnected field lines and material propelled up along the dipped field lines (toward the observer). We cannot check whether in our case an inverse or a normal polarity flux rope model applies because we can retrieve the azimuth of the magnetic field vector from the inversions only with a 180° ambiguity. This means that we know the direction of the magnetic vector in the plane perpendicular to the LOS but we do not know its orientation. But, qualitatively, assuming the configuration of an inverse flux rope, this model could be applied to our case to describe the presence of contemporarily up- and downflows with opposite inclination.

The first scenario proposed does not need any assumption on the flux rope model. It can have either normal or inverse polarity. Qualitatively, both models can explain the coexistence of up- and downflows observed at the same pixel position and above all the inclination of the magnetic field vector observed.

7 Conclusions & Outlook

In this thesis, for the first time, the magnetic structure of an active region filament observed during its activity phase has been determined. The analysis is based on the physical interpretation of spectropolarimetric observations obtained in the He I 10830 Å lines on 18 May 2005 with the second generation Tenerife Infrared Polarimeter (TIP-II) at the German Vacuum Tower Telescope (VTT).

The information on the magnetic field vector in the filament are obtained by applying to the observed Stokes profiles a numerical code for the synthesis and inversion of Stokes profiles in a Milne-Eddington atmosphere (Lagg et al. 2004). A part of this thesis work has been devoted to improving the code to take into account the role of the incomplete Paschen-Back effect regime in the formation of the He lines. In summary, we analyze the influence of the Paschen-Back effect on the Stokes profiles of the He I 10830 Å multiplet lines, by using synthetic profiles. Additionally, we investigate its influence on the inversion of a spectropolarimetric scan of an emerging active region.

Our results support the conclusion of Socas-Navarro et al. (2004) that incomplete Paschen-Back splitting (IPBS) should be taken into account when modeling the polarization profiles of the He I 10830 multiplet. For example, we find that by including the incomplete Paschen-Back effect into our inversion code, on average 16% higher field strength values are retrieved from inversions, while other atmospheric parameters are affected less significantly.

We also show that the Paschen-Back effect is not the main cause of the area asymmetry exhibited by the many He I 10830 Stokes profiles with a line width smaller than ~ 0.30 Å in Lagg et al.'s (2004) emerging flux region observation. The spatial points corresponding to such Stokes V profiles are those for which the inferred value of the magnetic field strength is lower than ~ 1.1 kG when IPBS is taken into account. The fact that the area asymmetry of the observed V profiles is considerably stronger than of the synthetic V profiles indicates that some other effect drives the area asymmetry more strongly than the Paschen-Back effect. The main candidates are line-of-sight gradients of the magnetic field vector and the velocity.

The last two chapters of the thesis deal with the analysis of the magnetic structure of an active region filament, located close to disc center. Some minutes before our observations a flare erupted in the vicinity of the filament. This event, most probably, was the cause of the destabilization of the magnetic field lines supporting the filament plasma. Some material is observed to leave the filament in the Hα slit-jaw camera images, but the filament did not show a global eruption and was not associated with a coronal mass ejection. Its activation was mainly characterized by observed increased internal turbulent motions accompanied by a rising motion of the whole prominence.

The analysis of the observed polarization of the He I 10830 Å multiplet in the filament,

carried out by inverting the Stokes profiles, reveals the presence of different unresolved atmospheric components of the He lines, coexisting within the resolution element (~ 1.2 arcsec). The inversions support the idea that these components correspond to plasma trapped on different magnetic field lines, in fact the coupling of the magnetic field vector between the individual components results in worse fits to the observed profiles. The He components are strongly blue- or redshifted with supersonic velocities, sometimes coexisting within the same resolution element. We measure downflow velocities up to 100 km/s and upflows up to 60 km/s along the line-of-sight. These supersonic up- and downflows are always coexisting with a He atmospheric component almost at rest ($-10 < v_{LOS} < +10$ km/s) within the same resolution element.
An analysis of the locations of the flows reveals that both the up- and downflows are present in the entire filament except at its end points where we only see fast downflows. The He blueshifted components are associated with mostly transversal field lines in the body of the filament. These field lines are found to be curving upwards on both sides. This picture suggests the presence of dipped field lines that are moving upward, carrying with them the filament material. The idea is that the whole flux rope starts to become active for some reason, most probably identified with the nearby flare eruption and it starts to lift up, explaining the blueshifts. The presence of dipped field lines is also suggested from the behavior of the He components at rest. The He redshifted components exhibit the same magnetic polarity as the photospheric field, i.e. they have the opposite inclination with respect to the dipped field lines. These downflows are observed to be faster at the filament end points.
The main feature, exhibited by the retrieved values of the magnetic field azimuth, for all the components, is that the field lines are found to be almost parallel to the filament axis in the plane perpendicular to the line of sight. This is in agreement with previous measurements.
The two main theoretical models of prominence support (dip or flux rope models) have been used to interpret the results obtained. Even if the observed dipped field lines are predicted by both models, globally we find best qualitative agreement of our observations with the flux rope, better than with the dip model. In particular the presence of upflows and downflows, showing opposite polarities contemporarily in one resolution element, is well explained by the flux rope model. So, assuming a flux rope model, we propose two plausible scenarios to interpret the coexistence of up- and downflows observed at the same pixel position together with the inclination of the magnetic field vector observed.
Further steps need to be taken to improve on the results of the present study. In order to provide more statistics needed to set constraints on the theoretical models of prominence support, there is a strong request of new observational results. More information on the prominence magnetic structure would also allow to distinguish among the two main proposed models of prominence support (dip model and flux rope model).
Up to now, the main used lines for spectropolarimetric analysis were the He I D_3 lines seen only in emission in prominences at the limb and the Hα line. Our work encourages to exploit the diagnostics potential of magnetic fields of the He I 10830 Å, particularly in the case of active region filaments.
The inversion technique applied in this work to the observed Stokes profiles can be improved by introducing the quantum theory of the Hanle effect to have a full treatment of the formation of the He lines at 10830 Å. As shown recently by Trujillo Bueno & Asensio

Ramos (2007), the presence of atomic level polarization may have an influence on the emergent linear polarization, even for magnetic field strength as large as 1000 G. In the same paper, however, they also point out that in low lying optically thick plasma structures, such as those of active region filaments, the amount of atomic-level polarization may turn out to be negligible and the emergent linear polarization of the He 10830 multiplet in such structures be dominated by the contribution caused by the transverse Zeeman effect. Our profiles, indeed, do not show signatures typical of the Hanle effect, but only a full treatment of the quantum theory of the Zeeman and the Hanle effect can clear any doubt.

The multi-component He profiles presented in this work, clearly indicate that the spatial resolution of the spectro-polarimetric data is still inadequate to deal observationally with the fine structure of such magnetic fields. A higher spatial resolution would allow to resolve the different magnetic field components that are coexisting at the present resolution in one resolution element. This will help also to understand if the components are associated with adjacent field lines or they originate from different heights. In this way, we could also give a significant contribution in the understanding the magnetic topology of a filament.

A time series analysis would also be interesting to perform in order to analyze the evolution of the individual magnetic structures of a prominence. Together with short exposure time the analysis could help to resolve highly dynamical fine structures.

Bibliography

Amari, T., Luciani, J. F., Mikic Z., & Linker, J. 1999, Three-dimensional Solutions of Magnetohydrodynamic Equationsfor Prominence Magnetic Support: Twisted Magnetic Flux Rope, ApJ, 518, 57

Andretta, V., & Jones, H. P. 1997, On the Role of the Solar Corona and Transition Region in the Excitation of the Spectrum of Neutral Helium, ApJ, 489, 375

Antiochos, S. K., & Klimchuk, J. A. 1991, A model for the formation of solar prominences, ApJ, 378, 372

Antiochos, S. K., Dahlburg, R. B., & Klimchuk, J. A. 1994, The magnetic field of solar prominences, ApJ, 420, 41

Aulanier, G., & Schmieder, B. 2002, The magnetic nature of wide EUV filament channels and their role in the mass loading of CMEs, A&A, 386, 1106

Aznar Cuadrado, R., Solanki, S. K., & Lagg, A. 2005, Supersonic Downflows in the Solar Chromosphere are Very Common, in Chromospheric and Coronal Magnetic Fields, eds. D. E. Innes, A. Lagg, S. K. Solanki, & D. Danesy, (ESA Publication Division), Vol. ESA SP-596, 49

Avrett, E. H., Fontenla, J. M., & Loeser, R. 1994, Formation of the Solar 10830 Angstrom Line, in Infrared Solar Physics, ed. D. M. Rabin, IAU Symp. (Dordrecht: Kluwer Academic Publishers), 154, 35

Babcock, H. W., & Babcock, H. D. 1955, The Sun's Magnetic Field, 1952-1954, ApJ Lett., 121, 349

Bommier, V., Landi Degl'Innocenti, E., Leroy, J. L., & Sahal–Bréchot, S. 1994, Complete determination of the magnetic field vector and of the electron density in 14 prominences from linear polarization measurements in the HeI D3 and H-alpha lines, SoPh., 154, 231

Casini, R., López Ariste, A., Tomczyk S., & Lites, B. W. 2003, Magnetic Maps of Prominences from Full Stokes Analysis of the He I D3 Line, ApJ Lett., 598, 67

Charbonneau, P. 1995, Genetic Algorithms in Astronomy and Astrophysics, ApJS, 101, 309

Choe, G. S., & Lee, L. C. 1992, Formation of solar prominences by photospheric shearing motions, SoPh., 138, 291

Collados, M., Lagg., A., Díaz García, J. J., et al. 2007, Tenerife Infrared Polarimeter II, in The Physics of Chromospheric Plasmas, eds. P. Heinzel, I. Dorotovič, & R. J. Rutten, (Astronomical Society of the Pacific), ASP Conf. Ser., Vol. 368, 611

Gaizauskas, V., Mackay, D. H., & Harvey, K. L. 2001, Evolution of Solar Filament Channels Observed during a Major Poleward Surge of Photospheric Magnetic Flux, ApJ, 558, 888

Gilbert, H. R., Holzer, T. E., & Burkepile, J. T. 2001, Observational Interpretation of an Active Prominence on 1999 May 1, ApJ, 549, 1221

Grossmann-Doerth, U., Schüssler, M., & Solanki, S. K. 1989, Stokes V asymmetry and shift of spectral lines, A&A, 221, 338

Jensen, E. 1990, Summary of I.A.U. COLLOQUIUM:117 - Dynamics of Prominences, in Dynamics of Quiescent Prominences, eds. V. Ruzdjak, E. Tandberg-Hanssen, IAU Colloq., 363, 129

Kippenhahn, R., & Schlüter, A. 1957, Eine Theorie der solaren Filamente. Mit 7 Textabbildungen, Z. Astrophys., 43, 36

Kuperus, M., & Raadu, M. A. 1974, The Support of Prominences Formed in Neutral Sheets, A&A, 31, 189

Kuperus, M., & Tandberg-Hanssen, E. 1967, The Nature of Quiescent Solar Prominences, SoPh., 2, 39

Lagg, A., Woch, J., Krupp, N., & Solanki, S. K. 2004, Retrieval of the full magnetic vector with the He I multiplet at 1083 nm. Maps of an emerging flux region, A&A, 414, 1109

Lagg, A., Woch, J., Solanki, S. K., & Krupp, N. 2007, Supersonic downflows in the vicinity of a growing pore. Evidence of unresolved magnetic fine structure at chromospheric heights, A&A, 462, 1147

Landi Degl'Innocenti, E., & Landolfi, M. 2004, Polarization in Spectral Lines (Kluwer Academic Publishers)

Leroy, J. L. 1989, Observation of prominence magnetic fields, in Dynamics and Structure of Quiescent Solar Prominences, ed. E. R. Priest, (Dordrecht: Kluwer), 77

Leroy, J. L., Bommier, V., & Sahal–Bréchot, S. 1984, New data on the magnetic structure of quiescent prominences, A&A, 131, 33

Lin, H., Penn, M. J., & Kuhn, J. R. 1998, He i 10830 Angstrom Line Polarimetry: A New Tool to Probe the Filament Magnetic Fields, ApJ, 493, 978

López Ariste, A., & Aulanier, G. 2007, Unveiling the Magnetic Field Topology of Prominences, in The Physics of Chromospheric Plasmas, eds. P. Heinzel, I. Dorotovič, & R. J. Rutten, (Astronomical Society of the Pacific), ASP Conf. Ser., Vol. 368, 291

Low, B. C. 2001, Coronal mass ejections, magnetic flux ropes, and solar magnetism, J. Geophys. Res., 106, 25

Low, B. C., & Hundhausen, J. R. 1995, Magnetostatic structures of the solar corona. 2: The magnetic topology of quiescent prominences, ApJ, 443, 818

Martin, S. F. 1990, Conditions for the formation of prominences as inferred from optical observations, in Dynamics of Quiescent Prominences, eds. V. Ruzdjak & E. Tandberg-Hanssen, (Berlin: Springer), 1

Martínez Pillet, V., Collados, M., Sánchez Almeida, J. et al. 1999, LPSP & TIP: Full Stokes Polarimeters for the Canary Islands Observatories, in High Resolution Solar Physics: Theory, Observations, and Techniques (Astronomical Society of the Pacific), ASP Conf. Ser., 183, 264

Merenda, L., Trujillo Bueno, J., Landi Deglt'Innocenti, E., & Collados, M. 2006, Determination of the Magnetic Field Vector via the Hanle and Zeeman Effects in the He I λ10830 Multiplet: Evidence for Nearly Vertical Magnetic Fields in a Polar Crown Prominence, ApJ, 642, 554

Osherovich, V. A. 1989, Solar prominence model based on eigenvalue solutions. II - Filaments in the vertical magnetic fields, ApJ, 336, 1041

Pécseli, H., & Engvold, O. 2000, Modeling of prominence threads in magnetic fields: Levitation by incompressible MHD waves, SoPh., 194, 73

Penn, M. J. 2000, An Erupting Active Region Filament: Three-Dimensional Trajectory and Hydrogen Column Density, SoPh., 197, 313

Penn, M. J., & Kuhn, J. R. 1995, Imaging spectropolarimetry of the He I 1083 nanometer line in a flaring solar active region, ApJ Lett., 441, 51

Priest, E. R. 1990, Magnetic structure of prominences, in Dynamics of Quiescent Prominences, eds. V. Ruzdjak, E. Tandberg-Hanssen, (Berlin: Springer), 150

Priest, E. R., Hood, A. W., & Anzer U. 1989, A twisted flux-tube model for solar prominences. I - General properties, ApJ, 344, 1010

Rachkowsky, D. N. 1962, Izv. Krym. Astrofiz. Obs., 27, 148

Rachkowsky, D. N. 1967, The reduction for anomalous dispersion in the theory of the absorption line formation in a magnetic field (in Russian), Izv. Krym. Astrofiz. Obs., 37, 56

Rüedi, I., Solanki, S. K., & Livingston, W. C. 1995, Infrared lines as probes of solar magnetic features. X. HeI 10830A as a diagnostic of chromospheric magnetic fields, A&A, 293, 252

Socas-Navarro, H., Trujillo Bueno, J., & Landi Degl'Innocenti, E. 2004, Signatures of Incomplete Paschen-Back Splitting in the Polarization Profiles of the He I ?10830 Multiplet, ApJ, 612, 1175

Socas-Navarro, H., Trujillo Bueno, J., & Landi Degl'Innocenti, E. 2005, Polynomial Approximants for the Calculation of Polarization Profiles in the He I 10830 Å Multiplet, ApJ, 160, 312

Solanki, S. K. 1993, Smallscale Solar Magnetic Fields - an Overview, Space Sci. Rev., 63, 1

Solanki, S. K., & Stenflo, J. O. 1984, Properties of solar magnetic fluxtubes as revealed by Fe I lines, A&A, 140, 185

Solanki, S. K., Lagg, A., Woch, J., Krupp, N., & Collados, M. 2003, Three-dimensional magnetic field topology in a region of solar coronal heating, Nature, 425, 692

Tandberg-Hanssen, E. 1974, The Nature of Solar Prominences (Dordrecht: D. Reidel Publ. Co.)

Tandberg-Hanssen, E. 1995, The Nature of Solar Prominences (Dordrecht: Kluwer Acad. Publ.)

Tang, F. 1987, Quiescent prominences - Where are they formed?, SoPh., 107, 233

del Toro Iniesta, J. C. 2003, Introduction to Spectropolarimetry (Cambridge: Cambridge University Press)

Trujillo Bueno, J. 2001, Atomic Polarization and the Hanle Effect, in Advanced Solar Polarimetry - Theory, Observation, and Instrumentation, ASP Conf. Ser., 236, 161

Trujillo Bueno, J. 2003, New Diagnostic Windows on the Weak Magnetism of the Solar Atmosphere, in Solar Polarization 3, eds. J. Trujillo Bueno & Sanchez Almeida, ASP Conf. Ser., 307, 407

Trujillo Bueno, J., & Asensio Ramos, A. 2007, Influence of atomic polarization and horizontal illumination on the Stokes profiles of the He I 10830 Å multiplet, ApJ, 655, 642

Trujillo Bueno, J., Landi Degl'Innocenti, E., Collados, M., Merenda, L., & Manso Sainz, R. 2002, Selective absorption processes as the origin of puzzling spectral line polarization from the Sun, Nature, 415, 403

Unno, W. 1956, Line Formation of a Normal Zeeman Triplet, PASJ, 8, 108

van Ballegooijen, A. A. 2000, Solar Prominence Models, in Encyclopedia of Astronomy and Astrophysics, ed. P. Murdin (Institute of Physics Publishing, London), http://www.ency-astro.com

van Ballegooijen, A. A., & Martens, P. C. H. 1989, Formation and eruption of solar prominences, ApJ, 343, 971

Van Hoven, G., Mok, Y., & Drake, J. F. 1992, Prominence condensation and magnetic levitation in a coronal loop, SoPh., 140, 267

Wiegelmann, T., Lagg, A., Solanki, S. K., Inhester, B., & Woch, J. 2005, Comparing magnetic field extrapolations with measurements of magnetic loops, A&A, 433, 701

Wu, S. T., Bao, J. J., An, C. H., & Tandberg-Hanssen, E. 1990, The role of condensation and heat conduction in the formation of prominences - an MHD simulation, SoPh., 125, 277

You, J., Hui, L., Zhongyu, F., & Sakurai, T. 2001, Multi-Wavelength Observation of the 3n/x3.3 Flare of 28 November 1998, SoPh., 203, 107

Zirin, H. 1988, Astrophysics of the sun (Cambridge: Cambridge University Press)

Publications

Refereed contributions:

Sasso, C., Lagg, A., & Solanki, S. K. *Milne-Eddington inversions of the He* I *10830 Å Stokes profiles: Influence of the Paschen-Back effect*. A&A, 2006, vol 456, 367.

Conference contributions:

Sasso, C., Lagg, A., & Solanki, S.K. *Influence of the Paschen-Back effect on the Stokes profiles of the HE 10830 Å triplet*, in: Proceedings of the International Scientific Conference on Chromospheric and Coronal Magnetic Fields (edited by D. E. Innes, A. Lagg, S. K. Solanki, and D. Danesy), ESA SP-596, ESA Publ. Div., Noordwijk, 2005.

Sasso, C., Lagg, A., Solanki, S.K., & Socas-Navarro, H. *Influence of the Paschen-Back effect on the results of polarimetric inversions of the He* I *10830 Å triplet*. Memorie della Societa Astronomica Italiana Supplement, 2006, 9, 126.

Teriaca, L., Lagg, A., Aznar Cuadrado, R., **Sasso, C.**, & Solanki, S.K. *The dynamics and structure of the solar atmosphere as obtained from combined SUMER/SOHO and TIP2/VTT observations*. Proceedings ofSOHO 17 - 10 Years of SOHO and Beyond, 7-12 May 2006, Giardini Naxos, Sicily, Italy (edited by H. Lacoste), ESA SP-617, ESA Publ. Div., Noordwijk, The Netherlands, 2006.

Solanki, S. K., Lagg, A., Aznar Cuadrado, R., Orozco, D., Collados, M., Wiegelmann, T., Woch, J. , **Sasso, C.**, & Krupp, N. *Measuring the magnetic vector with the He* I*10830 Å line: A rich new world*. Solar Polarization 4 (edited by R. Casini and B. W. Lites), vol. 358 of ASP Conference Series, 2006, 431.

Sasso, C., Lagg, A., Solanki, S.K., Aznar Cuadrado, R., & Collados, M. *Full-Stokes Observations and Analysis of He I 10830 Å in a Flaring Region*, The Physics of Chromospheric Plasmas (edited by P. Heinzel, I. Dorotovič, and R. J. Rutten), vol. 368 of ASP Conference Series, 2007, 467.

Sasso, C., Lagg, A., & Solanki, S.K. *Spectropolarimetry in the chromospheric He* I *1083.0 μm multiplet*, in: 1st Workshop of Astronomy and Astrophysics for Students (edited by N. R. Napolitano and M. Paolillo), INFN-Naples, 2007.

Acknowledgements

At the end of three long years here I am. I’ve always thought about this moment and now that it came I have to find the words to express my thanks to all the people that shared life moments with me.

So, I start with a thanks to the Max Planck Institute for Solar System Research (MPS) and the International Max Planck Research School on Physical Processes in the Solar System and Beyond (IMPRS), in the person of Dieter Schmitt, for giving me the opportunity to carry out the research presented in this thesis. I found here in Germany a very ’warm’ environment to work. Many thanks to my supervisor Sami Solanki. For all the many things he taught me and for believing in my ability to carry out this work. I wish to thank Franz Kneer. Dear Franz, every time I came to the University I always found in you a paternal support. Andreas, I really spent a good time working with you. Thanks, thanks and thanks for being always there to help me and to answer my questions. A huge thank goes to Regina. Without her, maybe, I would have never worked on these observations.

Thanks to ALL my friends here at the Institute, in particular to Silvia, Luca, Ceci, Manu. Grazie infinite. Above all, for your help in the last steps. Thanks to Hannah and Ray. Living with you gave me the feeling of being in a family.

Thanks to my parents and my family. I love you. Without your support I would have never been able to stay so much time far and alone. To my grandmother. You always believed in me and I wanted to make you proud of me. I know you will pray for me.

To my husband. This thesis is for you. Now I will come back home. Ti amo.

Lebenslauf

Name:	Clementina Sasso
Geburtsdatum:	15 Juli 1979
Geburtsort:	Torre del Greco (Na), Italien
Familienstand:	verheiratet
Eltern:	Giuseppe Sasso Angela Dentice
Staatsangehörigkeit:	Italienisch

Schulbildung:	1992 - 1997	Liceo Scientifico “A. Nobel”, Torre del Greco (Na), Italien
Studium:	1997 - 2004	Physikstudium an der Physikalischen Fakultät der Universität “Federico II”, Napoli, Italien
Promotion:	2005 - 2008	Promotion an der Universitäts Göttingen Stipendium der International Max Planck Research School on Physical Processes in the Solar System and Beyond